

Waves on Shear and Vortex Flows and the Stability of the Moore-Saffman model for a Trailing Wingtip Vortex

A thesis submitted to McGill University
in partial fulfillment of the requirements for the degree of
Doctor of Philosophy

by

Jan Feys

on

April 15, 2015

Department of Mathematics and Statistics
Faculty of Science
McGill University, Montreal

© 2015 Jan Feys

ABSTRACT

This thesis comprises three papers. In the first, the eigenvalue problem governing the propagation of long nonlinear surface waves is investigated when there is a current $\bar{u}(y)$ beneath the surface, y being the vertical coordinate. We consider specific velocity profiles such as boundary layer profiles of the Falkner-Skan similarity type, including the Blasius case. The singular solutions of the Rayleigh equation are examined to gain insight about the long wave limit of such solutions.

The second paper considers the inviscid linear stability of a trailing vortex using mean flow profiles given by an approximate solution of the Navier-Stokes equations. The axial and tangential velocity profiles obtained from this solution, deduced by Moore and Saffman (1973), agree well with experiments involving wings at slight angles of attack; in particular, they better describe the jet-like and wake-like axial flows near the center of the vortex than does the much-studied similarity solution found by Batchelor (1964). We numerically obtain growth rates for unstable perturbations for different values of n , a wingtip loading parameter.

Finally, we study the elliptical modes of instability in a pair of counter-rotating trailing wingtip vortices using the aforementioned Moore-Saffman vortex model. To this end, a direct numerical simulation is performed using a spectral method in cylindrical coordinates developed by Matsushima and Marcus (1997). We obtain growth rates and eigenmodes, several of which suggest the presence of a critical layer singularity in the radial coordinate r . Moreover, we compare our results to those for the Batchelor vortex, which is the model that most recent investigations have employed.

As is clear from the above, the subject matter of this thesis is twofold: waves on a shear flow on the one hand and vortex stability on the other. However distinct, both subjects have in common the presence of a critical layer singularity, which has a profound impact on the solutions of the equations governing each flow.

ABRÉGÉ

Cette thèse se compose de trois articles. Dans le premier, le problème des valeurs propres qui régissent la propagation d'ondes de surface longues non-linéaires est étudié lorsqu'il existe un courant $\bar{u}(y)$ sous la surface, y étant la coordonnée verticale. Nous considérons des profils de vitesse particuliers, tels que les profils de couche limite du type de similarité Falkner-Skan, y compris le cas Blasius. Les solutions singulières de l'équation de Rayleigh sont examinées afin d'approfondir notre compréhension de la limite d'ondes longues de telles solutions.

Le deuxième article considère la stabilité linéaire non visqueuse d'un tourbillon de fuite en utilisant les profils d'écoulement moyen donnés par une solution approximative des équations de Navier-Stokes. Les profils de vitesse axiale et tangentielle obtenus par cette méthode, déduits par Moore et Saffman (1973), correspondent bien à des expériences impliquant des ailes à de légers angles d'attaque; en particulier, ils décrivent mieux les flux axiaux en forme de jet ou de sillage près du centre du tourbillon que ne le fait la solution de similarité très étudiée de Batchelor (1964). Nous obtenons numériquement des taux de croissance des perturbations instables pour diverses valeurs de n , un paramètre qui mesure la charge alaire au bout de l'aile.

Enfin, nous étudions les modes elliptiques d'instabilité dans une paire de tourbillons marginaux contrarotatifs en employant le modèle tourbillonnaire précité de Moore-Saffman. À cette fin, une simulation numérique directe est effectuée en utilisant une méthode spectrale en coordonnées cylindriques développée par Matsushima et Marcus (1997). Nous obtenons des taux de croissance et des modes propres, dont plusieurs indiquent la présence d'une couche critique dans la coordonnée radiale r . De plus, nous comparons nos résultats à ceux obtenus dans le cas du tourbillon de Batchelor, le modèle employé par la plupart des études récentes. Comme il ressort de ce qui précède, le but de cette thèse est double: nous traitons d'une part des ondes sur un écoulement cisailé et d'autre part de la stabilité tourbillonnaire. Bien qu'ils soient distincts, les deux thèmes ont en commun la présence d'une singularité dans la couche critique, ce qui a de profondes conséquences sur les solutions des équations qui déterminent chaque type d'écoulement.

ACKNOWLEDGMENTS

Foremost, I am grateful to my doctoral advisor Professor Sherwin A. Maslowe. His patience and guidance have been invaluable to me through the years. The fact that he can count among his friends many of the most eminent researchers in the field, including most of the key references in this thesis, has benefited me in more than one way. Importantly, it offered me an exceptional opportunity to better understand the literature on shear and vortex flows. I am deeply thankful for the time and effort he has devoted to helping me discover applied mathematics.

In addition, I would like to thank the professors, postdocs and students in applied mathematics (and neighbouring fields) at McGill University. I truly felt enriched by their presence. The professors: Jean-Christophe Nave, Gantumur Tsogtgerel, Adam Oberman, Peter Bartello and Rustum Choksi. Among the postdocs, there were Andy Wan, Dmitry Kolomenskiy, Suresh Eswarathasan, David Shirokoff and Brian Seguin. I also had many interesting conversations with graduate students such as Lisa Powers, Alexandra Tcheng, Tiago Salvador, Hossein Amini Kafiabad, Mohammad Farazmand and Jinming Wen.

Perhaps most of all, my memories of Montreal will be filled with the many people I got to know and now call good friends; people like Anusar Farooqui, André-Paul Grecianu, Jason Polak, Joel Tousignant-Barnes, Jonathan Weinberg and Kael Dixon. I especially owe Maria a great deal of appreciation for her patience and support when my work was tough, and for being an unstoppable force of happiness and enthusiasm in my life.

Finally, my profound gratitude goes out to my parents Denise and Georges, for their endless support, to my siblings Bert and Roel, for leading the way abroad, and to my twin brother Frank, for fuelling my passion for mathematics through the good times we shared studying it together.

CONTRIBUTIONS OF AUTHORS

Each part of this dissertation is an article that has either appeared in a journal or has been submitted for peer review. The research work for all three was performed by myself under the guidance of my doctoral supervisor Professor Sherwin A. Maslowe, who is a co-author on all three manuscripts.

- Part 1 was published in *Studies in Applied Mathematics* in 2011, see [33].
- Part 2 appeared in *Physics of Fluids* in 2014 as Feys and Maslowe [34].
- Part 3 is a manuscript that was submitted for publication in April 2015.

TABLE OF CONTENTS

Background and outline	1
Long nonlinear waves on a shear flow	2
Stability of a trailing vortex	4
Elliptical instability of a vortex pair	6
1 Long Nonlinear Surface Waves in the Presence of a Variable Current	9
1.1 Introduction	10
1.2 Formulation of the outer problem	13
1.3 The eigenvalue problem	15
1.3.1 Numerical procedure for singular modes	17
1.4 Numerical results for various velocity profiles	19
1.4.1 The nonlinear critical wall layer	20
1.4.2 Falkner-Skan boundary layer profiles	22
1.4.3 Singular solutions of Rayleigh's equation with a free surface	24
1.5 Concluding remarks	26
2 Linear Stability of the Moore-Saffman Model for a Trailing Wingtip Vortex	29
2.1 Introduction	30
2.2 Moore-Saffman vortex	35
2.3 Stability equation and numerical approach	40

2.4	Numerical results	42
2.4.1	Instabilities for $ m = 1$	43
2.4.2	Instabilities for higher azimuthal wave numbers $ m > 1$	47
2.4.3	Axisymmetric instabilities ($m = 0$)	50
2.5	Concluding Remarks	51
 3 Elliptical Instability of the Moore-Saffman Model for a Trail-		
ing Wingtip Vortex		55
3.1	Introduction	56
3.2	Stability characteristics of the Moore-Saffman vortex	61
3.2.1	Basic formulation	62
3.2.2	Linear stability	64
3.3	Governing equations and numerical procedure	70
3.3.1	Governing equations	70
3.3.2	Numerical method	72
3.3.3	Numerical convergence and code verification	76
3.4	Numerical results	80
3.5	Concluding remarks	94
 Summary		97
 References		100

LIST OF FIGURES

1.1	Dispersion curve showing phase speed vs. inverse Froude number for the velocity profile $\bar{u} = \tanh 3y / \tanh 3$	20
1.2	Dispersion curve of phase speed vs. inverse Froude number for different streamwise pressure gradients.	23
1.3	Variation of phase speed with streamwise pressure gradient at a constant inverse Froude number, $G = 1.0$	24
1.4	Singular solutions of the Rayleigh equation for the Blasius boundary layer and the asymptotic suction profile at a constant inverse Froude number, $G = 1.0$	25
2.1	Axial velocity profiles from the experiments of Lee and Pereira [56]. The chord $c = 28$ cm and the measurements were made at a distance $x/c = 5$ downstream of the wingtip.	34
2.2	Numerical solution of Equation (2.8) giving (a) the tangential velocity profile and (b) the axial velocity profile obtained from the similarity solution of Moore and Saffman [67].	39
2.3	Contour plots of the growth rates ω_i of instabilities for all values in the (q, k) -plane for $m = -1$: shown are results for (a) $n = 0.70$, (b) $n = 0.60$, (c) $n = 0.50$ and (d) $n = 0.40$. The spacing between the solid contours is 0.01. The outermost solid contour represents modes with growth rate $\omega_i = 0.03$ and the dotted contour is the neutral curve.	44
2.4	The maximum growth rates ω_i for all values in the (q, n) -plane for (a) $m = -1$ and (b) $m = -2$. The outermost contour represents the neutral curve and the spacing between the contours is 0.02.	46
2.5	The variation of ω_i with k for $q = 1$ and $n = 0.50$ for several azimuthal wave numbers ($m = -1, -2, -3$ and -4).	47

2.6	Contour plots of the growth rates ω_i of instabilities for all values in the (q, k) -plane for $n = 0.50$: shown are (a) $m = -2$, (b) $m = -3$ and (c) $m = -4$. The spacing between the contours is 0.02. The outermost contour represents modes with constant growth rate $\omega_i = 0.04$	49
3.1	Numerical solution giving (a) the tangential velocity profile $V_n(r)$ and (b) the axial velocity profile $W_n(r)$ obtained from the similarity solution of Moore and Saffman [67].	63
3.2	For azimuthal wavenumber $m = -1$, both (a) the growth rate ω_i and (b) the corresponding axial wavenumber k for the most unstable inviscid modes for all values in the (W_0, n) -plane are displayed. The contour spacing is 0.05 in (a) and 0.03 in (b), with the outermost contour representing the neutral curve. The horizontal dotted lines mark $n = 0.44$ and $n = 0.25$	65
3.3	Same as Figure 3.2, but for $m = -2$	67
3.4	Same as Figure 3.2, but for $Re = 3180$	69
3.5	Shown in (a) is the convergence of the growth rate ω_i with an increasing number of modes N for Case III. The following parameters are fixed: $n = 0.95$ (approximately Batchelor), $\varepsilon = 0.0625$, and $W_0 = 0.482$, $Re = 3180$ and $k = 1.88$. The resulting elliptical instability is characterized by a resonance between the strain field and azimuthal wavenumbers $(m_1, m_2) = (-2, 0)$. In (b), the region near the asymptotic value of ω_i has been magnified. In both plots, the diamonds represent sample points.	78

3.6	The perturbation vorticity field for the unstable mode named Case III. The elliptical instability structure is visible as a combination of modes with azimuthal wavenumber $m_1 = -2$ and $m_2 = 0$. The contours, which are isovorticity lines, are spaced 0.1 apart. The zero vorticity contour is not displayed. Two poles of negative vorticity (with a minimum value below -0.9) and two poles of positive vorticity (with a maximum value above 0.5) exist. The vortex center is marked by a black dot.	79
3.7	The growth rate ω_i as a function of the axial wavenumber k is presented for a number of different mean flow velocity profiles. In (a), results for the Batchelor vortex are shown. In the other plots, Moore-Saffman profiles are used with the wing loading parameter n fixed at (b) $n = 0.95$, (c) $n = 0.80$, (d) $n = 0.70$, (e) $n = 0.50$ and (f) $n = 0.30$. The flow parameters are maintained at $\varepsilon = 0.0625$, $W_0 = 0.482$ and $Re = 3180$ throughout. Resonances of odd and even azimuthal wavenumbers are plotted on different curves. Note the different bounds on each vertical axis.	81
3.8	The growth rate ω_i as a function of the wing loading parameter n for fixed flow parameters $\varepsilon = 0.0625$, $W_0 = 0.482$ and $Re = 3180$. The value of the axial wavenumber is held steady at (a) $k = 1.88$, (c) $k = 2.60$, (c) $k = 3.23$ and (d) $k = 4.57$. Resonances of odd and even azimuthal wavenumbers are represented by star and circle symbols, respectively.	84
3.9	Contour plots of the maximum growth rate ω_i for every value of the axial wavenumber k and wing loading parameter n are presented for (a) $W_0 = 0.482$ and (b) $W_0 = 0.2494$. The other flow parameters remain fixed at $\varepsilon = 0.0625$ and $Re = 3180$. Every point shows the most unstable resonance for a given value of (k, n) . The contours are curves of constant growth rate. The spacing between the contours is 0.008. In each plot, several contours have been labeled for clarity.	86

3.10	The growth rate ω_i as a function of the axial wavenumber k for fixed flow parameters $\varepsilon = 0.0625$, $W_0 = 0.482$ and $Re = 3180$, shown for (a) the Batchelor vortex and (b) the Moore-Saffman vortex with $n = 0.50$. The solid line displays the damping due to viscosity. The viscous decay rate is estimated using the expression $-(k^2/Re)(1+\varepsilon/(\gamma-\varepsilon))$. Resonances of odd and even azimuthal wavenumbers are represented by star and circle symbols, respectively. . . .	87
3.11	Contour plots of the maximum growth rate ω_i for a wide range of values of the axial wavenumber k and axial flow parameter W_0 . The wing loading parameter equals (a) $n = 0.95$, (b) $n = 0.70$ and (c) $n = 0.50$. The other parameters remain fixed at $\varepsilon = 0.0625$ and $Re = 3180$. For each value of (k, W_0) , the growth rate of the most unstable resonance is shown. The contours are curves of constant growth rate and they are spaced 0.008 apart in each plot. Several contours have been labelled for clarity.	89
3.12	Partition diagram showing the most unstable resonant pair for every point in the (k, W_0) -plane for $n = 0.50$, $\varepsilon = 0.0625$ and $Re = 3180$. The corresponding growth rates are shown in Figure 3.11(c).	91
3.13	Perturbation isovorticity surfaces for a number of highly amplified modes for $n = 0.95$. The axial wavenumber equals (a) $k = 1.88$, (b) $k = 3.23$, (c) $k = 3.85$ and (d) $k = 4.57$, while the other parameters remain fixed at $\varepsilon = 0.0625$, $W_0 = 0.482$ and $Re = 3180$. Two isosurfaces, representing 25% and -25% of the maximum magnitude of the axial component of perturbation vorticity, are displayed in each plot. The shape of the surfaces is emphasized by thick isovorticity contours in the front plane.	92
3.14	Perturbation isovorticity contours for (a) $n = 0.70$ with $k = 1.75$ and (b) $n = 0.50$ with $k = 4.60$. The other parameter values are $\varepsilon = 0.0625$, $W_0 = 0.482$ and $Re = 3180$	93

LIST OF TABLES

2.1	For $m = -1$ and various values of n , the parameter values and growth rates of the most unstable perturbations identified and the critical value q_c of swirl for which stabilization occurs. The case $n = 1.00$ represents the results found by [66] for the Batchelor vortex.	45
2.2	A comparison of the results for the most unstable modes identified, for various values of n , for azimuthal wave numbers $m = -2, -3$ and -4 . The case $n = 1.00$ shows results found by [66] for the Batchelor vortex.	48
3.1	Code verification against published results for the Batchelor vortex for two cases of vortex instability. Case I is an unstable inviscid mode in the presence of viscosity for $Re = 1000$, $q = 0.761$, $m = -3$ and $k = 1.659$. Case II corresponds to an unstable viscous center mode for $Re = 14000$, $q = 2$, $m = -1$ and $k = 0.268$. The difference column presents the relative error (in percent) between the growth rate in every row and the next.	77

Background and outline

This dissertation has three parts. All three are manuscripts that were written for publication and can therefore be read independently of one another; each contains a detailed introduction, including an exhaustive literature review, and concluding remarks. Nonetheless, in this brief introductory section, we present a concise background for the results in this thesis, along with some key literature references. The objectives of the research program are outlined and we identify the topics which tie the three parts of the dissertation together.

Long nonlinear waves on a shear flow

Part 1 concerns long nonlinear surface waves in the presence of a variable current. The amplitude of these waves evolves according to the Korteweg-deVries (KdV) equation, which is discussed in Section 1.1. A broad review of the basic theory of parallel shear flows is presented in Chapter 4 of Drazin and Reid [24]. Many theoretical investigations have either neglected the effect of a current beneath the surface or else have taken it to be uniform. This is surprising since water waves on oceans and lakes often propagate on shear currents rather than on stagnant water. The nonlinear theory described in Burns [16] for long waves applies only to currents $\bar{u}(y)$ in which the vorticity is constant and the velocity depends linearly on the vertical coordinate y . In the latter part of his analysis, Burns formulated a linearized theory for streams which satisfy $\bar{u}'(y) > 0$ and $\bar{u}'' < 0$. He showed that under those assumptions the speed of propagation c of the surface wave is necessarily less than the minimum stream velocity or greater than the maximum stream velocity, thus excluding the possibility of a critical point y_c where $\bar{u}(y_c) = c$.

A study of solitary waves on a shear current with arbitrary vertical velocity distribution $\bar{u}(y)$, in the absence of a critical layer, was performed by Benjamin [9], thereby extending previous investigations to allow for rotational flow. Soon after that, Benney [10] took a non-steady approach, instead. In his paper, Benney derives time dependent equations for the development of long weakly non-linear waves and furnishes a systematic procedure for deriving higher order long wave equations. At first order in the expansion, one retrieves the KdV amplitude equation provided that the effects of wave-breaking and dispersion are

balanced. Section 1.2 contains details of the expansion up to first order. Then, in Section 1.3, we present the eigenvalue problem for the phase speed c that is associated with the lowest order terms in Benney's expansion.

In Part 1 of this dissertation, we will specifically be concerned with singular neutral modes that contain a nonlinear critical layer. A theory for these critical layers was formulated by Benney and Bergeron [11] and Davis [21]; nonlinear effects are included to deal with the singular nature of the Rayleigh equation near the singular point y_c . Importantly, dominance of nonlinear effects near the critical layer, in lieu of viscosity, implies the absence of a phase change across the critical layer for a neutral wave solution. In a geophysical setting, Redekopp [74] has found a Korteweg-deVries equation (or a modified KdV equation in the case of a stratified atmosphere) to govern solitary Rossby waves. Together with the work by Johnson, his results couple the nonlinear critical layer and solitary waves. For an overview, the reader is referred to Drazin and Reid [24] who discuss nonlinear critical layers on page 420 of their monograph. A more comprehensive presentation of critical layers in shear flows is given in the review article by Maslowe [63].

Our objective now is to solve the eigenvalue problem in order to determine the phase speed as a function of Froude number for a number of shear flow profiles. The numerical procedure used for computing singular solutions of the Rayleigh equation and their associated propagation speed is specified in Section 1.3.1. Then, in Section 1.4, we will find that these singular modes can be obtained for a variety of vertical velocity distributions such as boundary layer profiles of the Falkner-Skan similarity type, including the Blasius case. The appearance of a nonlinear critical wall layer is explained in Section 1.4.1.

The bridge to the next part of the dissertation, which deals with vortex flows instead of shear flows, is formed by the topic of critical layers. Several instances will be highlighted in the remainder of this introduction. As outlined above, critical layers play a prominent role in Part 1. Next, in the study of trailing vortex stability carried out in Parts 2 and 3, a critical layer singularity appears in the radial structure of the modes of instability of a vortical flow.

Stability of a trailing vortex

Part 2 constitutes, as far as we are aware, the first investigation of the inviscid linear stability of a trailing vortex using mean flow profiles given by an approximate solution of the Navier-Stokes equations found by Moore and Saffman [67].

A general introduction to vortex dynamics is given in the monograph by Saffman [78]. The book chapter by Ash and Khorrami [3] specifically develops vortex stability theory from basic principles and then discusses important contributions to the field. The linear stability of columnar vortices has seen much interest since the late 19th century. Notable early examples are Kelvin's study of the natural modes of oscillation of a column of rigidly rotating fluid and Rayleigh's sufficient condition for the stability of a rotating flow. Section 2.1 includes an extensive literature review. Here, we limit ourselves to considering two models for a rotating flow: the Rankine vortex and the Lamb-Oseen vortex. Neither model possesses linear modes of instability. However, the transition from an axial vorticity profile that is discontinuous (Rankine) to a smooth one (Lamb-Oseen) has implications for the waves that exist on these flows. Fabre, Sipp and Jacquin [31] have mapped and classified the normal modes of the Lamb-Oseen vortex. They make the point that the Lamb-Oseen model possesses singular, damped (critical-layer) modes in addition to neutral (Kelvin) waves. Only the latter exist in the case of a Rankine vortex. The occurrence of critical layer modes has several consequences; for example, with regards to Part 3 of this thesis, the damping incurred from the critical layer prevents a large number of possible resonant interactions from taking place in a pair of Lamb-Oseen vortices (Sipp and Jacquin [80]).

It has been known for many years from flight tests that aircraft trailing vortices contain strong axial flows [19]. These vortices linger in the wake of aircraft and the hazard they pose to oncoming air traffic severely limits the frequency of take-offs and landings at airports [81]. Accordingly, the inclusion of an axial mean flow makes the study of the stability of vortical flows more pertinent to the application of trailing wingtip vortices. Many authors have found the effect of an axial flow to be destabilizing: for example, superimposing a core axial velocity of constant magnitude on the Rankine vortex generates a single unstable

Kelvin-Helmholtz mode for every azimuthal wavenumber [60]. In the far field, *i.e.* many chord lengths behind the wingtip, mean flow profiles adapted from a paper by Batchelor [6] have been a frequent subject of investigation [58, 25, 66]. That model combines a Gaussian axial jet and a Lamb-Oseen azimuthal velocity component; the vortex is linearly unstable below a threshold strength of azimuthal velocity. In closer proximity behind the wingtip, where the roll-up of the vortex sheet shed by the wing is still in progress, the Batchelor vortex may not capture the shape of the velocity profiles. There, as stated by del Pino *et al.* [22], a family of similarity solutions to the Navier-Stokes equations established by Moore and Saffman [67] offers better agreement with experimental measurements. This is due in part to the fact that the model contains a parameter n , which depends on the wing loading. We define the Moore-Saffman mean velocity profiles in Section 2.2 and emphasize the effect of the wing loading parameter on the axial velocity component.

As regards the inviscid linear stability analysis performed in the second part of this dissertation, Howard and Gupta [43] derived a stability equation governing the radial velocity component of a non-axisymmetric perturbation to a columnar vortex in an inviscid fluid. This differential equation, and the numerical procedures we use to obtain solutions for it, are displayed in Section 2.3. The singular radius r_c of the stability equation, which corresponds to the location of the critical layer, must be taken into account in the computational routine by indenting the contour of integration into the complex plane. We further mention that Howard and Gupta proved a sufficient condition for the stability of a swirling flow which is an analog of the Richardson number 1/4 theorem for stratified shear flows. Other necessary or sufficient conditions for the linear stability of vortex flows exist under various restrictive assumptions (*e.g.* [83], [7] and [57]).

The objective is now to investigate the linear stability of the foregoing trailing vortex model proposed by Moore and Saffman. The results are presented in Section 2.4. Particularly of interest are growth rates for unstable perturbations for different values of n . The existence of modes of instability with various azimuthal wavenumbers m is examined. The unstable modes have critical layer singularities, a fact that necessitates indenting the path of numerical

integration for modes that are neutral and nearly neutral. Finally, we wish to compare the growth rates of the modes of instability to those for the Batchelor vortex. Section 2.5 provides concluding remarks. As noted there, an interesting avenue of research is to employ the Moore-Saffman model in a simulation of the short-wavelength cooperative instability that arises in a pair of trailing vortices. This problem is addressed in Part 3.

Elliptical instability of a vortex pair

In the third part of the thesis, we perform a numerical study of the elliptical instability of two counter-rotating vortices using the aforementioned Moore-Saffman mean flow velocity profiles.

After Crow's study of long-wave cooperative instability [20], at the start of the 70s, attention shifted somewhat to its short-wavelength counterpart. A comprehensive review of the relevant research that has been published since that time is presented in Section 3.1. Here, we touch on some key results. Following the analysis by Moore and Saffman [68], the mechanism responsible for the short-wave cooperative instability has been recognized to be a resonance between two normal modes of a vortex and an external strain field. The instability was analyzed by those two authors in the absence of axial flow, and, shortly after, by Tsai and Widnall [84] for a Rankine vortex. Ten years later, Pierrehumbert [72] and Bayly [8] formulated the instability mechanism in the more general framework of elliptical instability. More recently, the elliptical instability has been examined for a variety of vortex models, mostly in the absence of axial flow [27, 52, 55, 29] or with a simple axial mean velocity profile [49, 50, 76]. Amplified short-wavelength perturbations have been observed in co- and counter-rotating vortex pairs generated in water tank experiments (see, *e.g.*, [59, 26, 53]). The majority of these experiments did not include an axial mean flow, the exception being Roy *et al.* [75]. In addition, the observation of short-wavelength cooperative instabilities in aircraft wake (see, for example, Figure 1 in Bristol *et al.* [14]), and their role in the breakdown of aircraft wake vortices, provide a strong motive for further investigation. A review article, covering recent progress on the subject of elliptical instability, is due to Kerswell [47].

Motivated by the presence of axial flow in realistic trailing vortices, the topic of Part 3 of this thesis is the elliptical instability of a trailing vortex with Moore-Saffman mean velocity profiles. The features of this vortex model are summarized in Section 3.2.1. The general formulation differs from the one given in Part 2 in that it makes use of an axial flow parameter W_0 instead of a swirl parameter q . Section 3.2.2 is a brief overview of the inviscid stability characteristics of the Moore-Saffman vortex. Several aspects are highlighted such as the appearance of a critical layer singularity and the effect of viscosity on the inviscid modes of instability. Next, in Section 3.3.1, we formulate the equations that govern the evolution in time of a perturbation to a vortex that has been elliptically distorted by the presence of an external dipolar strain field. The method used in our numerical simulation is discussed in Section 3.3.2. For spatial discretization, we apply a spectral method in cylindrical coordinates. This is appropriate in our case because of the cylindrical geometry of the problem. Similarly to Matsushima and Marcus [64], we perform an expansion into algebraically mapped associated Legendre polynomials in the radial direction. This allows the pole condition at the origin to be satisfied exactly by all azimuthal modes. For time stepping, we employ a third order stiffly-stable splitting method by Karniadakis, Israeli and Orszag [46]. The computational routine was implemented in Fortran 95 using the OpenMP interface for parallel processing. In addition to a description of the numerical method, we make use of Section 3.3.2 to comment on some of the other approaches that exist for simulating the 3D incompressible Navier-Stokes equations (see Boyd [13] for a complete overview). The proper functioning of our code is verified in the ensuing section by comparing its output to published data.

The results of our numerical study are shown in Section 3.4. We obtain growth rates of unstable modes for a variety of values of the wing loading parameter n , axial flow parameter W_0 and the axial wavenumber k . Of particular interest are the values of k for which maximum amplification is attained. Additionally, we wish to map the dependency of the dominant pair of resonant azimuthal wavenumbers on W_0 . We compare our findings to those for the Batchelor vortex model.

Part 1

Long Nonlinear Surface Waves in the Presence of a Variable Current

In the first part of the thesis, which is a reproduction of Feys and Maslowe [33], we investigate the eigenvalue problem governing the propagation of long nonlinear surface waves when there is a current $\bar{u}(y)$ beneath the surface, y being the vertical coordinate. The amplitude of such waves evolves according to the KdV equation and it was proved by Burns [16] that their speed of propagation c is such that there is no critical layer (*i.e.*, c lies outside the range of $\bar{u}(y)$). If, however, the critical layer is nonlinear, the result of Burns does not necessarily apply because the phase change of linear theory then vanishes. We consider specific velocity profiles and determine c as a function of Froude number for modes with nonlinear critical layers. Such modes do not always exist, the case of the asymptotic suction profile $\bar{u} = 1 - e^{-y}$ being a notable example. We find, however, that singular modes can be obtained for boundary layer profiles of the Falkner-Skan similarity type, including the Blasius case. These and other examples are treated and we examine singular solutions of the Rayleigh equation to gain insight about the long wave limit of such solutions.

1.1 Introduction

The observation by Scott Russell of a solitary wave propagating down a canal and his subsequent experiments reported in 1838 generated an interest in long nonlinear waves that remains strong to this day. As is well known, Korteweg and deVries 57 years later derived the celebrated KdV equation that admits solitary wave solutions, as well as the periodic cnoidal waves. The essential feature of such an amplitude equation is a balance between dispersion and nonlinearity.

Until relatively recently, however, theoretical investigations assumed irrotational motion, either neglecting the effect of a current beneath the surface or else taking it to be uniform. This is surprising given the role of surface wind stress in generating water waves and the unlikelihood that bottom friction would allow the current to be uniform. These points were noted by Benjamin [9] who was the first to formulate a theory for solitary waves in the presence of a variable current.

The analysis of Benjamin, as in earlier related studies, employed a frame of reference moving at the speed of the solitary wave so that the flow would be steady. Benney [10], a few years later, presented a more general formulation that was time dependent and based on a two parameter expansion of A_t , where $A(x, t)$ is the amplitude and x is the direction of the wave propagation. If ε is a dimensionless amplitude parameter and μ^2 a measure of some characteristic length to the wavelength l , Benney's expansion of A_t has the form

$$A_t = -cA_x + \varepsilon 2rAA_x + \mu^2 sA_{xxx} + \dots \quad (1.1)$$

Although it is clear that to this order A satisfies the KdV equation, the method provides a systematic procedure for deriving higher order long wave equations. In addition to the shallow water example treated by Benjamin, Benney also showed how to recover earlier results from geophysical fluid dynamics, namely, internal waves in a stratified fluid and long waves in the presence of a Coriolis force in the framework of the beta plane approximation.

Returning now to the problem that is the focus of this part of the thesis, if h is the depth of the water and a the wave amplitude, then the two small parameters are $\varepsilon = a/h$ and $\mu^2 = (h/l)^2$. Clearly, these must be the same order of magnitude for the KdV equation to govern the amplitude evolution. The expressions for the coefficients of the nonlinear and dispersive terms, r and s , respectively, depend on $\bar{u}(y)$ and they turn out to be the same as those derived earlier by Benjamin in the steady case. However, before even considering the dispersive and nonlinear terms, there is a linear eigenvalue problem that must be solved to determine the phase speed c . The details will be given in Sections 2 and 3; briefly, though, the Rayleigh equation must be solved in the long wave limit subject to free surface conditions and the vanishing of the vertical velocity at $y = 0$, the bottom. The solution of this eigenvalue problem was first obtained by Burns [16], who showed that c is determined by the relation

$$\int_0^1 \frac{dy}{(\bar{u}(y) - c)^2} = \frac{1}{G}, \quad (1.2)$$

where $G = gh/U^2$ is an inverse Froude number, U is a characteristic velocity of the mean flow and y has been scaled with the depth h .

If there is a critical point y_c , where the denominator of the integrand in (1.2) vanishes, then the integral does not exist in any conventional sense. The eigenvalue problem is then singular and it must be approached by methods used to investigate neutral modes in the context of hydrodynamic stability. Rather than solving (1.2), the Rayleigh equation can be integrated numerically, satisfying the boundary conditions and using Frobenius series to cross y_c . Burns, in proving that c lies outside of the range of $\bar{u}(y)$, dealt with particular forms for the velocity profile and derived his conclusions from the integral condition (1.2). Yih [88], on the other hand, reexamined the inviscid theory of hydrodynamic stability when the upper boundary conditions are those for a surface wave. He showed that considerations based on the variation of the Reynolds stress are unchanged by having a free surface rather than a wall as the upper boundary. Specifically, the Reynolds stress is constant for a neutral mode and it is zero on both boundaries. It follows that within the context of linear theory, neutral modes cannot exist for monotonic velocity profiles unless $\bar{u}(y)$ has an inflection point. Otherwise, there would be a jump in the Reynolds stress that is incompatible with the foregoing conditions.

The classical theory leads to a discontinuity in the Reynolds stress by concluding that a singular neutral mode should be interpreted as the limit of a linearly unstable mode whose amplification rate goes to zero. There is, however, a more recent alternative and that is to employ a nonlinear critical layer. In that approach, Benney and Bergeron [11] and Davis [21] both showed that there is no phase change across an inviscid nonlinear critical layer of thickness $O(\varepsilon^{1/2})$ and, as a consequence, the Reynolds stress is continuous. The nonlinear approach is the appropriate one at large Reynolds number Re is $\varepsilon^{1/2} \gg (Re)^{-1/3}$. Interestingly, the idea that nonlinearity might be more appropriate than viscosity to deal with the critical layer in the present context was proposed in an authoritative survey article on water waves by Peregrine [70] (p. 83). However, he apparently did not pursue this approach nor did he cite [11] or [21].

There is only one paper of which we are aware that employs a nonlinear critical layer in studying the propagation of a surface wave whose amplitude evolution is governed by the

KdV equation. In that study, Johnson [45] focused on detailed aspects of the flow structure within the critical layer and how they relate to particular solutions of the KdV equation. For example, the treatment of regions of closed flow is considered in some detail; that was also an issue that received considerable attention in both [11, 21]. The latter studies dealt with periodic modes having a cats-eye structure, whereas the investigation by Johnson was concerned more with solitary waves. In that respect, it is reminiscent of Redekopp's analysis of solitary Rossby waves on the beta plane [74]. Results are presented in [45] in which, for example, a single cat's-eye is obtained as the outcome when $A(x, t)$ is given by the two-soliton solution of the KdV equation.

Our own study, in contrast with that of [45], deals only with the eigenvalue problem determining the phase speed c . In the language of matched asymptotic expansions, we are concerned with the outer problem. Johnson did not completely ignore the outer problem. He remarked, for example, that the Burns condition (1.2) would apply if the integral is interpreted using the notion of a Hadamard finite part [40]. This would be valid if the critical layer solution is symmetric about y_c . That does not guarantee, however, that a solution of (1.2) can be found for a particular velocity profile and a specific value of G . In the following section, we formulate the problem in a more general way that does not employ the Burns integral and, therefore, the critical layer structure is not required to be symmetric. Both the vorticity equation and the free surface conditions are developed in some detail. Then, in Section 3, the eigenvalue problem is formulated and the numerical procedure we use to solve it is described. Finally, in Section 4, we present numerical solutions for the dispersion curves, essentially the variation of c with inverse Froude number, for various velocity profiles of the boundary layer type. The case where the critical layer is close to the wall is also considered.

1.2 Formulation of the outer problem

We consider the two-dimensional flow of a current of depth h over a solid boundary at $y^* = 0$ and with a free surface at $y^* = h + \eta^*(x^*, t^*)$ or $y = 1 + \varepsilon\eta(x, t)$, after nondimensionalizing

with respect to h . The only characteristic length in the x -direction is the wavelength l , presumed large, so must set $x = x^*/l$ and the dimensionless time $t = (U/l)t^*$. The scaling that we employ for the dependent variables is the same as in Benney [10] and, as pointed out there, the two velocity components u and v must be nondimensionalized differently to preserve the continuity equation at lowest order. The dependent variables are scaled as follows:

$$u = \frac{u^*}{U}, \quad v = \frac{v^*l}{Uh}, \quad p = \frac{p^*}{\rho_0gh}, \quad \text{and} \quad \eta = \frac{\eta^*}{a}, \quad (1.3)$$

where the density of the water ρ_0 is taken constant. To describe the flow beneath the surface, it is most convenient to solve the vorticity equation after first introducing a stream function $\psi(x, y)$, where $u = \psi_y$ and $v = -\psi_x$. However, because free surface problems involve a pressure condition, it is helpful in formulating that condition to use the momentum equations. As in [10], we use a combination of these approaches, *i.e.*, the vorticity equation to describe the main body of the flow and the momentum equations to impose the free surface pressure condition.

To begin, we consider a perturbation of $O(\varepsilon)$ to the mean flow whose stream function and pressure are $\bar{\psi}$ and \bar{p} , so that

$$\psi = \bar{\psi}(y) + \varepsilon\hat{\psi}(x, y, t) \quad \text{and} \quad p = \bar{p}(y) + \varepsilon\hat{p}(x, y, t). \quad (1.4)$$

The perturbation quantities associated with the wave motion, *i.e.*, $\hat{\psi}$, \hat{p} and η are all expanded in powers of ε and μ^2 ; for example

$$\hat{\psi}(x, y, t) \sim \psi^{(0,0)} + \varepsilon\psi^{(1,0)} + \mu^2\psi^{(0,1)} + \varepsilon\mu^2\psi^{(1,1)} + \dots \quad (1.5)$$

The vorticity equation governing the perturbed flow then takes the form

$$\begin{aligned} & (\hat{\psi}_{yt} + \bar{u}\hat{\psi}_{xy} - \bar{u}'\hat{\psi}_x)_y + \varepsilon(\hat{\psi}_y\hat{\psi}_{xy} - \hat{\psi}_x\hat{\psi}_{yy})_y \\ & + \mu^2(\hat{\psi}_{xxt} + \bar{u}\hat{\psi}_{xxx}) + O(\varepsilon\mu^2) = 0. \end{aligned} \quad (1.6)$$

Along the lower boundary, the condition to be imposed is that $\hat{\psi}_x(x, 0, t) = 0$, whereas both a kinematic and a pressure condition must be imposed at the free surface $y = 1 + \varepsilon\eta(x, t)$.

The kinematic condition requires that

$$\frac{D}{Dt}(1 + \varepsilon\eta - y) = 0, \quad (1.7)$$

where $D/Dt = \partial/\partial t + (\mathbf{q} \cdot \nabla)$, and substitution of (1.4) into (1.7) yields

$$\{\eta_t + \bar{u}\eta_x + \hat{\psi}_x + \varepsilon\hat{\psi}_y\eta_x\}_{y=1+\varepsilon\eta} = 0. \quad (1.8)$$

The pressure condition is not so easy to formulate as in the irrotational case where a Bernoulli integral exists. Given that the free surface is a streamline, along which the pressure is constant, it is convenient to write

$$\left(\frac{\partial p}{\partial x}\right)_\psi = \left(\frac{\partial p}{\partial x}\right)_y + \left(\frac{\partial p}{\partial y}\right)_x \left(\frac{\partial y}{\partial x}\right)_\psi = \left(\frac{\partial p}{\partial x}\right)_y + \left(\frac{\partial p}{\partial y}\right)_x \varepsilon \eta_x = 0. \quad (1.9)$$

Expressions for the pressure derivatives required by (1.9) can be obtained directly from the horizontal and vertical momentum equations, namely,

$$\hat{\psi}_{yt} + \bar{u}\hat{\psi}_{xy} - \bar{u}'\hat{\psi}_x + \varepsilon(\hat{\psi}_y\hat{\psi}_{xy} - \hat{\psi}_x\hat{\psi}_{yy}) = -G \hat{p}_x \quad (1.10)$$

and

$$-\mu^2(\hat{\psi}_{xt} + \bar{u}\hat{\psi}_{xx}) + O(\varepsilon\mu^2) = -G(p_y + 1). \quad (1.11)$$

After expanding all quantities in Taylor series about $y = 1$, $\hat{\psi}$ and p must also be expanded in powers of ε and μ^2 , as in (1.5). We do not write the final expression here because in this study we consider only the eigenvalue problem determining c for various velocity profiles and values of G . However, the pressure condition at an interface for weakly nonlinear modes with $O(1)$ wavelength is given by (2.11) of Balagondar, Maslowe, and Melkonian [5].

1.3 The eigenvalue problem

For a given Froude number G , the propagation speed c is determined by solving an eigenvalue problem in which the governing equation is the lowest order vorticity equation (*i.e.*, $\varepsilon = \mu^2 = 0$). Substituting (1.5) into (1.6) and integrating with respect to y , we obtain

$$\hat{\psi}_{yt}^{(0,0)} + \bar{u}\hat{\psi}_{xy}^{(0,0)} - \bar{u}'\hat{\psi}_x^{(0,0)} = f(x, t). \quad (1.12)$$

The method developed by Benney, being a weakly nonlinear approach, involves a separation of variables at each order. To accomplish this in (1.12), we let $\hat{\psi}^{(0,0)} = \phi(y)A(x, t)$ and the amplitude equation governing $A(x, t)$ at lowest order is taken to be the linear wave equation

$$A_t = -c A_x. \quad (1.13)$$

It remains now to determine the function $f(x, t)$ such that an ODE for $\phi(y)$ is obtained from (1.12).

Equation (1.12) is, of course, the linearized horizontal momentum equation and comparison with (1.11) makes it clear that $f(x, t) = -G p_x^{(0,0)}$. We must therefore obtain an expression for the pressure to determine $f(x, t)$. The $O(\varepsilon)$ pressure is obtained most easily from the right hand side of (1.11). It turns out that both the mean pressure \bar{p} and lowest order perturbation $p^{(0,0)}$ must be considered. Noting that the left hand side of (1.11) is negligible at this order, we see that $\bar{p}' = -1$ and that $p^{(0,0)}$ is independent of y . The free surface condition (1.9) can therefore be used to conclude that

$$p_x^{(0,0)} = \eta_x^{(0,0)} \quad \text{and we can write} \quad p^{(0,0)} = \eta^{(0,0)} = \lambda A(x, t), \quad (1.14)$$

where λ is an arbitrary constant. Employing (1.14) now with (1.12), we see that

$$f(x, t) = -G p_x^{(0,0)} = -\lambda G A_x. \quad (1.15)$$

After substituting (1.13) and (1.15) into (1.12), the first-order ODE that results can be integrated to obtain

$$\phi = -\lambda G (\bar{u} - c) \int_0^y \frac{d\eta}{[\bar{u}(\eta) - c]^2}, \quad (1.16)$$

where the limits of integration have been chosen to satisfy the BC at $y = 0$. The only condition that we have yet to impose is (1.7), the kinematic condition at the free surface. At lowest order, we use (1.14) to replace $\eta^{(0,0)}$ and the wave Equation (1.13) can then be employed to achieve separation of variables. The result can be written

$$\phi(1) = -\lambda[\bar{u}(1) - c], \quad (1.17)$$

and if we use this value for $\phi(1)$ in (1.16), the eigenvalue condition (1.2), obtained by Burns, is recovered.

1.3.1 Numerical procedure for singular modes

The procedure described earlier is appropriate when there is no critical layer because the integral in (1.16) is determined uniquely. However, for singular modes, it is preferable to deal with the zeroth order vorticity equation which, after using (1.13) to separate variables, leads to the Rayleigh equation with wavenumber zero, namely,

$$(\bar{u} - c)\phi'' - \bar{u}''\phi = 0. \quad (1.18)$$

The procedure that we have used to solve the eigenvalue problem involves integrating (1.18) towards the critical layer first, from the upper, and then the lower boundary. Near the critical layer, these solutions are then matched to the series solutions first determined by Tollmien. Using the method of Frobenius, the solution of (1.18) can be expressed as a linear combination of the two power series

$$\begin{aligned} \phi_A &= (y - y_c) + \frac{\bar{u}_c''}{2\bar{u}_c'}(y - y_c)^2 + \dots \quad \text{and} \\ \phi_B &= 1 + \dots + \frac{\bar{u}_c''}{\bar{u}_c'}\phi_A \log(y - y_c) + \dots \end{aligned} \quad (1.19)$$

It was shown by Benney and Bergeron [11] that matching to the nonlinear critical layer requires that for $y < y_c$, we write $\log(y - y_c) = \log|y - y_c|$. That condition allows us to relate the numerical solutions above and below y_c and thereby solve the eigenvalue problem using the following procedure.

To begin the downward integration from $y = 1$, we first determine a single BC by combining the two free surface conditions. First, the pressure condition is obtained from (1.12), as described earlier, and the kinematic condition (1.17) can then be used to replace λ . This leads to the upper boundary condition

$$\phi'(1) - \left[\bar{u}'(1) + \frac{G}{\bar{u}(1) - c} \right] \frac{\phi(1)}{\bar{u}(1) - c} = 0. \quad (1.20)$$

It is convenient to choose $\phi(1) = 1$ as the arbitrary constant in the eigenvalue problem. Using a Runge-Kutta method, (1.18) is integrated downward to a value $y_c + \delta$, where δ is

a small number that can be determined by trial and error. We then match the numerical solution to the Frobenius series at this point and write

$$\phi(y_c + \delta) = A^+ \phi_A(y_c + \delta) + B^+ \phi_B(y_c + \delta)$$

and

$$\phi'(y_c + \delta) = A^+ \phi'_A(y_c + \delta) + B^+ \phi'_B(y_c + \delta).$$

The constants A^+ and B^+ can now be determined using Cramer's rule.

The procedure is then repeated, integrating this time from the lower boundary to $y_c - \delta$. The situation with respect to the boundary conditions is, however, slightly different. We know that $\phi(0) = 0$, but $\phi'(0)$ must be determined; it can be taken as unity during the first integration and values obtained for A^- and B^- . From the Frobenius solutions (1.19), it is clear that ϕ is continuous at y_c , so $\phi'(0)$ can then be adjusted for the second integration so that $B^- = B^+$. Evaluating ϕ' above and below the critical layer using (1.19) with the logarithm in ϕ_B written as $\log|y - y_c|$, leads to the conclusion that $A^- = A^+$. In general, however, this will not be the case, so an iteration procedure must be employed in which c is varied until the two values of A agree. We have imposed this eigenvalue condition by requiring that $\left| \frac{A^+}{B^+} - \frac{A^-}{B^-} \right| < 10^{-5}$. The results presented in the following section have been obtained using this procedure. Before presenting our computational results, we derive a result for $\phi(y_c)$ that can be used to assess the accuracy of the computations. Substituting (1.17) into (1.16) to eliminate λ , we obtain

$$\phi(y) = \frac{\phi(1)G(\bar{u}(y) - c)}{\bar{u}(1) - c} \int_0^y \frac{d\eta}{[\bar{u}(\eta) - c]^2}. \quad (1.21)$$

The lower limit of the integral having been chosen to satisfy the BC at $y = 0$, let us suppose that $y < y_c$. As $y \rightarrow y_c$ from below, the integral becomes infinite and $(\bar{u}(y) - c) \rightarrow 0$. That being the case, we can use l'Hôpital's rule to find that

$$\phi(y_c) \rightarrow -\frac{G}{\bar{u}'_c(1 - c)}, \quad (1.22)$$

where we have employed the normalization $\phi(1) = \bar{u}(1) = 1$. Our computational results for the constant B were always within 1% of (1.22).

1.4 Numerical results for various velocity profiles

Our expectations for the existence of singular modes were guided to some extent by the corresponding solutions of the Rayleigh equation obtained by Benney and Bergeron [11]. It turned out, however, that the free surface boundary conditions can change the outcome substantially. For example, we began with the case of the asymptotic suction profile $\bar{u} = 1 - e^{-y}$ because Benney and Bergeron, for the same profile, found singular mode solutions for a range of wavenumbers that extended from, roughly, $k = 0.8$ to $k \rightarrow 0$. We discovered to our surprise, however, that long surface waves with nonlinear critical layers do not exist for this profile. To better understand this, we solved the Rayleigh equation for singular neutral modes with a free surface and we discovered that such solutions exist only for relatively short waves. Presentation of the latter results will be deferred until the end of this section because our focus here is on long waves.

The first velocity profiles for which we did find the nonlinear critical layer modes sought in this study involved the function $\tanh(\gamma y), y \geq 0$. For such profiles, more familiar in the context of free shear layers, even though $\bar{u}''(0) = 0$ the flow is stable according to Fjørtoft's theorem. That is because the vorticity at $y = 0$ is not a relative maximum. More generally, we considered the normalized family of profiles

$$\bar{u} = (u_0 + \tanh(\gamma y))/u_n, \quad (1.23)$$

where $u_n = u_0 + \tanh \gamma$. We begin the presentation of our computational results by showing in Figure 1.1 the variation of c with the inverse Froude number G for the velocity profile $\bar{u} = \tanh(3y)/\tanh 3$. It can be seen that c is greatest when the inverse Froude number is small (*i.e.*, $U^2 \gg gh$) and it decreases rapidly before leveling off at a value of approximately $c = 0.29$ for $G > 5$.

Following our determination of the dependence of c on the Froude number for a representative value of γ , as exemplified by the results in Figure 1.1, we attempted to find singular modes having small positive values of c . To do this, we employed the profile (1.23) and varied G , u_0 and γ . Our motivation was, in part, to compare with the nonsingular

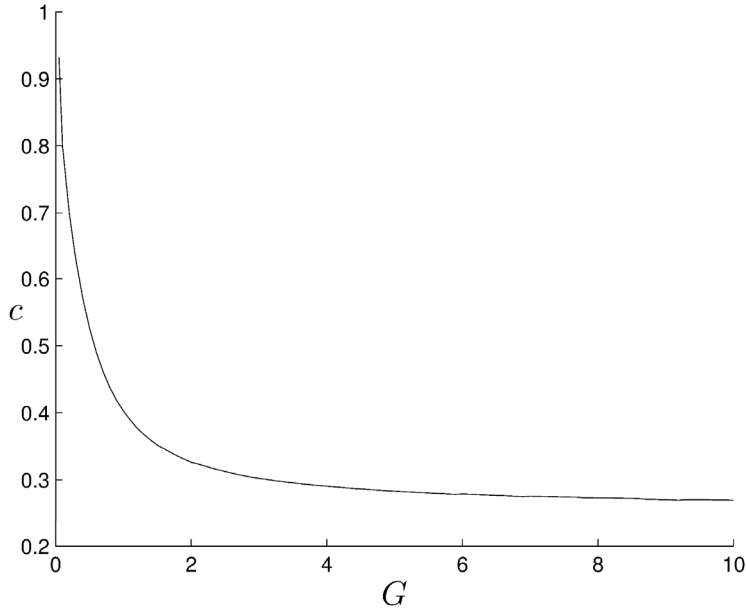


Figure 1.1: Dispersion curve showing phase speed vs. inverse Froude number for the velocity profile $\bar{u} = \tanh 3y / \tanh 3$.

case because, in both [16] and [70], analyses are presented for modes having either $c = 0$ or slightly less than 0. An entire section of [70] is, in fact, devoted to an investigation of the family of profiles $\bar{u}'' = \alpha \bar{u}$, where $c = 0$ and α is a constant. Only nonsingular modes could be treated, however, so that it was necessary to restrict attention to profiles for which either there is no critical point where $\bar{u} = c$ or else $\bar{u}''(y_c) = 0$. With the use of a nonlinear critical layer, on the other hand, it is possible to greatly expand the number of possibilities, as we now discuss.

1.4.1 The nonlinear critical wall layer

In the classical stability theory of shear flows, it is known that the critical and wall layers merge along the lower branch of the neutral curve (see, *e.g.*, Figure 4.5 of Drazin and Reid [24]). As the Reynolds number $Re \rightarrow \infty$, $c \sim k^2$, so it would appear that in a study of long waves, the case of a critical layer near the wall is pertinent. We must recall though that the foregoing result is derived from the Orr-Sommerfeld theory with the upper boundary

conditions not being those for a free surface. Therefore, its pertinence to cases where the critical layer is nonlinear must be reassessed. When the critical layer is not near the wall, the constants A and B multiplying the Frobenius solutions (1.19) were both assumed to be $O(1)$ in the eigenvalue computations reported by Benney and Bergeron [11]. As discussed below, we cannot assume that such is the case when the critical layer is near the wall.

The thickness of the nonlinear critical layer when it is near the wall remains $O(\varepsilon^{1/2})$. The primary difference however, compared with the case when y_c is in the interior of the fluid, is that A can be much greater than B . The nonlinear critical layer theory for that case was formulated by Finlay, Liu and Maslowe [35]; as in [11], B was assumed to be $O(1)$. However, A , the constant multiplying the regular Frobenius solution, was taken to be $O(\varepsilon^{-1/2})$ so that $A(y - y_c)$ is $O(1)$ near the critical layer.

The governing equation in the critical layer according to [35] is given, at lowest order, by

$$\Psi_Y \Psi_{YY\theta} - \Psi_\theta \Psi_{YY} = \lambda \Psi_{YYY}, \quad (1.24)$$

where $\Psi(\theta, Y) = (\varepsilon \bar{u}'_c)^{-1} \psi(\theta, y)$, $Y = (y - y_c)/\varepsilon^{1/2}$, $\theta = kx$, and $\lambda^{1/3}$ is the ratio of the viscous to the nonlinear critical layer thickness. Solutions of (1.24) were obtained numerically in [35] for various values of λ and streamline patterns were computed showing the influence of the wall. Here, we are interested primarily in large Reynolds number flows, so it is worth recalling [35] that a solution of (1.24) in the inviscid limit, $\lambda = 0$, is given by

$$\Psi = \frac{Y^2}{2} + (Y + Y_0) \cos \theta, \quad (1.25)$$

where the inviscid BC $\Psi_\theta = 0$ is satisfied at the wall, $Y = -Y_0 = -y_c/\varepsilon^{1/2}$. The same analysis could be used to treat the long wave case that is the subject of this part of the thesis. The only modification to the solution (1.25) would be to replace $\cos \theta$ with $A(x - ct)$.

A glance at (1.25) reveals that the difference compared with the solution in [11] and [21], yielding the cat's-eye streamline pattern, is the presence of an additional term proportional to Y . We, therefore, have tried to find velocity profiles yielding eigensolutions consistent with the assumptions implicit in the wall layer theory, namely, a relatively small value of y_c

and $|A| \gg |B|$. To that end, we have investigated the family of profiles described by (1.23). As mentioned earlier, we varied G, u_0 and γ . Suppose as a reference point, we consider the value $G = 1.0$ in Figure 1.1 with $\gamma = 3.0$ and $\varepsilon = 0$. As shown in this figure, c decreases with increasing G . As for the other parameters, it turned out that smaller values of c are obtained by increasing γ and u_0 . (A nonzero choice for u_0 violates the no-slip condition; however, our analysis is inviscid, so this is permissible.)

At the reference point where $G = 1.0$, we found that $c = 0.4353$ and the critical point $y_c = 0.1546$. This is well outside the wall layer and $|B/A| = 5.16$, so the singular Frobenius solution is dominant. Let us now compare these values with those for a wall layer case. If we set $u_0 = 0.1$, $\gamma = 3.5$ and $G = 1.8$, we obtain $c = 0.3646$ and $y_c = 0.0885$. For these values, ε could be as small as 0.01 and the nonlinear wall layer theory would still be applicable provided, of course, that the Reynolds number was large. The remaining question concerns the magnitude of the constant multiplying the regular Frobenius solution. For this case, $|A/B| = 4.9705$ which more or less confirms the scaling in [35]. To support the basic idea, the ratio of $|A|$ to $|B|$ is larger by a factor of 25.6 compared with the reference point, $G = 1.0$.

1.4.2 Falkner-Skan boundary layer profiles

The Falkner-Skan similarity solution of the boundary layer equations is valid for flows subject to a streamwise pressure gradient when the velocity varies according to $\bar{u} \sim x^m$. The velocity profiles are obtained by solving the ordinary differential equation

$$f''' + ff'' + \beta(1 - f'^2) = 0, \quad (1.26)$$

where $\beta = 2m/(m+1)$. The velocity component parallel to the wall is given by $f'(\eta)$ and η is a similarity variable (see Section 4.2 of [82] for details). When $\beta = 0$ the Blasius solution for a flat plate is recovered and a separation profile results when $\beta = -0.1988$.

We have computed dispersion curves for a wide range of pressure gradients, both favorable and adverse. Several of these are illustrated in Figure 1.2, ranging from $\beta = 0.2$ to $\beta = -0.14$.

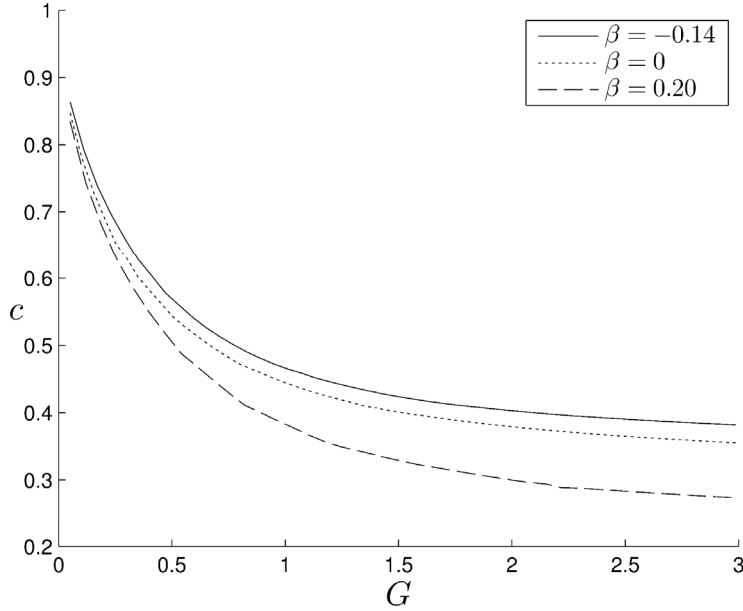


Figure 1.2: Dispersion curve of phase speed vs. inverse Froude number for different stream-wise pressure gradients.

The qualitative behavior of c with increasing G is similar to that of the $\tanh y$ profile. There are, however, some surprising variations with pressure gradient that for clarity we do not show in Figure 1.2.

Because c reaches a maximum at some value of β , certain dispersion curves would intersect had they been included in Figure 1.2. This problem in visualization can be avoided if we consider the variation of c with β while holding G constant. At a fixed value of G , c typically increases from its flat plate value with decreasing β , reaching a maximum, and it then decreases rapidly. This can be seen clearly in Figure 1.3, corresponding to $G = 1.0$, where the maximum value of c is reached near $\beta = -0.12$; c then decreases rapidly until a value of β is reached close to that associated with boundary layer separation.

The results in Figure 1.3 suggest that for positive β the critical layer and wall layer may merge. Not only does c decrease with increasing β , but the change in the velocity profile when the pressure gradient is favorable increases the likelihood of that happening. To demonstrate this point, consider the computational results for the case $\beta = 0.20$ and

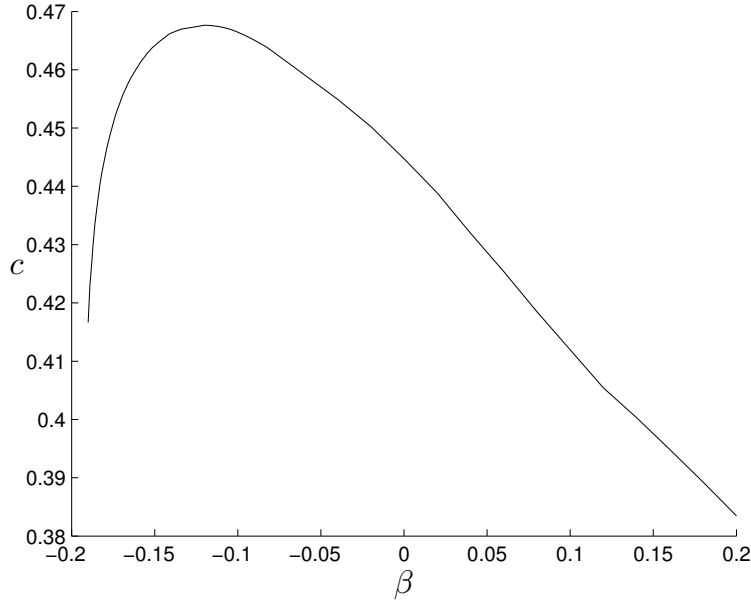


Figure 1.3: Variation of phase speed with streamwise pressure gradient at a constant inverse Froude number, $G = 1.0$.

$G = 3.0$. We find that $c = 0.2733$ and the corresponding value of $y_c = 0.0705$; for moderate to high Reynolds numbers, this is clearly in the nonlinear wall layer régime.

1.4.3 Singular solutions of Rayleigh's equation with a free surface

The computations presented in this section were motivated by our failure, noted above, to find long wave solutions for the asymptotic suction profile. We wondered if the nonexistence of such solutions could have been anticipated from the behavior, as $k \rightarrow 0$, of nonlinear critical layer solutions of the Rayleigh equation

$$(\bar{u} - c)(\phi'' - k^2\phi) - \bar{u}''\phi = 0. \quad (1.27)$$

To better understand the situation, we computed solutions of (1.27) for singular modes in the two cases of the Blasius profile and the asymptotic suction layer. In Figure 1.4, the free surface solutions are shown along with those obtained by Benney and Bergeron [11].

In agreement with the results presented in [11], we see that there are solutions for both

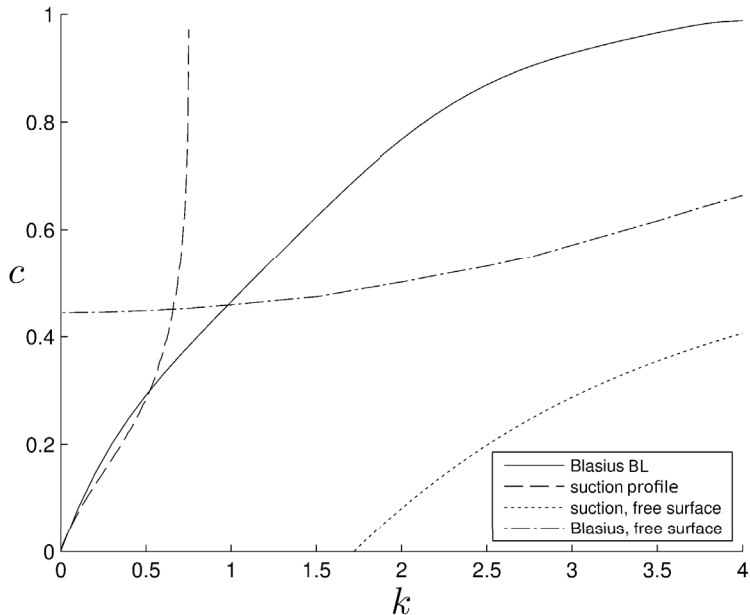


Figure 1.4: Singular solutions of the Rayleigh equation for the Blasius boundary layer and the asymptotic suction profile at a constant inverse Froude number, $G = 1.0$.

profiles in the usual semi-infinite case, as $k \rightarrow 0$. The obvious difference is that the curvatures of the dispersion curves are of opposite sign, so that waves having $k \sim O(1)$ exist for the Blasius profile, but not for the asymptotic suction boundary layer. More pertinent from the standpoint of this investigation, however, is that when there is a free surface, long wave solutions exist for the Blasius flow, but not for the asymptotic suction profile. We cannot conclude, however, from only two examples that long wave free surface modes exist for a particular profile only if solutions of the Rayleigh equation are possible as $k \rightarrow 0$. The discontinuity in density at a free surface is absent in the continuous case. And the scaling is different, so it is not true that the semi-infinite continuous case is recovered simply by setting $G = 0$ in (1.21). On the other hand, our results illustrated in Figure 1.4 are unlikely to be a coincidence, so the question does deserve further thought.

Finally, we remark that even in the framework of linear stability theory, there have been few computations reported for continuous shear flows with a free surface. Morland et al. [69] have investigated the stability of three velocity profiles, only two of which were smooth. In

both cases, the neutral modes at marginal stability did not have critical layers. In fact, one of these, the exponential profile, is a particular case of the class of solutions having $c = 0$ that were described in [70] and mentioned immediately before Section 4.1. Clearly, there is room for further stability investigations and it would be interesting to see if the stability boundary for some profile could be a singular neutral mode.

1.5 Concluding remarks

Every swimmer and boating enthusiast knows that currents occur in the ocean and other large bodies of water. Yet, the presence of these currents has been largely ignored in most papers dealing with the theory of water waves. Even in those papers that did account for them, the currents were often assumed to be uniform or irrotational. Such an assumption is unlikely to be realistic, as pointed out more than 40 years ago by Benjamin [9]. This observation was repeated in the survey article by Peregrine [70].

In this part of the thesis, we deal specifically with a class of modes propagating on currents that are not only rotational, but the modes propagate with a phase speed such that a critical layer is present. This possibility would seem to be excluded according to a result proved by Burns [16], as we discussed in Section 1.1; indeed, that is the case within the framework of linear theory. Peregrine appears to have been not only the first to consider the existence of critical layer modes but he mentioned, in passing, that at high Reynolds numbers a nonlinear critical layer would be the appropriate choice to resolve the associated singularity in the linear eigenvalue problem. It was not, however, until the paper by Johnson [45] that such a development was actually carried out. (Apparently, without knowledge of Peregrine's suggestion, *i.e.*, [70] is not cited by Johnson.)

The analysis of [45] is more in the spirit of Davis [21] than that of Benney and Bergeron [11] in that unsteadiness, rather than viscosity, is used to determine the streamline patterns in regions of closed flow. This was more feasible in [45] than in [21] thanks to the approximations that can be employed in the context of long waves. Consideration of the eigenvalue

problem, however, is still necessary to determine c in the Korteweg-deVries equation. This is the focus of our investigation and we have computed dispersion curves for currents having velocity profiles of boundary layer type. In the case of a favorable pressure gradient, we have found that the critical layer is likely to be near the wall. Streamline patterns at lowest order were computed in [35], but the solution should be carried out to higher order to match with the logarithmic term in the Frobenius expansion (1.19). With regard to future investigations, a direct numerical simulation of the unsteady problem for long waves would clearly be worthwhile. A comparison of the streamline patterns with those determined employing the KdV equation in [45] would be of particular interest.

Part 2

Linear Stability of the Moore-Saffman Model for a Trailing Wingtip Vortex

The content of the second part of the dissertation was taken from Feys and Maslowe [34]. It presents an investigation of the stability of a trailing vortex using mean flow profiles given by an approximate solution of the Navier-Stokes equations. The axial and tangential velocity profiles obtained from this solution, deduced by Moore and Saffman, agree well with experiments involving wings at slight angles of attack. In particular, the Moore-Saffman profiles better describe the jet-like and wake-like axial flows near the center of the vortex than does the much-studied Batchelor vortex. We determine solutions numerically for these profiles and find that they are well suited to describe the flow at short and intermediate distances behind the wingtip. Growth rates for unstable perturbations are presented for different values of n , the wingtip loading parameter. These growth rates are shown to be somewhat larger than those obtained for the Batchelor vortex, and instability persists for larger values of the swirl. The largest amplification rates were found to occur near $n = 0.5$, the value corresponding to elliptic loading. This is within the range $0.44 < n < 1.0$, where the core axial flow is wake-like. For $n < 0.44$, the flow in the vortex core is jet-like and the growth rates of unstable perturbations become progressively smaller, with all modes damped for $n \approx 0.25$.

2.1 Introduction

The recent introduction of larger more powerful jetliners like the A380 has again brought attention to the study of the stability of the trailing wingtip vortex. A similarity solution for an aircraft trailing vortex, valid far downstream of the wingtip, was found by Batchelor [6]. Its stability has been the focus of many papers, beginning with Lessen, Singh and Paillet [58]. Motivated by experiments reported recently by Lee and Pereira [56], we consider a family of profiles based on the formulation of Moore and Saffman [67] that better describes the axial flow near and inside the core of the vortex. After computing velocity profiles corresponding to various wing loadings, we present stability calculations for the vortex model with Moore-Saffman axial mean flow and a number of azimuthal velocity profiles. First, though, let us briefly review some results on the stability of swirling flows.

The inviscid stability of a rotating flow with azimuthal velocity $V(r)$ and no axial flow was investigated by Rayleigh in 1916. It was only 7 years later that the subject began to attract considerable attention because of its relevance to the celebrated Taylor vortices. Rayleigh showed that a sufficient condition for stability is that the square of the circulation increases in the radially outward direction for all r . Specifically, his theorem requires that the Rayleigh discriminant $\Phi = r^{-3}d(rV)^2/dr \geq 0$. Synge generalized this result using Sturm-Liouville theory to show that Φ being negative anywhere is a sufficient condition for centrifugal instability. Recently, the latter result was extended to include non-axisymmetric disturbances by Billant and Gallaire [12]. Their analysis applies to eigenfunctions having two turning points, although this is not a necessary condition for instability.

The vortical flows of interest in this part of the thesis include an axial mean flow $W(r)$ in addition to the swirl component $V(r)$. The stability of such flows was treated by Howard and Gupta [43] who were able to combine the 4 equations governing the linear theory to obtain a single ordinary differential equation (ODE) for $u(r)$, the r -component of the radial velocity. For axisymmetric perturbations, this second order differential equation is the analogue of the Taylor-Goldstein equation governing stratified shear flows and a stability criterion equivalent to the Richardson number $1/4$ theorem was proved in [43]. Specifically, it was shown that a sufficient condition for stability is that $\Phi - \frac{1}{4}W'^2$ be everywhere non-negative. For non-axisymmetric disturbances, however, it was found that instability is always possible for modes whose wavelength is sufficiently long in the axial direction and only a bound on the growth rate could be obtained. Stability computations for particular examples have since confirmed that non-axisymmetric modes are indeed the most unstable.

In studies of the stability of trailing vortices, the swirl component $V(r)$ is often viewed as being a stabilizing influence on an unstable axial flow $W(r)$. (Rotating pipe flow provides a counter-example [62], but in the case of the trailing vortex, we may view the swirl as stabilizing.) The Rankine vortex is the simplest model for the swirl component and modal solutions corresponding to that profile are termed Kelvin waves. The monograph by Saffman [78] presents dispersion curves for different azimuthal wavenumbers. A more realistic rep-

resentation of a vortex, because its vorticity is continuous, is provided by the Lamb-Oseen vortex $V(r) = (1 - e^{-r^2})/r$. Its stability properties were recently investigated in great detail by Fabre, Sipp and Jacquin [31]. In addition to the Kelvin modes, there are slightly damped modes termed “critical layer waves” in [31]. The latter modes include regions centered on a singularity of the Howard-Gupta equation, where viscosity is significant. A model more realistic than the Lamb-Oseen vortex was proposed recently by Fabre and Jacquin [29] who introduced an intermediate layer within which $V(r) \sim r^{-\alpha}$, where the constant α can be chosen to best fit the data. This profile was then used to investigate the cooperative short wave instability involving the interaction of two counter-rotating vortices.

If we consider now the case of shear flows such as jets or wakes with $W \neq 0$ and $V = 0$, the associated linear stability theory is very similar to that for plane, parallel flows. A necessary condition for instability analogous to Rayleigh’s inflection point theorem was derived by him and extended by Batchelor and Gill [7]. A Gaussian axial flow $W(r) = e^{-r^2}$ satisfies Rayleigh’s criterion and this form of W combined with a Lamb-Oseen profile for the azimuthal component is now known as the Batchelor vortex.

Lessen *et al.* [58] adapted Batchelor’s similarity solution for stability investigations, writing it in the dimensionless form

$$V(r) = \frac{q}{r} \left(1 - e^{-r^2}\right) \quad \text{and} \quad W(r) = e^{-r^2}, \quad (2.1)$$

where q is a swirl parameter. It was shown in [58] that the axial flow is stabilized for $q \geq 1.5$, approximately, and this result was seemingly confirmed by a number of subsequent investigations, the most detailed being that of Mayer and Powell [66]. Heaton [41], however, showed that weakly amplified center modes (*i.e.*, modes having a critical point singularity near $r = 0$) exist and these modes are unstable until $q \geq 2.31$. (The sign of $W(r)$ in Batchelor’s solution is actually negative, as discussed in [22], but Lessen *et al.* pointed out that the sign of W has no effect on the temporal growth rate so it can be normalized as in (2.1) for convenience.)

It has been known from flight tests for many years that aircraft trailing vortices contain

strong axial flows [17, 37, 86]. These can be directed towards the airplane (wake-like) or away from it (jet-like). Most often, there is a velocity defect in the vortex core, but many factors enter into determining whether there is a defect or an excess, including angle of attack and wingtip configuration. The analysis of Batchelor [6] demonstrated the dynamical necessity of axial flow relative to the free stream in the core of the vortex. Starting from inviscid considerations, he showed that changes in the azimuthal motion in the downstream direction produce an axial pressure gradient resulting in an acceleration of the axial velocity. In fact, the Bernoulli equation suggests that W , the axial velocity, becomes infinite as $r \rightarrow 0$. (As pointed out by Saffman [77], $W(0)$ is finite in [6] only because Batchelor assumed the interior part of the vortices to be in solid body rotation).

Having shown the importance of an axial flow with an inner viscous core, Batchelor went on to formulate a boundary layer analysis valid far downstream of the wingtip. This led to his similarity solution having the form (2.1) above. Batchelor's point of view in discussing this similarity solution was that viscous diffusion of the vortex would counteract the Bernoulli effect and thereby lead to a deficit in the profile for $W(r)$. There is an additional effect of viscosity contributing towards a wake-like flow and that stems from the boundary layer on the wing. The latter effect was discussed by Batchelor [6] and an expression estimating its effect on $W(r)$ was derived by Moore and Saffman [67].

Whatever the source of the deficit often observed in experiments, it cannot be explained by the far field solution found by Batchelor [6] because of the limited size of any apparatus. This was one of the considerations that motivated Moore and Saffman [67] to modify the approach of [6]; we will describe briefly their solution in Section 2.2. In experiments, both deficits [4, 23] and excesses [19] have been observed for the axial velocity profile. Spalart [81] has explained how to predict which will be the case by introducing a parameter $\Gamma/(W_0 b)$, where Γ is the circulation, W_0 the free-stream velocity and b the wingspan. Small values of this parameter are associated with deficits. Anderson and Lawton [2] have confirmed this behavior in their wind tunnel experiments and they explain that the two behaviors are most correlated with the wing's angle of attack, deficits being associated with smaller angles of

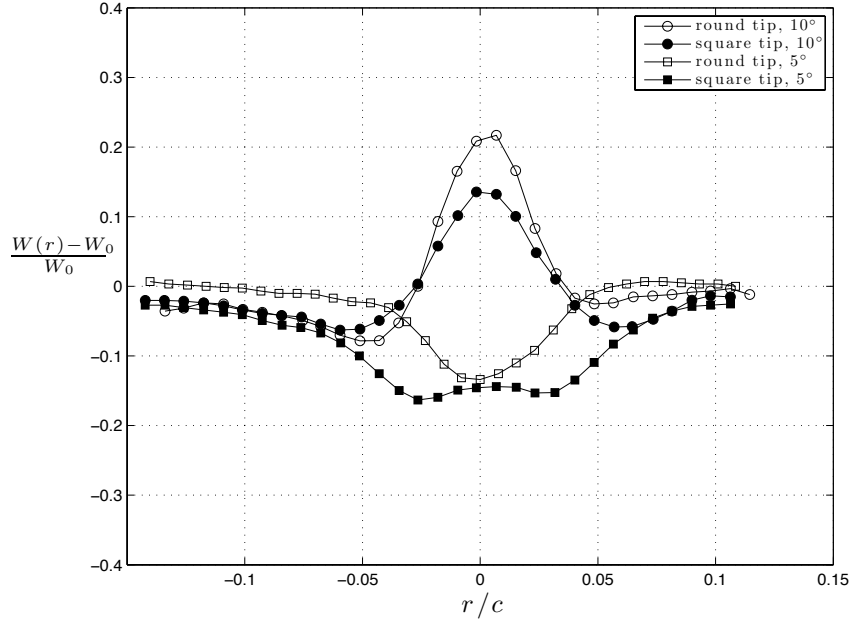


Figure 2.1: Axial velocity profiles from the experiments of Lee and Pereira [56]. The chord $c = 28$ cm and the measurements were made at a distance $x/c = 5$ downstream of the wingtip.

attack. In addition, they observed that the wingtip configuration influenced the magnitude of the axial velocity, rounded tips producing a higher axial velocity at the same value of the circulation parameter.

Given our objective to determine the stability of a trailing vortex, we must have an accurate representation of the velocity profile and the question of velocity deficits is only one aspect. Some of the experimentally measured profiles simply cannot be fit with a Gaussian. The same profile may include, for example, both wake-like and jet-like regions, as illustrated in the experiments in [56]. This can be seen in the axial velocity profiles of Figure 2.1, where we have curve fit data kindly provided to us by Dr. Pereira. Clearly, the profile for the square wingtip at 5° angle of attack cannot be described well by a Gaussian profile. We will see in Section 2.2 that an advantage of the solution presented in [67] is that the magnitude and direction of axial velocity vary according to the value of a parameter related to the wing loading. A careful comparison of the solutions given by [6] and [67] with their measured

velocity and axial vorticity profiles was made by del Pino *et al.* [22]. These researchers found that the presence of the wing loading parameter permitted a greater variety of their velocity profiles to be described accurately by the Moore-Saffman profiles than was the case with the Batchelor vortex.

2.2 Moore-Saffman vortex

We will consider the stability of a columnar vortex in an incompressible and inviscid fluid in Sections 2.3 and 2.4. In cylindrical coordinates (r, θ, z) , the velocity components of such a vortex can be written $[0, V(r), W(r)]$ so that the Howard-Gupta equation governs its stability. As we already noted in Section 2.1, boundary-layer-type solutions that describe aircraft trailing vortices have been given by both Batchelor [6] and Moore and Saffman [67]. Specifically, the assumptions $\partial/\partial z \ll \partial/\partial r$ and $V \ll W$ are employed in both papers. (This is termed the viscous light-loading approximation in [67].) The analysis of Batchelor [6] is steady and includes the additional assumption that far downstream $|W - W_0| \ll W_0$, where W_0 is the speed of the wing at infinity, *i.e.* in a fixed frame. Moore and Saffman [67] employ an equivalent condition specified below. The point of departure between the two analyses is that [67] uses a two-dimensional time dependent formulation to describe the vortex development beginning near the completion of roll-up. This solution is then converted to a steady form by setting $t = z/W_0$. Let us briefly comment on the approximations involved.

The Reynolds numbers associated with trailing vortices are extremely high, even in the laboratory. For example, Olsen [45] states that 10^4 is a typical value of this parameter for his water tunnel experiments compared with 10^7 for flight situations. Although it is true that these Reynolds numbers are large, the necessity of a viscous core is still evident because, as we will see below, the inviscid solution for light loading is singular as $r \rightarrow 0$.

An important simplification employed in both [6] and [67] is that the flow is supposed axisymmetric. Experiments suggest that this assumption is valid even as close to the wing as 3 chord lengths downstream from the tip [23, 39]. Batchelor's similarity solution should

provide an accurate description of the vortex decay sufficiently far downstream of the wing; however, Moore and Saffman [67] estimate that in the case of Olsen’s experiments, this distance would be of the order of several thousand chord lengths. The desire to be able to make comparisons with experiments, those of Olsen being one example, is cited by the authors as a primary motivation for their analysis. We can add, however, that it is perhaps of greater significance that their analysis provides a better description than [6] of the in-flight development of trailing vortices relatively near to the wingtip.

With these objectives in mind, the intermediate region between the beginning of vortex roll-up and the far field, in which the radial distribution of vorticity in the inner-most portion is continuous, was investigated by Moore and Saffman. Noting that the three-dimensional steady problem is intractable, the authors considered instead the axisymmetric, time-dependent evolution of a vortex. For that case, a similarity solution could be obtained. In Appendix A of their paper, they show that the replacement of t by z/W_0 can be formally justified when the angle of attack $\alpha \rightarrow 0$ and z is large. It was also shown there that this is equivalent to the assumption $W \ll W_0$, where W is the departure from the free-stream velocity.

The analysis in Moore and Saffman [67] begins by considering the inviscid roll-up of a wingtip vortex which leads to the conclusion that the azimuthal velocity v_θ has the behavior

$$v_\theta \sim \beta r^{-n}, \quad (2.2)$$

where the wing loading near the tip is proportional to x^{1-n} and x is the spanwise coordinate, $0 \leq x \leq b$. The value $n = 1/2$ corresponds to elliptic loading, Batchelor’s solution is recovered for $n = 1$ and $0 \leq n \leq 1$. The constant β is related to the wing loading, angle of attack and aspect ratio. Its significance and estimates for different distributions of circulation have been reported by Pullin and Phillips [73]. As an illustration of how β can be estimated for a particular case, the reader is referred to the experiments of Baker *et al.* [4], where the results are compared with the similarity solutions in [67].

After making the light loading approximation and using Bernoulli’s equation, substituting

(2.2) into the inviscid equations leads to the following behavior for w and the pressure p :

$$p \sim -\frac{\beta^2}{2n} r^{-2n} \quad \text{and} \quad w \sim \frac{\beta^2}{2W_0} \left(\frac{1}{n} - 1 \right) r^{-2n} \quad \text{as } r \rightarrow 0. \quad (2.3)$$

Given that v_θ, w and p are all singular as $r \rightarrow 0$, it is clear that a viscous core is required to describe the interior of the vortex. The governing equations, derived using boundary layer methods in Moore and Saffman [67], are parabolic and this lends itself to a similarity solution. Employing the notation of [67], the independent variables are time t and a similarity variable $\eta(r, t)$; it is understood that in our application to trailing vortices t is to be replaced by z/W_0 .

What makes the system of three equations governing the viscous core relatively easy to solve is that the coupling is weak. The presentation in Saffman [78] (Ch. 13) begins with the steady equations and shows that the substitution $z = W_0 t$ leads to a single equation for v_θ that was solved by Kirde more than 50 years ago. The solution of this equation can be written

$$v_\theta(r, t) = \frac{\beta}{(\nu t)^{n/2}} V_n(\eta), \quad (2.4)$$

where

$$\eta = -\frac{r^2}{4\nu t} \quad \text{and} \quad V_n(\eta) = 2^{-n} \Gamma\left(\frac{3}{2} - \frac{n}{2}\right) (-\eta)^{\frac{1}{2}} M\left(\frac{1}{2} + \frac{n}{2}, 2, \eta\right). \quad (2.5)$$

$M(a, b, \eta)$ in (2.5) denotes the confluent hypergeometric function and Γ is the gamma function. It should be noted that the presence of the wing loading parameter n in the solution for v_θ is the result of matching the solution of the azimuthal momentum equation to (2.2). The actual boundary conditions imposed on the viscous solution are that as $-\eta \rightarrow \infty$, v_θ, w and p should match with the $r \rightarrow 0$ approximation of the inviscid solution, as given by (2.2) and (2.3).

With v_θ given by (2.4), it is straightforward to solve for the pressure using the radial momentum equation. The result for the η -dependent part of the pressure, in the notation of [67], can be written

$$P_n(\eta) = -\frac{1}{2} \int_{-\infty}^{\eta} \eta^{-1} V_n^2(\eta) d\eta. \quad (2.6)$$

With the pressure now known, one finds from the axial momentum equation that w is given by

$$w(r, t) = \frac{\beta^2}{W_0(\nu t)^n} W_n(\eta), \quad (2.7)$$

where $W_n(\eta)$ satisfies the second order ODE

$$\eta \frac{d^2 W_n}{d\eta^2} + (1 - \eta) \frac{dW_n}{d\eta} - nW_n = -nP_n - \eta \frac{dP_n}{d\eta}. \quad (2.8)$$

Calculation of the mean flow profiles must be done numerically and integrals of confluent hypergeometric functions are involved. We follow the approach of [67] which begins by solving for $P_n(0)$ from Equation (2.6) to obtain

$$P_n(\eta) = P_n(0) - \frac{1}{2} \int_0^\eta \eta^{-1} V_n^2(\eta) d\eta. \quad (2.9)$$

The particular solution $W_I(\eta)$ of (2.8) that satisfies

$$W_I(0) = 0 \quad \text{and} \quad \frac{dW_I}{d\eta}(0) = -nP_n(0) \quad (2.10)$$

can then be found by a single simultaneous integration of (2.8) and (2.9) towards $\eta = \infty$. The general solution $W_n(\eta)$ follows directly from the initial and boundary conditions on w once $W_I(\eta)$ is known.

Recalling that the normalization usually used for the Batchelor vortex is $W(0) = 1$, we must change this because according to the solution of (2.8), $W_n(0) = 0$ at $n \approx 0.44$. We, therefore, scale W by introducing the quantity \bar{W} , defined to be the difference between maximum and minimum axial velocity. We will also divide the swirl parameter q by an additional factor of 2 to ensure that the characteristic velocity used by others for the Batchelor vortex is obtained as $n \rightarrow 1$. The resulting characteristic velocity scale W_s and characteristic length scale r_s are

$$W_s = \bar{W} \frac{\beta^2}{W_0(\nu t)^n} \quad \text{and} \quad r_s = (4\nu t)^{1/2}. \quad (2.11)$$

Starting from (2.4) and (2.7), we then write for the non-dimensionalized mean velocity profiles

$$V(r) = 2qV_n(\eta) \quad \text{and} \quad W(r) = \frac{1}{\bar{W}} W_n(\eta) \quad (2.12)$$

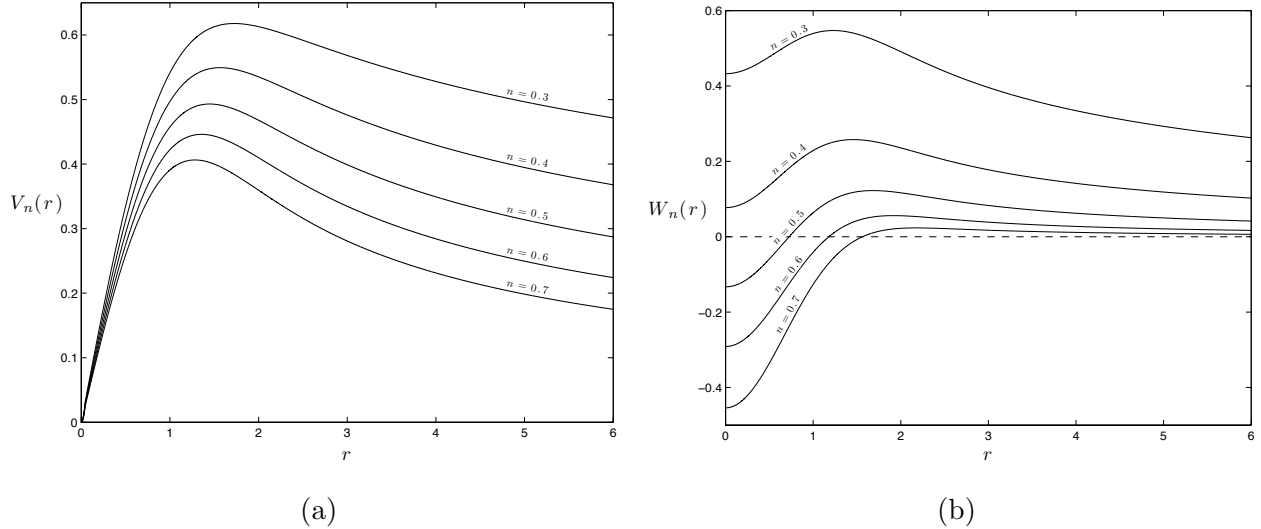


Figure 2.2: Numerical solution of Equation (2.8) giving (a) the tangential velocity profile and (b) the axial velocity profile obtained from the similarity solution of Moore and Saffman [67].

with $\eta = -r^2$ and the swirl parameter given by

$$q = \frac{(\nu t)^{n/2} W_0}{2\beta \bar{W}}. \quad (2.13)$$

In light of the discussion in Section 2.1 about experimental observations of wake-like vs. jet-like axial flows, a particularly interesting aspect of the solutions obtained from the numerical integration of (2.8) is that the character of w changes near $n = 0.44$. For n larger than this value, the vortex has a wake-like core with jet-like velocity only for large r . This is consistent with Batchelor's solution, which is recovered when $n = 1$ and which he described as being wake-like. In Figure 2.2, we show how the azimuthal and axial velocity profiles vary with n . As this parameter decreases, it can be seen that even for $n = 0.7$ the axial velocity profile is not far from Gaussian. However, the magnitude of $W_n(0)$ decreases with n and for $n < 0.44$ the flow relative to the wing becomes jet-like. It can be seen that going from velocity defect to an excess is quite different from simply reversing the sign of e^{-r^2} in (2.1).

From the axial velocity profiles shown in Figure 2.2(b), we can see why a better approximation to the experimental profiles in Figure 2.1 is possible. For the square tipped wing at

5° angle of attack, for example, the solution of Equation (2.8) could be used with $n \approx 0.35$. In the case of the round tipped wing at an angle of attack of 10°, on the other hand, the solution with $n \approx 0.55$ would be appropriate.

2.3 Stability equation and numerical approach

Our objective, as stated in Sections 2.1 and 2.2, is to investigate the stability of a vortex whose velocity components, in cylindrical coordinates, can be written $[0, V(r), W(r)]$. To that end, a helical perturbation of $O(\varepsilon)$ is superimposed on the mean flow and we write for the radial, azimuthal and axial velocity, respectively,

$$[u_r, u_\theta, u_z] = [0, V(r), W(r)] + \varepsilon[i u(r), v(r), w(r)]e^{i(kz+m\theta-\omega t)}. \quad (2.14)$$

The pressure

$$P = \bar{p}(r) + \varepsilon p(r)e^{i(kz+m\theta-\omega t)}, \quad (2.15)$$

where $\bar{p}(r)$ is the pressure of the unperturbed vortex. The axial wavenumber is denoted k , m is the azimuthal wavenumber and $\omega = \omega_r + i\omega_i$ is the complex frequency. Substituting these expressions into the inviscid momentum equations and the continuity equation, and then linearizing, one can eliminate all variables but u to obtain the stability equation found by Howard and Gupta [43], namely,

$$\begin{aligned} \gamma^2 D[SD_\star u] - \left\{ \gamma^2 + \gamma r D \left[S \left(\frac{D\gamma}{r} + \frac{2mV}{r^3} \right) \right] \right. \\ \left. - 2kV \frac{S}{r^2} [krD_\star V - mDW] \right\} u = 0, \end{aligned} \quad (2.16)$$

where $D = d/dr$, $D_\star = d/dr + 1/r$, $S = r^2/(m^2 + k^2r^2)$ and

$$\gamma(r) = mV/r + kW - \omega. \quad (2.17)$$

A detailed derivation of (2.16) can be found in Ash and Khorrami [3].

Since $r = 0$ is a regular singularity of (2.16), boundary conditions at the vortex center can be obtained from a Frobenius expansion. If one imposes the restrictions $V(0) = 0$,

$V''(0) = 0$ and $W'(0) = 0$, which are satisfied by the Moore-Saffman velocity profiles and which are argued in Heaton [41] to be natural for real flows, it is straightforward to derive a second order expansion of the form

$$u(r) = r^\delta(1 + a_1r + a_2r^2 + \dots). \quad (2.18)$$

The solution that is bounded at $r = 0$ has the Frobenius exponent $\delta = |m| - 1$.

The far field boundary conditions are deduced by examining the asymptotic form of (2.16). For the Batchelor vortex, it was found (see [58] and [3]) that the pressure perturbation for large r satisfies the modified Bessel equation and, knowing the asymptotic behavior of p , u can be found easily from the radial momentum equation. For the Moore-Saffman profiles, we find that (2.16) reduces to a similar equation and its asymptotic behavior for large r is given by

$$u(r) \sim \frac{e^{-kr}}{\sqrt{r}} \left(1 + \frac{1}{8} \frac{4m^2 + 3}{kr} + \dots \right), \quad (2.19)$$

where n does not appear until the term involving $1/r^2$.

Two different numerical methods were used to solve (2.16) in this study. The first was a high accuracy shooting method with contour deformation used to deal with singular neutral modes, as in Lessen *et al.* [58]. The viscous critical layer analysis of Le Dizès [54] shows that the correct eigenvalue condition for a neutral mode is obtained by considering the limit $\omega_i \downarrow 0$. For our vortex, this means indenting the integration contour over the singularity, a consequence of γ'_c being negative, where $\gamma(r_c) = 0$ and γ is defined in (2.17).

In addition to the shooting method, we also employed spectral collocation methods using either Chebyshev or rational Chebyshev functions (see Boyd [13]). Because the eigenvalue ω does not appear linearly in (2.16), it is more convenient to combine the governing equations into

$$\gamma \left[ku - \frac{1}{k} D \left(D_\star u + \frac{mv}{r} \right) \right] - \frac{D\gamma}{k} \left(D_\star u + \frac{mv}{r} \right) \quad (2.20)$$

$$+ D(DWu) + \frac{2kVv}{r} = 0, \quad (2.21)$$

and

$$\gamma \left[krv + \frac{m}{k} \left(D_\star u + \frac{mv}{r} \right) \right] + (krD_\star V - mDW)u = 0, \quad (2.22)$$

which is a less reduced form of the Howard-Gupta equation and contains the eigenvalue linearly. The second equation includes a minor correction of equation (5b) in [66].

The boundary conditions at the inner boundary $r = 0$ were derived by Batchelor and Gill [7] and are given by

$$u = v = 0 \quad \text{when} \quad m = 0, |m| > 1, \quad (2.23)$$

and

$$Du = u + mv = 0 \quad \text{when} \quad |m| = 1. \quad (2.24)$$

For the far field boundary condition, one simply imposes $u = v = 0$ as $r \rightarrow \infty$. It is necessary to map the infinite domain to a finite interval to proceed with the numerics. The physical domain $r \in [0, \infty)$ may be either truncated to $[0, R]$ for some large R and mapped to $x \in [-1, 1]$ using the linear transformation

$$x = \frac{2}{R}r - 1, \quad (2.25)$$

or a more involved transform may be used on the semi-infinite interval. For example, the algebraic map

$$x = \frac{r - L}{r + L} \quad (2.26)$$

can be used, where L is a scaling parameter. Both maps have been implemented for our calculations and yield the same result, although convergence for the map (2.26) was generally found to be faster. The range of parameters used was R up to 200, L of order 1 and the number of base functions N up to 250. Detailed discussions of the merits of each method described in this section can be found in both [3] and [41].

2.4 Numerical results

Computations are presented below for unstable disturbances in a range of values of the Moore-Saffman wing loading parameter n and of the swirl parameter q . Only the principal modes of instability are shown. The critical value of q at which stabilization occurs will be

denoted by q_c . The value of q for which the growth rate of the most unstable disturbance is the largest will be denoted by q^* . The mean profiles as $n \rightarrow 1$ correspond to the Batchelor vortex mean flow profiles up to an accuracy of 10^{-3} , which allows us to verify our computational methods. Our results are in close agreement with those reported by Mayer and Powell [66].

2.4.1 Instabilities for $|m| = 1$

Figure 2.3 shows the growth rates of unstable disturbances in the (q, k) -plane for values of $n = 0.70, 0.60, 0.50$ and 0.40 . Only unstable contours and the neutral curve are displayed, with the growth rate being constant along each contour. The outermost solid contour represents $\omega_i = 0.03$ and the dotted contour is the neutral curve. First, compared to Figure 3 of [66] for the Batchelor vortex, the range of unstable values of k and q expands as n is decreased from $n = 1$. This destabilization happens slowly for $n > 0.70$, but becomes more rapid for values of n below that. We find that the region of instability in the (q, k) -plane continues to expand until $n \approx 0.44$. The unstable region shrinks somewhat when n is decreased further, as can be seen from the plot in Figure 2.3(d) for $n = 0.40$. The variation of q_c with n is different from that of the critical value of k when n is decreased: q_c increases significantly until $n \approx 0.44$ and diminishes after that, whereas k_c experiences a slow monotonic increase. Secondly, the growth rates increase when n is decreased. The maximum growth rate for $n = 0.70$ and $n = 0.50$ were found to be $\omega_i = 0.256$ and $\omega_i = 0.275$, which is larger than the value $\omega_i = 0.242$ reported in Mayer and Powell [66] for the Batchelor vortex. Finally, the ridge marking the two-lobed structure of the unstable region becomes more pronounced for lower n . The location of the ridge shifts towards $q \approx 0.40$ and this causes the highest contour lines to split so that, for $n = 0.40$, the surface has developed two separate (flat) peaks. These are located at $q = 0.25, k = 1.03$ and $q = 0.42, k = 0.65$.

Detailed results of the most unstable perturbations for several values of n are presented in Table 2.1. The value of q_c increases from $q_c = 1.53$ for $n = 0.95$ to $q_c = 2.25$ for $n = 0.50$. This means that for the case of elliptic loading of a wing, one can encounter unstable disturbances

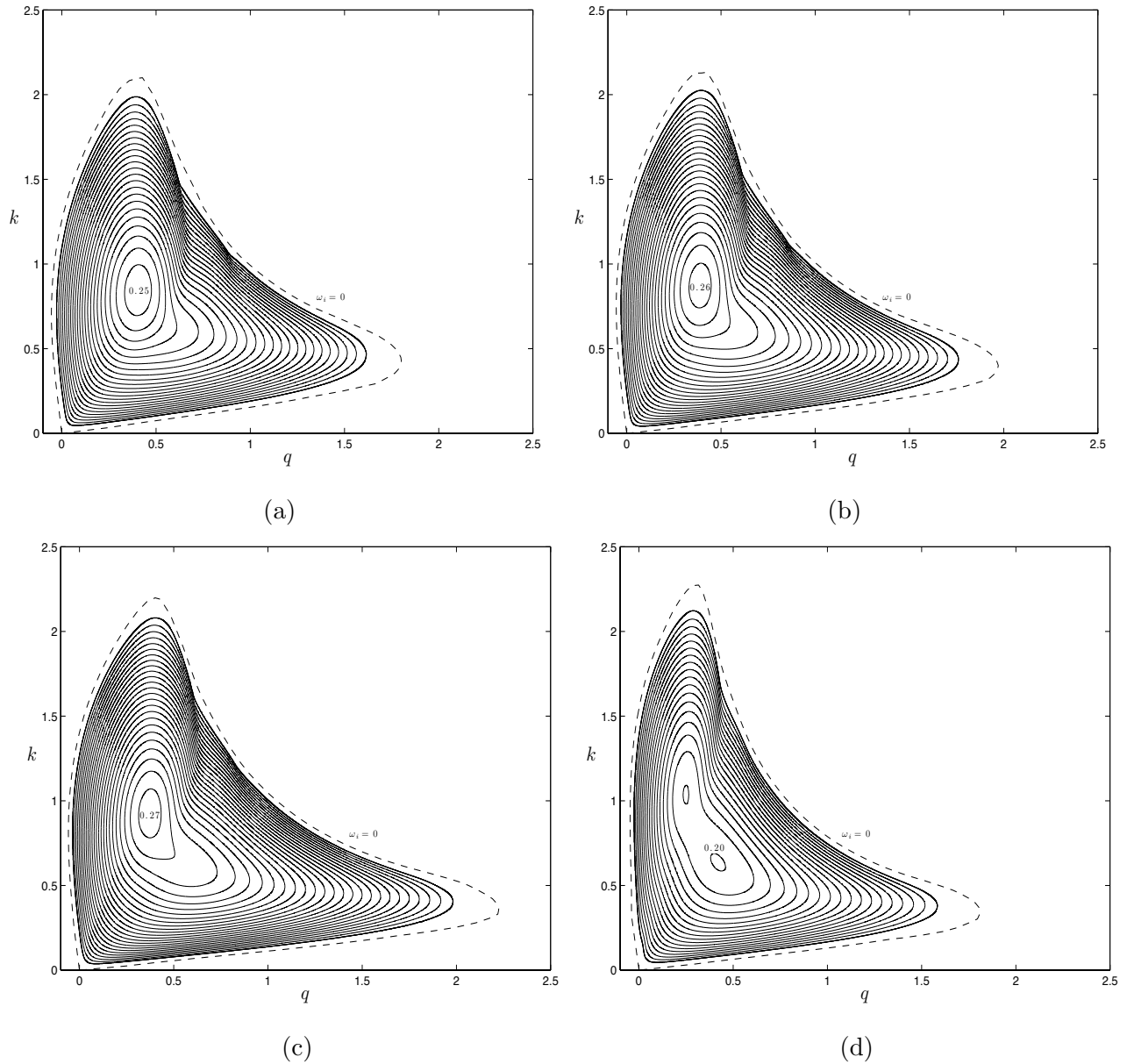


Figure 2.3: Contour plots of the growth rates ω_i of instabilities for all values in the (q, k) -plane for $m = -1$: shown are results for (a) $n = 0.70$, (b) $n = 0.60$, (c) $n = 0.50$ and (d) $n = 0.40$. The spacing between the solid contours is 0.01. The outermost solid contour represents modes with growth rate $\omega_i = 0.03$ and the dotted contour is the neutral curve.

n	q^*	k^*	ω_i	q_c
1.00	0.458	0.811	0.242	1.50
0.95	0.448	0.817	0.244	1.53
0.90	0.439	0.820	0.245	1.58
0.80	0.422	0.829	0.250	1.70
0.70	0.405	0.844	0.256	1.82
0.60	0.390	0.873	0.264	1.99
0.50	0.374	0.929	0.275	2.25
0.44	0.363	0.986	0.282	2.49
0.40	0.249	1.038	0.201	1.83
0.30	0.091	0.812	0.064	0.63

Table 2.1: For $m = -1$ and various values of n , the parameter values and growth rates of the most unstable perturbations identified and the critical value q_c of swirl for which stabilization occurs. The case $n = 1.00$ represents the results found by [66] for the Batchelor vortex.

in a region of parameter space for which the Batchelor vortex is stable. The value of q^* decreases slightly when n is reduced which indicates that the most unstable modes occur at a lower value of swirl. The wavelength k^* of the most unstable disturbance shortens until $n = 0.44$ and quickly lengthens again for lower values of n . The maximum growth rate for the Moore-Saffman profiles increases from $\omega_i = 0.244$ for $q^* = 0.448$ to $\omega_i = 0.275$ for $q^* = 0.374$ when n is decreased from $n = 0.95$ to $n = 0.50$. The largest growth rates were found to be attained for $n \approx 0.44$.

A similar effect takes place for the modes with $m = -1$ and $q < 0$ which, as pointed out by [3], correspond to modes with $m = 1$ described in [58]. The critical swirl value q_c changes very little, although the growth rates do increase. The maximum growth rate of $\omega_i = 0.051$ for $n = 0.95$ increases to $\omega_i = 0.081$ for $n = 0.50$.

Finally, we have computed the most amplified $m = -1$ disturbance for the complete

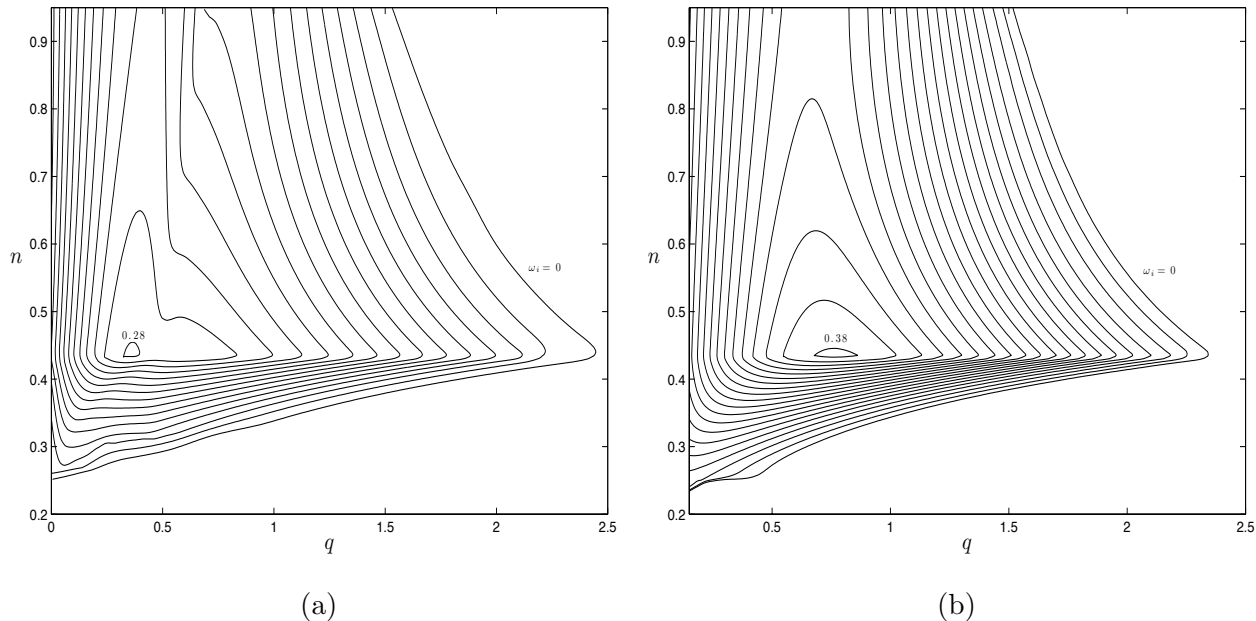


Figure 2.4: The maximum growth rates ω_i for all values in the (q, n) -plane for (a) $m = -1$ and (b) $m = -2$. The outermost contour represents the neutral curve and the spacing between the contours is 0.02.

(q, n) -plane. The results are shown in Figure 2.4(a). Each point on the picture represents the growth rate of the most unstable perturbation for a given value of q and n . For example, the most unstable disturbance for $q = 1.50$ and $n = 0.50$ has a growth rate of about $\omega_i = 0.12$. One can again observe the three main changes we have found to be associated with a decrease in n : an increase of the critical value q^* , an increase in growth rates and a shift of the ridge in the unstable region towards lower values of q . No unstable disturbances were found for values of the Moore-Saffman parameter below $n \approx 0.25$.

A sufficient condition for the instability of columnar vortices has been derived by Leibovich and Stewartson [57] and we have verified that our results for unstable perturbations are consistent with that condition. It was shown in [57] that the flow is unstable if

$$VD(\Omega)[(D(rV)D(\Omega) + (DW)^2)] < 0, \quad (2.27)$$

where $\Omega = V/r$ and D indicates differentiation with respect to r . For the Batchelor vortex (2.1), condition (2.27) yields the sufficient condition $q < \sqrt{2}$ which is close to the marginal

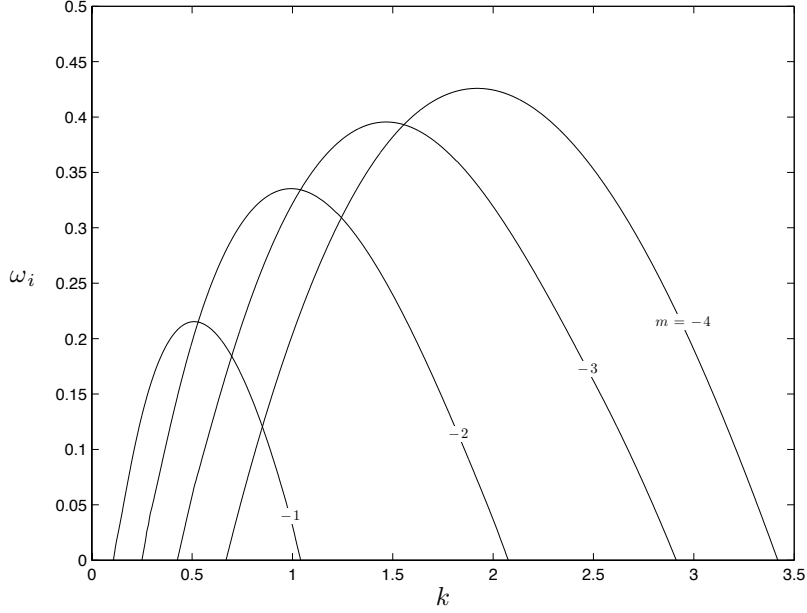


Figure 2.5: The variation of ω_i with k for $q = 1$ and $n = 0.50$ for several azimuthal wave numbers ($m = -1, -2, -3$ and -4).

stability value of 1.50 if center modes are excluded. As n is decreased, we found that the condition (2.27) is less sharp, but still reasonably close to our computed values. For example, with $m = -1$ and $n = 0.5$, it can be seen from Table 2.1 that $q = 2.25$ at marginal stability. This is consistent with the sufficient condition for instability $q < 1.664$ given by (2.27), *i.e.* the vortex is indeed unstable for q less than 1.664.

2.4.2 Instabilities for higher azimuthal wave numbers $|m| > 1$

A comparison of growth rates for the particular case $q = 1$ and $n = 0.5$ is presented in Figure 2.5. We see that, as in the case of the Batchelor vortex [58, 66], the modes become progressively more unstable with increasing $|m|$. Table 2.2 presents results for the location and growth rate of the most unstable mode for azimuthal wave numbers $m = -2, -3$ and -4 . As suggested by the results in this table, the increase in ω_i with increasing $|m|$, shown in Figure 2.5 for $n = 0.5$, is observed for all the values of n that we have considered. It should also be noted that the growth rates of the most amplified disturbance increase when

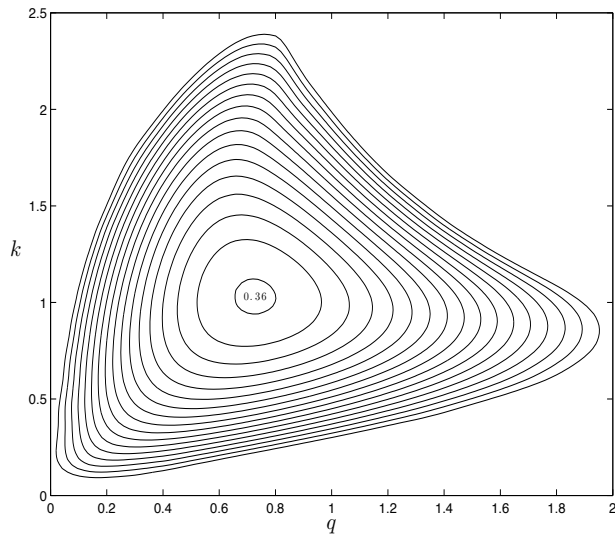
	$m = -2$			$m = -3$			$m = -4$		
n	q^*	k^*	ω_i	q^*	k^*	ω_i	q^*	k^*	ω_i
1.00	0.693	1.182	0.314	0.779	1.665	0.355	0.815	2.176	0.378
0.95	0.683	1.169	0.314	0.770	1.641	0.355	0.807	2.140	0.378
0.70	0.670	1.095	0.329	0.761	1.520	0.373	0.800	1.973	0.397
0.60	0.689	1.061	0.342	0.778	1.471	0.388	0.817	1.904	0.414
0.50	0.726	1.029	0.363	0.817	1.422	0.412	0.856	1.837	0.439
0.44	0.762	1.010	0.381	0.854	1.394	0.432	0.898	1.800	0.461
0.40	0.558	0.997	0.277	0.623	1.374	0.314	0.655	1.771	0.335
0.30	0.196	0.966	0.094	0.220	1.328	0.106	0.229	1.704	0.113

Table 2.2: A comparison of the results for the most unstable modes identified, for various values of n , for azimuthal wave numbers $m = -2, -3$ and -4 . The case $n = 1.00$ shows results found by [66] for the Batchelor vortex.

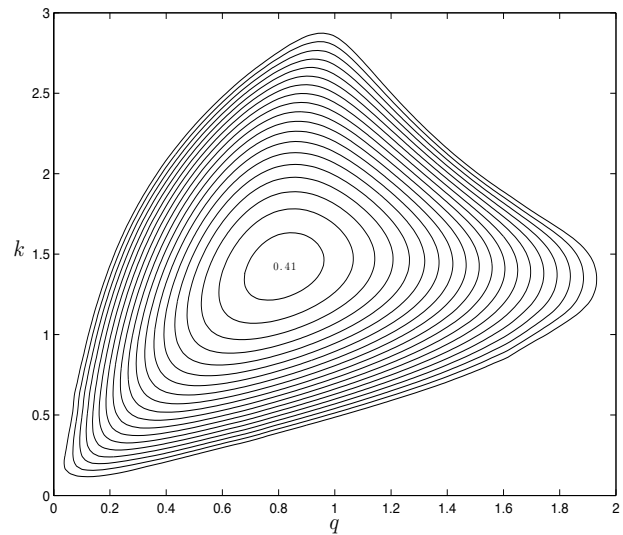
n decreases. The maximum amplification occurs at a higher value q^* of the swirl parameter, while the value of k^* is seen to decrease only slightly. The vortex begins to stabilize when n is decreased below $n = 0.44$ and all wavelengths become damped below $n \approx 0.25$.

The unstable regions for $m = -2, -3$ and -4 for the case of elliptic wing loading are shown in Figure 2.6. The unstable regions were found to be smooth and to contain no ridges. No unstable disturbances were found for $q < 0$. It can be seen that the critical value of k remains fairly constant, while the unstable region expands in the k direction. Figure 2.4(b) displays the growth rates of the most unstable modes for $m = -2$ for the (q, n) -plane. The destabilizing effect of n is similar to that for $m = -1$. However, no ridge is present for $|m| > 1$ so that the surface is smooth. We calculated that the most unstable mean flow profile is $n = 0.44$ with a maximum of $\omega_i = 0.381$ at $q^* = 0.762$.

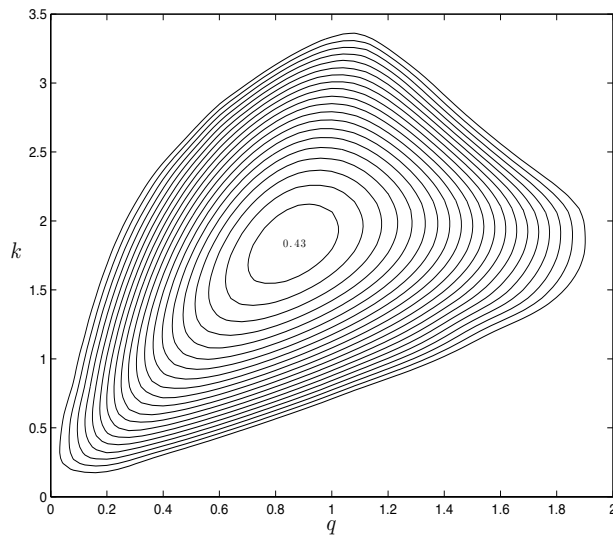
Our results for the Moore-Saffman profiles show a significant difference compared with the Batchelor vortex when the wing loading parameter is decreased towards the value $n = 0.5$,



(a)



(b)



(c)

Figure 2.6: Contour plots of the growth rates ω_i of instabilities for all values in the (q, k) -plane for $n = 0.50$: shown are (a) $m = -2$, (b) $m = -3$ and (c) $m = -4$. The spacing between the contours is 0.02. The outermost contour represents modes with constant growth rate $\omega_i = 0.04$.

corresponding to elliptical wing loading. Below the value $n = 0.44$, where the largest growth rate occurs, the axial velocity profile $W(r)$ no longer has a deficit and it becomes jet-like. For $1 \geq n \geq 0.44$, as noted above, our computations show that the maximum growth rates increase with $|m|$, and they become progressively larger as n is decreased below 1.0. For $-m \geq 2$, they are approximately 22 % greater than those for the Batchelor vortex.

Having computed the amplification factors for many cases, one can ask to what extent the qualitative behavior as n is varied could have been anticipated from the velocity profiles shown in Figure 2.2. First, we should note that the azimuthal profiles $V(r)$ are all stable, so it is the shear of the axial velocity $W'(r)$ that is responsible for the instability. For a jet-like axial flow, it is sometimes true that a larger value of W' will lead to a larger growth rate. To assume, however, that this is true in general will lead to incorrect conclusions. Some insight as to why this is the case follows from the upper bound on ω_i given by Equation (22) of Howard and Gupta [43]. There, it can be seen that the magnitude of the instability involves a competition among several terms and the values of the wavenumbers k and m play a role. Without solving the eigenvalue problem to determine the wavenumber k for a given q and m , it is not generally possible to estimate ω_i .

2.4.3 Axisymmetric instabilities ($m = 0$)

We have searched for axisymmetric modes of instability without finding any for values of n in the range $0.15 \leq n \leq 0.95$. This is consistent with studies of the Batchelor vortex [58, 66], where no such modes were found. The sufficient condition for stability from [7] can be applied to the jet that results when $q = 0$. However, unlike the case of the Batchelor vortex, this condition does not guarantee stability for the Moore-Saffman mean flow profiles since $Q'(r)$ changes sign at a value of $1 < r < 2$, where $Q \equiv rW'/(m^2 + k^2r^2)$. As a consequence, one cannot rule out the existence of unstable axisymmetric disturbances. In addition, we find that the criterion found by Howard and Gupta [43], analogous to the Richardson number 1/4 theorem, does not exclude the possibility of instability. Similar to [58], however, we may argue in a heuristic way that, since the role of stable swirl is purely stabilizing for

axisymmetric disturbances, it is plausible that the Moore-Saffman mean flow profiles are stable to axisymmetric modes.

Although no inviscid linear instability was found for $m = 0$, these modes can still play a role in the elliptic instability. The latter instability can be interpreted as a parametric resonance involving two Kelvin waves with the same values of axial wavenumber and frequency and with azimuthal wavenumbers m and $m + 2$. For a strained Rankine vortex, it is known that the conditions most favorable for instability are $\omega = 0$ and $m = \pm 1$. However, the addition of a continuous axial flow may change this, as was shown by Lacaze, Ryan and Le Dizès [50]. For a strained Batchelor vortex, progressively increasing the axial flow resulted in the combination $m = -2$ and $m = 0$ becoming the most unstable.

2.5 Concluding Remarks

In Section 2.4, we presented the results of stability computations for trailing vortex profiles described by the similarity solution of Moore and Saffman [67]. Their solution contains a wing loading parameter n and we found that there is instability for $n \geq 0.25$. Comparisons, to a certain extent, can be made with results for the Batchelor vortex, which is recovered as $n \rightarrow 1$. For that case, a number of researchers have determined the variation of amplification rates with axial and azimuthal wave number and the swirl parameter q . The latter is important in determining the stability of the vortex because, as we noted in Section 2.1, there is a critical value of q above which the flow is stable. For the Moore-Saffman vortex this value was shown in Section 2.4 to be more than 60% larger than that for the Batchelor vortex.

As the parameter n is decreased from 1.0, the growth rates increase and there is a significant difference compared with the Batchelor vortex once the value $n = 0.5$, corresponding to elliptical wing loading, is reached. The most unstable perturbations occur near $n = 0.44$; below this value, $W(r)$, the axial velocity profile, no longer has a deficit and it becomes jet-like. For $1 \geq n \geq 0.44$, our computations show the same trend with increasing azimuthal wavenumber as that observed in the case of the Batchelor vortex. The maximum growth

rates increase with $|m|$, and they become progressively larger as n is decreased below 1.0. For $-m \geq 2$, they are approximately 22 % greater than those for the Batchelor vortex. Our computations, however, are inviscid and it is well known that the stabilizing effect of viscosity is most effective for short waves. As $|m|$ increases, so does the value of k for the most amplified wave, *i.e.* the wavelength of the fastest growing wave decreases rapidly with increasing $|m|$. At finite Reynolds numbers, the most amplified mode in any given experiment could, therefore, be $m = -2$ or $m = -1$, although shorter waves may also be present, depending on the Reynolds number.

The most striking difference between our results and those for the Batchelor vortex occurs for decreasing n when this parameter becomes less than 0.44, at which point the axial flow changes from wake-like to jet-like. In Section 2.4, we saw that for $n < 0.44$ the amplification factor for the Moore-Saffman vortex decreases rapidly as n becomes smaller and that the vortex is stable for $n \leq 0.25$, approximately. For the Batchelor vortex, on the other hand, it was pointed out in [58] that there is a certain symmetry; changing the sign of $W(r)$ in (2.1) simply reverses the sign of the frequency, but does not affect ω_i , the growth rate. We may conclude that for the purpose of stability investigation, the Batchelor vortex is a more reliable model in the wake-like case, *i.e.* when there is a deficit in the axial flow. Growth rates for the jet-like axial flow, on the other hand, may be too large.

The $m = -1$ mode, sometimes termed the bending mode, deserves special consideration because it is the only mode whose radial perturbation velocity does not vanish at the vortex center. Lessen *et al.* [58] investigated the characteristics of this mode quite thoroughly for the Batchelor vortex, but Mayer and Powell [66] showed that the largest ω_i for this case occurred in a region of parameter space that had been omitted in [58]. (We note, in passing, that the growth rates in Figure 3(a) of [58] must be incorrect, because they are larger than what is stated in their Table 1 to be the maximum value of ω_i). Another reason to examine the bending mode in detail is that in the absence of axial velocity it is the most important for the short wave cooperative instability. Finally, it was shown in [66] that the $m = -1$ mode has the lowest critical Reynolds number and that is likely to be the case for

the Moore-Saffman vortex, as well.

Experimental observations of weakly nonlinear waves on vortices that can be approximated by the Batchelor vortex have been reported by Maxworthy, Hopfinger and Redekopp [65], but their study focused more on long wave propagation than stability. Given the absence of experimental data on hydrodynamic stability of wingtip vortices, the in-flight observations of Brown [15] are particularly interesting. These data were taken at high altitudes (31000 - 38000 ft) and, although the Reynolds numbers were large, atmospheric conditions were laminar or only weakly turbulent. The 9 aircraft generating the wakes were comprised of a considerable variety of jumbo jets, including the A-380. Measurements were primarily of the azimuthal velocity with attention focused on the velocity profiles and the variation of the Rayleigh discriminant. Values of the latter quantity indicated the possibility of centrifugal instability. Without knowing more details of the axial velocity profiles, interpretation of the observations is, of course, somewhat speculative. We mention here only a few results, namely, those most pertinent to the present study and its possible extensions.

First, a number of the azimuthal velocity profiles were found to be described well by the Fabre-Jacquin model [29] which is essentially an approximation of the Moore-Saffman solution with $W = 0$. Secondly, centrifugal instability was indicated according to the Rayleigh criterion and by the measurements. The biggest departure from theoretical models employed here and in earlier stability investigations was the magnitude and behavior of the radial velocity which was larger than one would expect. This raises questions about the parallel flow approximation suggesting that it may be worthwhile to take into account nonparallel effects using multiple scaling. Both inflows and outflows were observed, possibly indicating that the higher modes reported by Duck and Foster [25] and Mayer and Powell [66] may be significant.

The results of our stability analysis suggest that a worthwhile extension would be to employ the Moore-Saffman model in a numerical simulation of the evolution of a pair of counter-rotating vortices. We mention here two studies along these lines using other velocity profiles. First, Faddy and Pullin [32] considered an array of counter-rotating vortices to which

was superposed an axial flow proportional to the axial vorticity. An initial linear instability was noted comprised of helical disturbances. These unstable disturbances equilibrated as the mean axial velocity adjusted and further downstream an elliptic instability was observed.

A second numerical investigation of elliptical instability, including an axial flow, was cited in Section 2.4, namely, the one reported by Lacaze, Ryan and Le Dizès [50]. Unlike [32], the axial flow in [50] was taken to be small so that linear instability could not occur. With no axial flow, the dominant modes in the elliptic instability were found by Fabre and Jacquin [29], using an approximate representation of the Moore-Saffman azimuthal velocity profile, to be $m = \pm 1$. With the addition of an axial flow, it was found in [50] that the combination $m = -2$ and $m = 0$ at some point became the most unstable. It would be interesting to not only employ the Moore-Saffman velocity profiles, but to allow for linear instability, as was done in the investigation of Faddy and Pullin [32].

Part 3

**Elliptical Instability of the
Moore-Saffman Model for a Trailing
Wingtip Vortex**

The elliptical instability exhibited by two counter-rotating trailing vortices is considered. This type of vortex instability can be viewed as a resonance between two normal modes of a vortex and an external strain field. Recently, numerical investigations have extended earlier results that ignored axial flow to include models with a simple axial jet such as the similarity solution found by Batchelor [6]. In this part, we present growth rates of elliptical instability for a family of velocity profiles found by Moore and Saffman [67]. These profiles have a parameter that depends on the wing loading, and are therefore capable of modelling both the jet-like and wake-like axial flow present in a trailing vortex at short and intermediate distances behind the wingtip. A direct numerical simulation is performed using an efficient spectral method in cylindrical coordinates developed by Matsushima and Marcus [64]. We compare our results to those for the Batchelor vortex model. This part is based on a manuscript that was submitted to a peer-reviewed journal in April 2015.

3.1 Introduction

The elliptical instability of a vortex pair has received considerable attention in recent years. In particular, the short-wavelength cooperative instability exhibited by two counter-rotating vortices has been of interest. Most investigations have assumed a vortex model with no axial flow or a simple axial flow profile. We, instead, consider the elliptical instability for a family of similarity solutions found by Moore and Saffman [67]. These velocity profiles are able to model the jet-like and wake-like axial flow present in a trailing vortex.

The short-wave cooperative instability mechanism, which can cause linear instability in a vortex subject to external strain, was first predicted by Widnall, Bliss and Tsai [87] for vortex rings. Shortly thereafter, Moore and Saffman [68] performed a rigorous mathematical analysis of the stability of an infinite straight vortex deformed elliptically by a weak irrotational strain field. They recognized the role of resonance in the instability process: for the case of a general axisymmetric flow, but in the absence of axial flow, they showed that two Kelvin modes can become tuned with the non-axisymmetric correction caused by the strain

field. Moreover, using a multi-scale analysis in the small strain limit, Moore and Saffman obtained estimates of the growth rate of the instability. The aforementioned authors noted that the effect of axial flow is to break the symmetry between oppositely propagating waves of the unperturbed vortex. As a consequence, the presence of an axial flow complicated the problem in such a way that their analysis could only be applied in the case of a small axial flow with a magnitude of the same order as that of the strain field. Results similar to Moore and Saffman's were reported almost concurrently by Tsai and Widnall [84] for the special case of a Rankine vortex.

Several years later, the short-wavelength instability was investigated again by Pierrehumbert [72], albeit in the more general framework of three-dimensional instability of two-dimensional flows. He showed that the instability occurs in a generic quadratic flow modelling the elliptically deformed rigidly rotating core of a general two-dimensional strained flow. Accordingly, the short-wave instability mechanism can be viewed more broadly to be an elliptical instability. Additionally, Pierrehumbert discovered that, in the short axial wavelength limit, the modal structure of the instability becomes increasingly trapped near the vortex center while the growth rate approaches a constant value. This means that there is no short-wavelength cutoff in the absence of viscosity. In contrast, Landman and Saffman [51] determined that such a cutoff does exist in the case of a viscous flow, bounding from above the axial wavenumbers for which instability can persist. Solving a matrix Floquet problem, Bayly [8] obtained close agreement with the results of Pierrehumbert. Waleffe [85] later took a third approach to the same problem. He showed that the stability of the flow is governed by a second order ODE known as the Ince equation, and succeeded in finding an analytical form of the modes found by Pierrehumbert and Bayly. None of the studies mentioned includes axial flow, since it makes an analytical approach largely intractable. As a consequence, most analytical investigations in the last twenty years have made restrictive assumptions, such as a specific swirl flow profile $V(r)$ and an absence of axial flow. Several of these investigations are discussed below. A review of recent progress that has been made in elliptical instability research can be found in Kerswell [47].

The vortical flows of interest include an axial mean flow $W(r)$, as well as a swirl component $V(r)$. The Rankine vortex is the simplest model for the swirl component. It is given by

$$V(r) = \begin{cases} \Omega r, & \text{if } r < a, \\ \Omega a^2/r, & \text{if } r > a, \end{cases} \quad (3.1)$$

where a is the vortex core radius and Ω is the solid body rotation rate in the core. The modal solutions corresponding to that profile are termed Kelvin waves. A detailed analysis of the elliptical instability of the Rankine vortex in a multipolar strain field is presented by Eloy [26] and Eloy and Le Dizès [28]. For a similar problem, the Rankine vortex in a dipolar strain field without viscosity, Fukumoto [36] obtained an explicit solution for the disturbance flow field using Bessel and modified Bessel functions, thus allowing for an in-depth analysis of the instability. A more realistic representation of a vortex, because its vorticity is continuous, is provided by the Lamb-Oseen vortex which has azimuthal velocity $V(r) = (1 - e^{-r^2})/r$. Le Dizès and Laporte [55] considered the stability of a pair of Lamb-Oseen vortices, comparing estimates from the theory by Moore and Saffman with direct numerical results. The most unstable elliptical modes were found to be a combination of $m = -1$ and $m = 1$ modes. We note that the study of the elliptical instability for the Rankine vortex and the Lamb-Oseen vortex yields very different results. For example, Sipp and Jacquin [80] point out that, contrary to the case of a Rankine vortex, the presence of critical layers in a Lamb-Oseen vortex prevents a large number of possible resonances. Resonant coupling between Kelvin modes with azimuthal wavenumbers $m = -2$ and $m = 0$ occurs for the Rankine vortex, while the corresponding interaction is damped for the Lamb-Oseen vortex.

More recently, there has been a great deal of interest in understanding the role of elliptical instability in trailing wingtip vortices. A model more realistic than the Lamb-Oseen vortex was proposed by Fabre and Jacquin [29] who presented a two-scale model for the swirl flow $V(r)$, effectively introducing an extra parameter α to better fit trailing vortex data. It has, however, been known from flight tests for many years that aircraft trailing vortices sometimes contain strong axial flows (see e.g. Chow, Zilliac and Bradshaw [19]). As shown

by Lacaze, Birbaud and Le Dizès [49], adding a constant axial jet to the core of the Rankine vortex has a considerable influence on the combinations of Kelvin modes partaking in the resonance process. One of the few studies to consider a trailing vortex model with an axial flow is Lacaze, Ryan and Le Dizès [50], which concerns the elliptical instability of the Batchelor vortex. These authors performed a systematic study of the elliptical modes of instability of a pair of counter-rotating Batchelor vortices, whose axial flow $W(r) = W_0 e^{-r^2}$ with $0 < W_0 < 0.66$. In contrast to the Lamb-Oseen vortex ($W_0 = 0$), the combination of $m = -1$ and $m = 1$ Kelvin modes becomes damped for a slight axial flow. Other resonant pairs become successively unstable and stable as the axial flow is increased further. The stability of a pair of co-rotating Batchelor vortices was subsequently studied by Roy *et al.* [76]. Three years later, the findings for co- and counter-rotating Batchelor vortices were compared to measurements made using particle image velocimetry in a water tank (Roy *et al.* [75]). The experiment revealed a short-wave instability with a spatial structure characterized by the $m = 0$ and $|m| = 2$ azimuthal Fourier modes.

Despite the fact that it is now recognized that the presence of axial flow has a noticeable effect on the elliptical instability, there have been few previous investigations that account for the diversity of axial flow that can be present in trailing vortices. We now review several elements from the introduction of Feys and Maslowe [34]. The relative axial velocity in a trailing vortex can be directed towards the airplane (wake-like) or away from it (jet-like). Although the latter may seem unexpected, Spalart [81] offers two mathematical explanations for jet-like flow: using either the shape of the vortex lines or the Bernoulli equation and the pressure (an argument already given by Batchelor [6]). He also points out that the axial flow can be not only wake-like or jet-like, but it can switch sign within the same flow. The far field solution found by Batchelor does not account for this range of possibilities. In addition, the effect of vortex wandering on experimental observations must be recognized (Baker *et al.* [4]). Devenport *et al.* [23] explain that the velocity field of any vortex will appear as a Batchelor vortex given sufficient wandering. Motivated by the ability of the family of similarity solutions found by Moore and Saffman [67] to account for both wake-

and jet-like flows, our objective is to use these mean flow profiles for an analysis of the elliptical instability of a trailing vortex. It is pointed out by del Pino *et al.* [22] that the presence of an extra parameter (the wing loading parameter n) allows for a greater variety of velocity profiles to be accurately fitted by the Moore-Saffman profiles than is the case with the Batchelor vortex. So far, only the linear inviscid stability for the Moore-Saffman profiles has been studied [34], yielding growth rates that are somewhat larger than those obtained for the Batchelor vortex. The instability is found to persist for larger values of the swirl. The largest amplification rates were found to occur at $n = 0.44$. For $n < 0.44$, the flow in the vortex core is jet-like and the growth rates of unstable perturbations become progressively smaller. An important question addressed in the present work is if the same behavior persists for the elliptical modes of instability.

The goal of this study is to investigate the elliptical instability for the base flow velocity profiles found by Moore and Saffman [67]. The magnitude of the axial flow will be chosen sufficiently small to prevent strong amplification of linear inviscid perturbations acting on the base flow; slight instability will be permitted as it does not interfere with our objectives of examining the cooperative instability. In addition, we will present one instance where the strength of the axial flow is diminished to such an extent that it ensures complete stability of the base flow. We do not exclude the presence of viscous modes (Khorrami [48]) and center modes (Heaton [41]), which, in principle, persist for lower amounts of axial flow, since they are not expected to have an influence on the elliptical instability mechanism. After imposing a weak strain field on the base mean flow, its streamlines relax to an elliptically deformed equilibrium state (Jiménez, Moffatt and Vasco [44]). For our purposes, an expression for the first order non-axisymmetric correction to the base flow given by Moore and Saffman [68] will suffice. The resulting elliptical mean flow will then be used to perform a direct simulation in cylindrical coordinates, employing a numerical method described by Matsushima and Marcus [64]. We will extensively compare the resulting growth rates and vorticity contours with the results for the Batchelor vortex obtained by Lacaze, Ryan and Le Dizès [50]. In addition, we will relate our findings to those of Roy *et al.* [76]. Finally, the effect of the wing loading

parameter n on the Moore-Saffman profiles will be thoroughly investigated.

Part 3 of this dissertation is organized as follows. In Section 3.2, the Moore-Saffman profiles are introduced. We emphasize the physical effect of the wing loading parameter n on the axial velocity component and then summarize the linear inviscid stability results for the Moore-Saffman base flow profiles in order to determine the flow parameters which will be used in the numerical simulation. The range of flow parameters is restricted to make sure that the vortex is mostly stable in the absence of strain and will allow us to attribute modal growth in our numerical investigation to cooperative instability. In Section 3.3, we discuss the non-axisymmetric correction caused by the strain field on the base flow and we derive the governing equation for a perturbation in the presence of viscosity. Further, the details of the numerical procedure are given in this section. We verify the numerical method by comparing its output to a multitude of published results. Section 3.4 contains the findings of our numerical investigation of the stability of a Moore-Saffman vortex subject to a dipolar strain field. Instability growth rates and vorticity contours are presented and compared to the results for the Batchelor vortex. The effect of a change of wing loading parameter n , axial wavenumber k and axial flow parameter W_0 on the resonant pairs is of particular concern. The parameter n is shown to have a major impact on the growth rates. The last section (Section 3.5) consists of concluding remarks.

3.2 Stability characteristics of the Moore-Saffman vortex

In this section, the family of similarity solutions of the Navier-Stokes equations found by Moore and Saffman [67] is discussed briefly. We then summarize its stability characteristics with the aim, in Section 3.4, of constraining the flow parameters to ensure that the vortex does not have strongly amplified modes of instability in the absence of strain. The stability threshold $W_{0,c}$ is of particular interest.

3.2.1 Basic formulation

Consider a columnar vortex with velocity components $[0, V(r), W(r)]$ in cylindrical coordinates (r, θ, z) in an incompressible and inviscid fluid. The assumption of axisymmetry of this base flow is reasonable since it describes the mean flow in the absence of strain and, thus, without non-axisymmetric effects.

Moore and Saffman [67] begin by considering the inviscid roll-up of a wingtip vortex. Because the loading of the wing is an important unknown, a wing loading parameter n is introduced with $n = 1/2$ corresponding to elliptical loading, $0 < n < 1$. In the limit where $n \rightarrow 1$, Batchelor's solution is recovered. After making the light loading approximation, the solutions of the inviscid governing equations are shown to be singular near the vortex core. This necessitates including viscosity to describe the interior of the vortex. Using boundary layer methods, Moore and Saffman then derived parabolic governing equations and obtained a solution using a similarity variable $\eta = -r^2/(4\nu t)$, where ν denotes kinematic viscosity and t is time. The resulting family of similarity solutions consists of velocity components proportional to an azimuthal function $V_n(\eta)$ and an axial function $W_n(\eta)$. The exact expressions for these velocity components involve confluent hypergeometric functions. Moreover, the axial component $W_n(\eta)$ is found to be the solution to a second order ODE that must be solved numerically. Feys and Maslowe [34] provide definitions of the functions $V_n(\eta)$ and $W_n(\eta)$ that were just introduced. Here, we limit ourselves to displaying the velocity components graphically.

The functions $V_n(r)$ and $W_n(r)$ are shown in Figure 3.1, with the similarity variable having been reduced to $\eta = -r^2$. A particularly interesting aspect of the Moore-Saffman profiles is that the character of the axial component $W_n(r)$ changes near $n = 0.44$. For n larger than this value, the vortex has a wake-like core with jet-like velocity only for large r . This is consistent with Batchelor's solution, which is recovered for $n \rightarrow 1$ (but corresponds to an unrealistic, rectangular lift distribution) and which he described as being wake-like. As n decreases, it can be seen that even for $n = 0.7$ the axial velocity profile is not far from Gaussian. However, the magnitude of $W_n(0)$ decreases with n and for $n \lesssim 0.44$ the flow

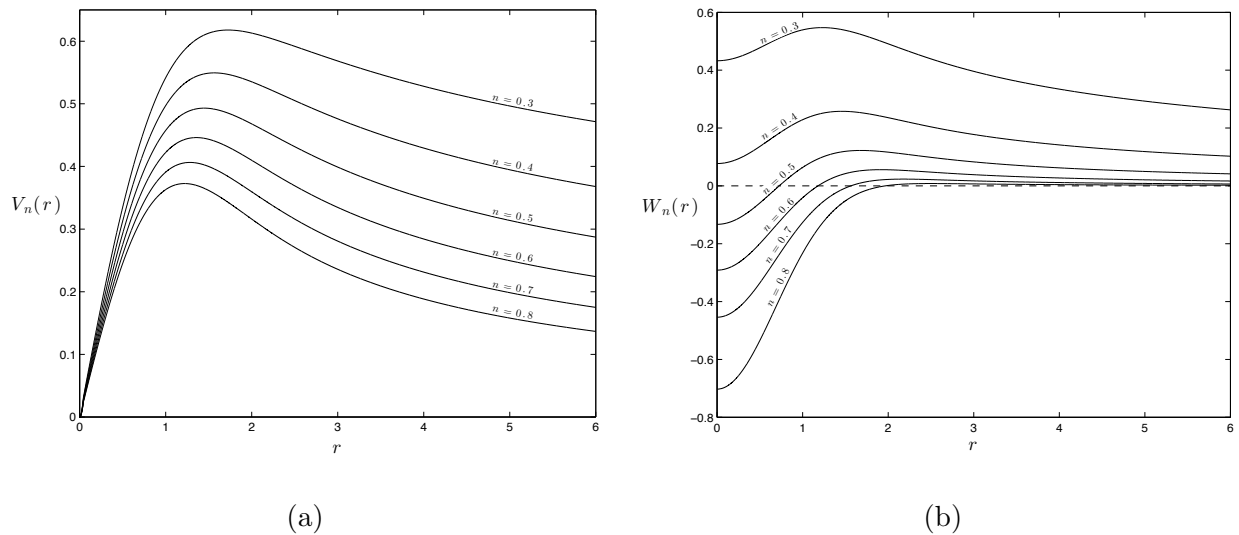


Figure 3.1: Numerical solution giving (a) the tangential velocity profile $V_n(r)$ and (b) the axial velocity profile $W_n(r)$ obtained from the similarity solution of Moore and Saffman [67].

relative to the wing becomes jet-like. Since experimental observations at close proximity to the wingtip have revealed both axial flow deficits and excesses, the wing loading parameter n makes the Moore-Saffman family of profiles well suited to model the variety of axial flow present. Many factors influence the value of n in practice because the wake- or jet-like characteristics of the vortex depend on the angle of attack and the tip configuration of the wing (see Chow, Zilliac and Bradshaw [19] and Anderson and Lawton [2]). A high angle of attack or a round wingtip generally leads to an axial velocity excess at the vortex core (jet-like flow) which corresponds to a low value of n .

In order to be useful in a numerical investigation, a careful non-dimensionalization of these theoretical profiles must be performed. We have chosen to introduce an axial flow parameter W_0 , thereby normalizing the swirl velocity. This contrasts with the more common convention where the magnitude of the axial velocity is normalized and a swirl parameter q is introduced. An extra factor of 2 is put in to ensure that the characteristic velocity used for the Batchelor vortex is recovered for $n \rightarrow 1$. The following base mean flow profiles are

then used in the numerics:

$$V(r) = 2V_n(\eta) \quad \text{and} \quad W(r) = \frac{W_0}{\bar{W}} W_n(\eta) \quad (3.2)$$

with $\eta = -r^2$, the similarity variable, and \bar{W} being the difference between the maximum and minimum value of W_n . In later sections, we will refer to previous investigations that utilized the swirl parameter q instead of the axial flow parameter W_0 . We now specify the relation between q and W_0 . The axial component $W(r)$ is often viewed as having a destabilizing effect on a stable vortex $V(r)$ in an unbounded domain. One thus expects the flow to be stable for $W_0 < W_{0,c}$, where $W_{0,c}$ is a critical value of the axial flow parameter. Keeping in mind the change of convention concerning normalization, the stabilizing value q_c of the swirl parameter found in earlier studies [58, 66] and the value of $W_{0,c}$ used here are related through $W_{0,c} = 1/q_c$. In the case of the Batchelor vortex, for example, it was established by Lessen, Singh and Paillet [58] that $q_c \simeq 1.5$. This relates to a value of $W_{0,c} \simeq 0.66$.

The Moore-Saffman family of velocity profiles describes vortices that develop from laminar flow over a wing. However, in free flight, where the Reynolds number may exceed 10^6 , the airfoil boundary layer is likely turbulent. This motivated Phillips [71] to consider trailing vortices undergoing roll-up behind a lightly loaded wing on which the boundary layer is turbulent. Phillips determines the form of the Reynolds-stress distribution after identifying three regions in the vortex core. He then suggests that two modes for the decay of the peak azimuthal velocity in time are possible: $\sim t^{-n/2}$, which is the rate for the profiles defined in this subsection, and $\sim t^{(n-2)/2}$, a rate to which the decay may asymptote after some time (further behind the wingtip). Here, t denotes time and n is the wing loading parameter.

3.2.2 Linear stability

Varying the wing loading parameter n in the Moore-Saffman vortex model significantly impacts the linear inviscid stability characteristics [34]. The key stability properties are reviewed here. The mean profiles as $n \rightarrow 1$ correspond to the Batchelor vortex mean flow profiles up to an accuracy of 10^{-3} . The growth rates and regions of instability for the

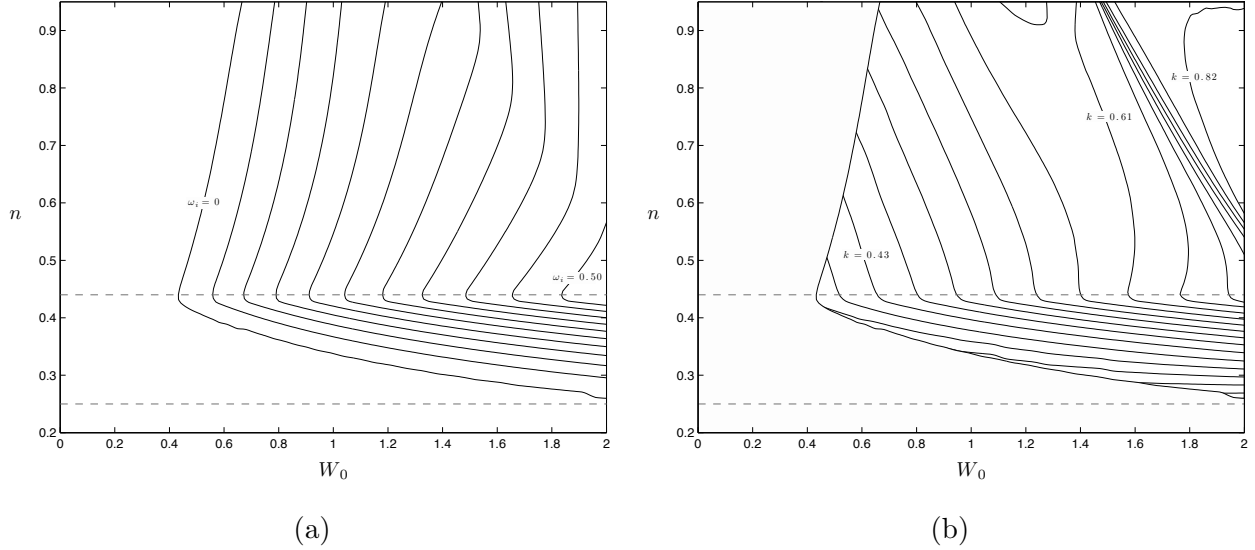


Figure 3.2: For azimuthal wavenumber $m = -1$, both (a) the growth rate ω_i and (b) the corresponding axial wavenumber k for the most unstable inviscid modes for all values in the (W_0, n) -plane are displayed. The contour spacing is 0.05 in (a) and 0.03 in (b), with the outermost contour representing the neutral curve. The horizontal dotted lines mark $n = 0.44$ and $n = 0.25$.

Batchelor vortex have been documented extensively [3, 66] and our findings are in very good agreement with those results. Note that we have exchanged the swirl parameter q for the axial flow parameter $W_0 = 1/q$, as was stated in the previous subsection, and that this causes the growth rates to scale by a factor of W_0 . The effect of viscosity on the inviscid modes of instability is illustrated in this subsection. Many linear modes of instability of the Moore-Saffman vortex possess a critical layer singularity. The existence and role of the critical layer is briefly discussed at the end of this subsection.

Figure 3.2 displays the growth rates and axial wavenumbers of the most amplified $m = -1$ disturbances at every point in the (W_0, n) -plane. First we discuss Figure 3.2(a). The contours on this figure are curves of constant growth rate and the outermost contour represents the neutral curve (corresponding to $W_{0,c}$). The fastest growing mode was calculated independently for every value of the axial flow parameter and the wing loading parameter; each

point on the picture represents the growth rate ω_i of the most unstable perturbation for fixed values of W_0 and n . For example, the most unstable disturbance for $W_0 = 1.00$ and $n = 0.50$ has a growth rate of $\omega_i \simeq 0.2147$. Several conclusions are true for all values of the wing loading parameter n . The axial component $W(r)$ has a destabilizing effect. For $W_0 = 0$, the purely swirling flow is stable for all values of n in the sense that all disturbances decay in time. The flow destabilizes when the axial flow parameter W_0 is increased past a critical value $W_{0,c}$. As mentioned in the previous section, $W_{0,c} \simeq 0.66$ for $n = 0.95$, a value of the wing loading parameter for which the Moore-Saffman profiles closely correspond to those of the Batchelor vortex. For $n = 0.50$, the threshold has decreased to approximately $W_{0,c} \simeq 0.47$. Increasing W_0 past the critical value results in a further destabilization of the linear inviscid modes and an increase of the growth rate of the most amplified disturbance. Two important features of the Moore-Saffman vortex model are visible. First, a decrease in n is associated with a decrease in the critical value $W_{0,c}$. This is true until $n = 0.44$, a constant which is indicated by the upper horizontal dotted line. The vortex is found to become more stable when n is decreased below $n = 0.44$. No unstable disturbances were found for values of the Moore-Saffman parameter lower than $n \simeq 0.25$, depicted on the figure by the bottom dotted line. The neutral curve can be seen to approach the line $n = 0.25$ asymptotically. The fact that $W_{0,c} \rightarrow \infty$ means that no amount of axial flow will cause the damped modes to become unstable. Secondly, the growth rates were found to be greater for $0.44 \leq n < 0.95$ than for the Batchelor vortex, a fact which becomes more pronounced for large W_0 and small n .

The effect of a change in n on the axial wavenumber k of the most amplified wave is clarified in Figure 3.2(b). Plotted is the axial wavenumber of the most amplified mode at every point in the (W_0, n) -plane for which the growth rate was shown in Figure 3.2(a). The contours are curves of constant k . Only unstable modes have been computed; the calculation was halted at the neutral curve, which is visible as the leftmost curve. The most unstable disturbance for $W_0 = 1.00$ and $n = 0.50$, with the aforementioned growth rate of $\omega_i \simeq 0.2147$, has $k \simeq 0.5065$. Interesting variations in k can be observed. Besides an increase in k when

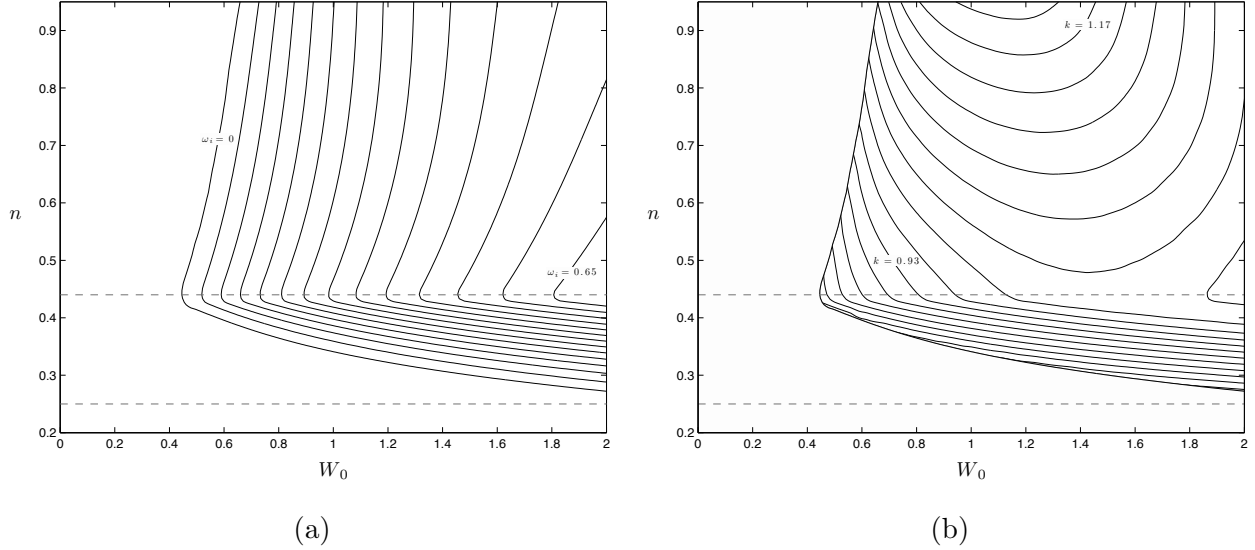


Figure 3.3: Same as Figure 3.2, but for $m = -2$.

n is decreased, a diagonal ridge is visible which marks a region of rapid change in the axial wavelength of the most unstable disturbance. These topographical structures demonstrate that the introduction of an extra parameter n by Moore and Saffman generalizes the known results for the Batchelor vortex in a non-trivial way. The normal modes presented in Figure 3.2 are all primary modes of instability: other growing disturbances, with a lower growth rate, can exist for the same set of parameter values m , n and k . This is true for all unstable azimuthal wavenumbers and this is worth keeping in mind because triadic resonances between these different modes and the strain field have been observed in numerical simulations [50].

Figure 3.3 shows the same information for the fastest growing modes when $m = -2$. The resulting growth rates ω_i are plotted in Figure 3.3(a) and the axial wavenumbers k are shown in Figure 3.3(b). The magnitude of the growth rates in Figure 3.3 is larger than those that were shown for $m = -1$ in Figure 3.2(a). The same trend is observed for higher azimuthal wavenumbers. Normal modes for more negative values of m grow more rapidly, but can be expected to be damped in the presence of viscosity. These findings for the Moore-Saffman vortex model are in line with what is known for the Batchelor vortex. Further observations about the effect of n and W_0 on modes with $m = -2$ are similar to those for the case $m = -1$

discussed earlier. Nevertheless, a glance at Figure 3.3(b), displaying the axial wavenumbers for growing disturbances with $m = -2$, demonstrates that the cases $m = -2$ and $m = -1$ are not qualitatively the same for $0 \lesssim W_0 \lesssim 2$. To begin, modes of instability for $m = -2$ behave differently compared with modes for $m = -1$ when the strength of the axial flow is augmented. The value of k for the most unstable disturbance does not increase monotonically with W_0 . The wavelengths are also shorter for higher azimuthal wavenumbers. For $m = -1$ and $n > 0.44$, k ranges between 0.40 and 0.85. In comparison, the interval for $m = -2$ goes from about $k \simeq 0.80$ to $k \simeq 1.20$.

Unstable perturbations with $m = 1$ exist for all values of n , but their growth rate is small compared to disturbances with $m < 0$. The Moore-Saffman vortex is stable for $m > 1$ and $m = 0$. Even so, several of these stable azimuthal wavenumbers may participate in the elliptical instability process. It is, for example, possible for cooperative instability to cause growth in disturbances with azimuthal wavenumber $m = 0$ through the resonance $(m_1, m_2) = (-2, 0)$. In fact, we will later show that this particular resonant pair manifests itself for the vortex model that is the subject of Part 2 and 3 of this dissertation.

As a further matter, viscosity will be present in Section 3.4. The effect of a finite Reynolds number on the inviscid modes of instability, into which both Mayer and Powell [66] and Ash and Khorrami [3] offer insight, is of a strictly damping nature. The stability properties of the flow are modified markedly at Reynolds numbers that are in the order of 100 and below. Figure 3.4 illustrates the stability properties of the Moore-Saffman vortex model for $Re = 3180$; the growth rates and axial wavenumbers of the fastest growing modes for $m = -1$ are displayed for a large number of points in the (W_0, n) -plane. This figure bears a strong resemblance to Figure 3.2, both qualitatively and quantitatively. It can be observed that $W_{0,c}$, the value of W_0 associated with the onset of instability, equals approximately 0.443 for $Re = 3180$ which is a very slight increase from the inviscid case. For $W_0 = 0.482$, instability occurs for $0.42 \lesssim n \lesssim 0.52$ with a maximum growth rate of $\omega_i \simeq 0.0187$.

To conclude, we highlight the role of critical layer singularities in the linear modes of instability. The importance for the cooperative instability mechanism lies in the fact that

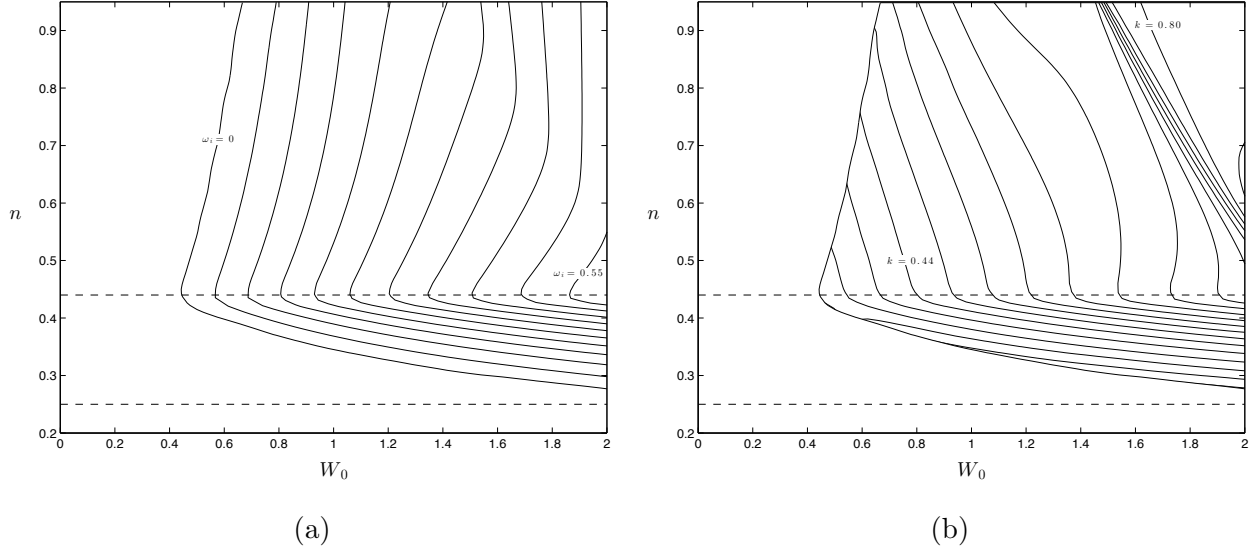


Figure 3.4: Same as Figure 3.2, but for $Re = 3180$.

the critical layer singularity damps neutral modes, thereby reducing the number of possible resonant pairs exhibiting growth [80]. Nevertheless, resonant coupling between a neutral mode and a damped critical layer mode is possible if the coupling is sufficiently strong [50]. The location of the critical layer is determined by a positive real root r_c of the expression

$$\gamma(r) = m \frac{V(r)}{r} + kW(r) - \omega, \quad (3.3)$$

where $\omega = \omega_r + i\omega_i$ is the complex frequency. In the absence of axial flow ($W(r) \equiv 0$), it is clear that a singularity can arise only if the angular frequency ω/m of the normal mode is in the range of the angular momentum of the vortex. Moreover, changing the sign of m only causes the sign of the real frequency ω_r to invert. The situation is complicated by a nonzero axial flow term which breaks this symmetry. The eigenvalue problem for ω has to be solved in that case and care has to be taken near the critical radius r_c . To solve for the eigenmode, the contour of integration must be deformed away from the real positive axis over or under the singularity depending on if the sign of $\gamma'(r_c)$ is negative or positive. The viscous critical layer analysis of Le Dizès [54] shows how to obtain the correct eigenvalue condition for a neutral mode.

3.3 Governing equations and numerical procedure

We consider unsteady perturbations to an incompressible inviscid fluid with a non-axisymmetric mean flow. A numerical routine in cylindrical coordinates (r, θ, z) is implemented to simulate the evolution in time of the perturbation.

3.3.1 Governing equations

The governing equations are obtained in two steps. To begin, a first order expression for the elliptical deformation of the base mean flow is derived. Then, the perturbation equations are obtained by linearizing about the elliptical mean flow.

The non-axisymmetric correction to a base mean flow $[0, V_0(r), W_0(r)]$, for the Moore-Saffman vortex given by (3.2), subject to a stationary dipolar strain field of magnitude ε is detailed in Moore and Saffman [68] in the absence of axial flow ($W_0(r) \equiv 0$). As remarked by Lacaze, Ryan and Le Dizès [50], the presence of an axial velocity component does not complicate matters since it is decoupled from the other velocity components at order ε . The strain field causes an elliptical deformation of the base mean flow, resulting in a velocity field $\bar{\mathbf{u}}$ equal to

$$[\bar{u}(r, \theta), \bar{v}(r, \theta), \bar{w}(r, \theta)] = [0, V_0(r), W_0(r)] + \varepsilon [U_1(r, \theta), V_1(r, \theta), W_1(r, \theta)]. \quad (3.4)$$

An important consequence of the external strain field is the appearance of a radial mean velocity component $U_1(r, \theta)$ at order ε . The correction terms in (3.4) are given by

$$U_1(r, \theta) = -\frac{F(r)}{r} \sin(2\theta), \quad (3.5)$$

$$V_1(r, \theta) = -\frac{F'(r)}{2} \cos(2\theta), \quad (3.6)$$

$$\text{and} \quad W_1(r, \theta) = -\frac{F(r)W_0'(r)}{2V_0(r)} \cos(2\theta), \quad (3.7)$$

where $F(r)$ satisfies the second order ODE

$$F''(r) + \frac{1}{r}F'(r) - \left(\frac{4}{r^2} + \frac{\omega_0'(r)}{V_0(r)}\right)F(r) = 0. \quad (3.8)$$

Here, $\Omega_0 = V_0(r)/r$ is the angular velocity of the base mean flow and $\omega_0 = (rV_0(r))'/r$ is the axial component of its vorticity. The boundary conditions for $F(r)$ are $F(r) \sim r^2$ as $r \rightarrow 0$ and $F(r) \rightarrow 1/r^2$ as $r \rightarrow \infty$. These conditions allow us to determine $F(r)$ in a unique way by solving (3.8) numerically.

In order to obtain equations for a velocity-pressure perturbation $(\tilde{\mathbf{u}}, \tilde{p})$ of order κ , the three-dimensional incompressible Navier-Stokes equations

$$\frac{\partial \mathbf{u}}{\partial t} + (\mathbf{u} \cdot \nabla) \mathbf{u} = -\nabla p + \frac{1}{Re} \nabla^2 \mathbf{u}, \quad (3.9)$$

$$\nabla \cdot \mathbf{u} = 0, \quad (3.10)$$

with Re the Reynolds number, are linearized about the non-axisymmetric mean flow given by (3.4). The equations are expanded in cylindrical coordinates in a manner similar to what was done in Ash and Khorrami [3]. The fluctuations to the steady-state are assumed to be of the form

$$\mathbf{u}(r, \theta, z, t) = \bar{\mathbf{u}}(r, \theta) + \kappa \tilde{\mathbf{u}}(r, \theta, z, t), \quad (3.11)$$

$$p(r, \theta, z, t) = \bar{p}(r, \theta) + \kappa \tilde{p}(r, \theta, z, t). \quad (3.12)$$

They lead to the following equations governing the perturbation:

$$\frac{\partial \tilde{\mathbf{u}}}{\partial t} + (\tilde{\mathbf{u}} \cdot \nabla) \bar{\mathbf{u}} + (\bar{\mathbf{u}} \cdot \nabla) \tilde{\mathbf{u}} = -\nabla \tilde{p} + \frac{1}{Re} \nabla^2 \tilde{\mathbf{u}}, \quad (3.13)$$

$$\nabla \cdot \tilde{\mathbf{u}} = 0. \quad (3.14)$$

The numerical method used to solve the linearized viscous equations given by (3.13) and (3.14) is described in the following section. The domain is unbounded and the only boundary condition that is applied is the decay of the perturbation quantities at infinity. As is usually presumed [50, 31], the slow viscous diffusion of the mean flow $\bar{\mathbf{u}}$ has been neglected in (3.11) and (3.12). The background flow is effectively frozen in time, so that any temporal growth can be directly attributed to the perturbation $\tilde{\mathbf{u}}$.

3.3.2 Numerical method

The three-dimensional linearized Navier-Stokes equations, (3.13) and (3.14), are to be solved in cylindrical coordinates using a spectral method in space and a third order splitting method in time. The problem of spatially discretizing the perturbation quantities $(\tilde{\mathbf{u}}, \tilde{p})$ requires some thought because the physical domain is unbounded and includes the pole at $r = 0$. Clustering of collocation points near the coordinate singularity at the origin can restrict the size of the explicit time step. Care is taken to avoid this by choosing a suitable orthogonal basis of polynomials in the radial direction. First, the details of the spectral discretization in space are given and compared with other standard numerical approaches. Then, the time stepping mechanism is described. Finally, the parameters of the numerical simulation are given.

Spectral methods are a popular choice due to their high accuracy and relative ease of use. The periodicity of the azimuthal variable θ allows a Fourier expansion. The axial variable z does as well, provided that the axial dimension, which is inherently unbounded, is assumed to be periodic. In the radial direction, however, there are numerous families of polynomials which form suitable orthogonal bases. Our numerical routine employs mapped associated Legendre polynomials in the radial variable r . The specifics of this spectral expansion were first formulated by Matsushima and Marcus [64]. The orthogonal polynomials satisfy the pole condition exactly at the coordinate singularity $r = 0$ and their behavior as $r \rightarrow \infty$ is suitable for expanding smooth functions which decay algebraically or exponentially. The associated Legendre polynomials, denoted by P_n^m , generalize the more familiar Legendre polynomials and satisfy a similar recursion. Formulas detailing the recursion relations necessary for manipulating the polynomials P_n^m in spectral function space can be found in Abramowitz and Stegun [1].

Following Matsushima and Marcus [64], the radial variable $0 \leq r < \infty$ is mapped to a computational variable $-1 \leq \mu < 1$ via the algebraic map

$$\mu = \frac{r^2 - L^2}{r^2 + L^2}, \quad (3.15)$$

where $L > 0$ is a map parameter that can be chosen to optimize convergence. After a

considerable amount of algebra, (3.15) eliminates r from (3.13) and (3.14) by substituting in the variable μ instead. All perturbation quantities are then expanded into Fourier/associated Legendre series as follows:

$$\tilde{\mathbf{u}}(\mu, \theta, z, t) = \sum_{k=-K}^K \sum_{m=-N}^N \sum_{n=|m|}^N \tilde{\mathbf{u}}_{k,m,n}(t) P_n^m(\mu) e^{im\theta} e^{ikz}, \quad (3.16)$$

$$\tilde{p}(\mu, \theta, z, t) = \sum_{k=-K}^K \sum_{m=-N}^N \sum_{n=|m|}^N \tilde{p}_{k,m,n}(t) P_n^m(\mu) e^{im\theta} e^{ikz}. \quad (3.17)$$

Here, the integers N and K determine the number of basis functions in the expansion. The complex coefficients $\tilde{\mathbf{u}}_{k,m,n}(t)$ and $\tilde{p}_{k,m,n}(t)$ are the expansion coefficients for the velocity and pressure, respectively.

The truncation of the radial basis in (3.16) and (3.17) is triangular in the sense that higher azimuthal wavenumbers m are associated with fewer radial basis functions. This happens naturally as the associated Legendre polynomials satisfy $P_n^m(\mu) = 0$ for $n < |m|$. Boyd [13] mentions that for spherical harmonics, a triangular truncation gives the most uniform resolution (and allows the longest time step). Although this has not been proven for the associated Legendre polynomial basis, it seems plausible that it is preferable here as well. Quadrature in the variable μ is performed using Gauss-Legendre collocation points. When mapped to the variable r , half of the collocation points are guaranteed to lie between 0 and L . In this way L controls the resolution near the core of the vortex.

The application of associated Legendre polynomials to pseudospectral methods is novel, but was shown to be successful for simulating cooperative instability in [64]. More recently, Bristol *et al.* [14] have investigated the instabilities of a pair of parallel unequal-strength vortices using the same numerical method. The spectral expansion used by these authors differs from the one used in this part of the thesis in an important way. Both [64] and [14] performed a toroidal and poloidal decomposition of the velocity field which eliminates the incompressibility condition (3.14) and reduces the number of unknowns. In lieu of this, we have taken adjoint complex combinations of the radial and azimuthal velocity profiles, thus simplifying the vector Laplacian. Similar considerations apply to the spectral tau-method

proposed by Sakai and Redekopp [79]. That method employs one-sided Jacobi polynomials as radial expansion functions for solving vector field equations defined in polar coordinates.

The spectral method described above has significant advantages over other numerical techniques. When compared to an approach in Cartesian coordinates using a Fourier expansion in all directions, such as the one taken by Faddy and Pullin [32] in conjunction with a special mapping for the axial coordinate developed by Cain, Ferziger and Reynolds [18], our expansion in cylindrical coordinates requires fewer basis functions to achieve a desired accuracy and allows a direct inspection of the azimuthal wavenumbers. The disadvantage is that there is no fast transform to the space of associated Legendre polynomials, thus increasing computational expense. In cylindrical coordinates, there are other polynomial bases that can be used to expand in the radial direction. Several of these are listed in [13], including Bessel functions and Chebyshev polynomials. Bessel functions have been shown to be ill-suited because of slow convergence of the expansion. Gottlieb and Orszag [38] suggest using Chebyshev polynomials for a cylindrical geometry because a fast transform is available. Clustering of the grid points occurs near $r = 0$, however, which severely limits the time step.

Stepping in time in our numerical procedure is performed using a third order stiffly-stable splitting method devised by Karniadakis, Israeli and Orszag [46]. This scheme is similar to Adams-type explicit schemes for time integration, but it has a significantly broader stability region due to the fact that the time derivative is discretized using backwards differentiation. Moreover, the convective terms in (3.13) are handled explicitly while the diffusive terms are implemented implicitly for stability reasons. The lack of a predictive equation for the evolution in time of the pressure stems from the fact that, in an optimization sense, the pressure \tilde{p} is a Lagrange multiplier for the momentum equations associated with the divergence-free constraint. As a consequence, at every time step (of size Δt), a Poisson equation of the form

$$\nabla^2 \tilde{p} = \frac{1}{\Delta t} \nabla \cdot \tilde{\mathbf{u}} \quad (3.18)$$

must be solved to determine the pressure necessary to make the velocity field $\tilde{\mathbf{u}}$ satisfy (3.14). After being initialized to random noise, the disturbance velocity field $\tilde{\mathbf{u}}$ is made divergence-

free by applying a pressure gradient that is calculated in this manner. The disturbance velocity and pressure fields are then advanced in time and quickly become a combination of exponentially growing and decaying modes. The fastest growing modes are identified and the growth rates of these modes are obtained by looking at the gain in their energy.

The equations necessary for time-stepping the expansion coefficients $\tilde{\mathbf{u}}_{k,m,n}(t)$ and $\tilde{p}_{k,m,n}(t)$ given in (3.16) and (3.17), which are obtained from (3.13) and (3.18) via the splitting method formulation, have a convenient form in the sense that coefficients with different azimuthal wavenumber m are mostly decoupled. More specifically, both the pressure gradient and viscous diffusion term are applied to every azimuthal wavenumber independently. There is, however, coupling between azimuthal wavenumbers (that are exactly 2 apart, i.e. $m - 2$, m and $m + 2$) through the effect of the non-axisymmetric correction to the mean flow in the convection term of the governing equation. Nonetheless, the equations allow for an extensive parallelization of the numerical code which in turn reduces simulation runtime drastically. The method is implemented in Fortran 95 using the OpenMP interface for parallel processing.

We now discuss the range of values of the computational parameters that were used in the numerical simulations. The resolution parameter L was found to have a significant impact on the rate of convergence and it is thus necessary to choose this parameter carefully. The optimal value of L was found to lie between 0.5 and 6 and depends primarily on the axial wavenumber k . The radial decay of the modes increases for decreasing k and the collocation points have to be spread out accordingly to ensure accurate results. The time step Δt was chosen to be of order 0.001. This size of time step was found to be sufficient to integrate the governing equation (3.13) as far as $t = 1000$. The asymptotic behavior of the perturbation velocity field was thereby recovered and the dominant modes could be obtained. Axial wavenumbers were usually chosen to be between 1 and 7 with steps of 0.01, unless otherwise stated. The integer N in (3.16) and (3.17) was chosen to be in the order of 60, although accurate results could already be obtained for N as low as 25. Numerically, N determines the number of azimuthal (and radial) wavenumbers. For example, $N = 25$ corresponds to 51 Fourier modes in the azimuthal direction. When N is increased, which

corresponds to increasing the number of azimuthal and radial modes, the time step Δt is decreased. Specifically, Δt is taken to be inversely proportional to N .

3.3.3 Numerical convergence and code verification

Several checks were performed in order to assure that the numerical routine functions as desired. In this subsection, we compare some of our results to previously published data and obtain excellent agreement. In addition, we present convergence analyses of the numerical method in order to show that in most cases a very low number of spectral modes is needed to get an accurate estimate of the instability growth rate. Results are first presented for instabilities in the absence of strain. After this, a strain field is introduced and elliptical instability growth rates are verified.

To begin, we reproduce several published results for modes of instability of the Batchelor vortex in the absence of strain ($\varepsilon = 0$). In Table 3.1, comparisons are presented for two unstable modes: an inviscid mode in the presence of viscosity (Case I) and a viscous center mode (Case II). For Case I, the governing equations were integrated to $t = 300$. For Case II, due to the smaller growth rate of the instability, we integrated until $t = 800$. As is well known, the growth rate of center modes is at least an order of magnitude smaller than that of inviscid modes. In both cases presented, convergence is observed with an increase in the number of basis functions. Looking at Case I, the growth rate of the instability is already determined quite accurately for $N = 10$. Little gain in accuracy is perceived in runs with progressively higher values of N . We find the growth rate to be $\omega_i = 0.32446063$, all digits being significant. Excellent agreement with the numerical results of Fabre and Jacquin [30] and Mao [61] is obtained. Case II is a viscous center mode, which is a mode of instability with a perturbation field concentrated in the vortex center and which occurs only in the presence of viscosity. Convergence is found to be somewhat slower than for Case I which is expected due to the nature of its perturbation velocity field and small growth rate. Viscous center modes are not expected to participate in the elliptical instability mechanism; Case II was examined only to verify our code. The numerical routine yields a growth rate of

	Case I		Case II	
basis functions N	growth ω_i	change (%)	growth ω_i	change (%)
10	0.32447168	3.63×10^{-3}	0.074360	46.21
20	0.32445990	2.28×10^{-4}	0.039996	48.60
30	0.32446064	2.17×10^{-6}	0.020559	3.31
40	0.32446063	0	0.019878	0.71
50	0.32446063	0	0.019736	0.012
60	0.32446063	0	0.019734	0
70	0.32446063	—	0.019734	—
Ref. [30]	0.3245		0.01963	
Ref. [42]	—		0.01974	
Ref. [61]	0.3245		0.019714	

Table 3.1: Code verification against published results for the Batchelor vortex for two cases of vortex instability. Case I is an unstable inviscid mode in the presence of viscosity for $Re = 1000$, $q = 0.761$, $m = -3$ and $k = 1.659$. Case II corresponds to an unstable viscous center mode for $Re = 14000$, $q = 2$, $m = -1$ and $k = 0.268$. The difference column presents the relative error (in percent) between the growth rate in every row and the next.

$\omega_i = 0.019734$, all digits being significant. Many recent computations have been done for this type of mode, for example by [30], [61] and Heaton [42]. Table 3.1 demonstrates that our numerical result agrees well with all three of those investigations.

Next, we look at the Batchelor vortex subject to a strain field of magnitude $\varepsilon = 0.0625$. Figure 3.5 shows numerical convergence results representative of those for all simulations of elliptical instability performed in this study. The results displayed in this figure were obtained for a specific set of flow parameter values and $n = 0.95$, a value of the wing loading parameter for which the mean flow profiles closely resemble those of the Batchelor vortex. We refer to this setup as Case III. For the flow parameters chosen, a resonance occurs

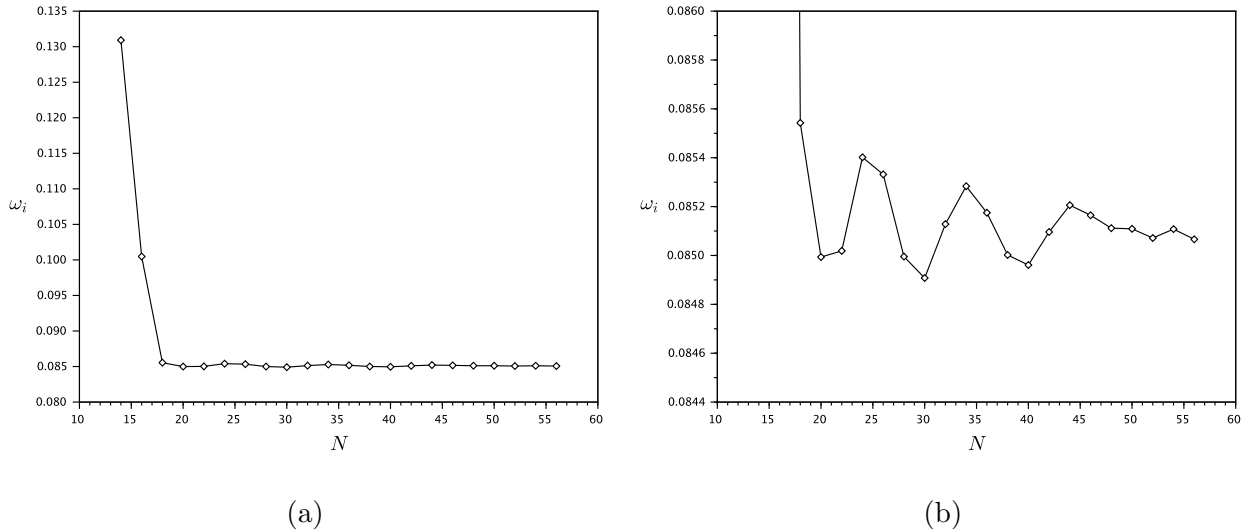


Figure 3.5: Shown in (a) is the convergence of the growth rate ω_i with an increasing number of modes N for Case III. The following parameters are fixed: $n = 0.95$ (approximately Batchelor), $\varepsilon = 0.0625$, and $W_0 = 0.482$, $Re = 3180$ and $k = 1.88$. The resulting elliptical instability is characterized by a resonance between the strain field and azimuthal wavenumbers $(m_1, m_2) = (-2, 0)$. In (b), the region near the asymptotic value of ω_i has been magnified. In both plots, the diamonds represent sample points.

between the strain field and the pair of azimuthal wavenumbers $(m_1, m_2) = (-2, 0)$. For each sample point on the curve, a random initial perturbation velocity field was advanced in time. As was mentioned in the previous subsection, the perturbation growth rate is extracted by running the simulation for a sufficiently long time. To ensure accurate results, the equations for Case III presented here were solved up to time $t = 400$. The most unstable perturbation component quickly develops exponential growth which allows us to extract a numerical growth rate. The growth rate ω_i of the instability was found to be close to 0.0851.

The present results compare favorably with the single previous investigation of this case of which we are aware. The numerical result given by Lacaze, Ryan and Le Dizès [50] is $\omega_i/\varepsilon \simeq 1.23$, which corresponds to $\omega_i = 0.0769$. The same authors report a theoretical prediction equal to $\omega_i/\varepsilon \simeq 1.32$ and this corresponds to $\omega_i \simeq 0.0825$. With regard to

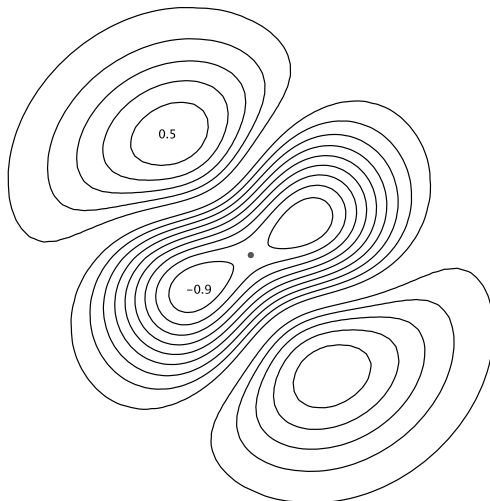


Figure 3.6: The perturbation vorticity field for the unstable mode named Case III. The elliptical instability structure is visible as a combination of modes with azimuthal wavenumber $m_1 = -2$ and $m_2 = 0$. The contours, which are isovorticity lines, are spaced 0.1 apart. The zero vorticity contour is not displayed. Two poles of negative vorticity (with a minimum value below -0.9) and two poles of positive vorticity (with a maximum value above 0.5) exist. The vortex center is marked by a black dot.

convergence, Figure 3.5(a) shows that our computation rapidly approaches an asymptotic value between $N = 14$ and $N = 18$. For higher values of N , a slight oscillation in ω_i is visible, but its amplitude is small and decreasing. A magnified version of the same curve is presented in Figure 3.5(b) and it shows the convergence behavior more clearly. The oscillation amplitude can be seen to diminish rapidly to less than 10^{-4} for $N \approx 50$. This provides clear evidence of the correct functioning of our numerical scheme. A look at Figure 3.6 confirms this conclusion. Displayed in this figure is the perturbation vorticity field associated with the mode of resonance in Case III. The contours shown in this figure can be compared to those in Figure 15(a) from [50]; the modal structures are seen to resemble one another closely.

3.4 Numerical results

The influence of the wing loading parameter n on the growth rate ω_i of the instability is our primary point of interest. The environment parameters are kept constant at a strain rate of $\varepsilon = 0.0625$ and a Reynolds number of $Re = 3180$. We have obtained results for values of the Moore-Saffman wing loading parameter n between 0.25 and 0.95.

Figure 3.7 displays the dependence of the growth rates of the elliptical instability on the axial wavenumber k for the Batchelor vortex and for a number of values of n . The axial flow parameter is maintained at $W_0 = 0.482$. Notwithstanding that this allows the possibility of instability of the Moore-Saffman base flow for $0.42 \lesssim n \lesssim 0.52$, as was indicated in Section 3.2.2, the growth associated with the instability is very slow (its growth rate is smaller than 0.02) and therefore not expected to interfere with our goal of tracking the elliptical instability. The results for the Batchelor vortex, displayed in Figure 3.7(a), consist of a series of parabolic arcs in narrow bands which correspond to different resonant pairs of azimuthal wavenumbers. We find the three most unstable axial wavenumbers to be $k \simeq 1.86$, $k \simeq 3.23$ and $k \simeq 4.55$. The corresponding growth rates are $\omega_i \simeq 0.0852$, $\omega_i \simeq 0.0780$ and $\omega_i \simeq 0.0693$, respectively. All three modes were found by previous investigations to be principal modes; they are associated with a resonance between modes having the same radial (nodal) structure. Separating them are branches of less unstable modes, at approximately $k \simeq 2.56$ and $k \simeq 3.85$, which are composed of non-principal modes. The present numerical study can determine the azimuthal and radial structure of elliptical modes of instability, but it can not ascertain if a mode is principal or not. Analytical estimates are necessary to do that.

In comparison, for the same parameter configuration, Lacaze, Ryan and Le Dizès [50] present the resonant modes in Figure 14 and Table 1 of their paper, employing $\sigma = \omega_i/\varepsilon$ to express the growth rate. It is the sole reference of which we are aware that contains detailed information regarding growth rates for the cooperative instability of counter-rotating Batchelor vortices. The present findings are in good agreement with the results shown there,

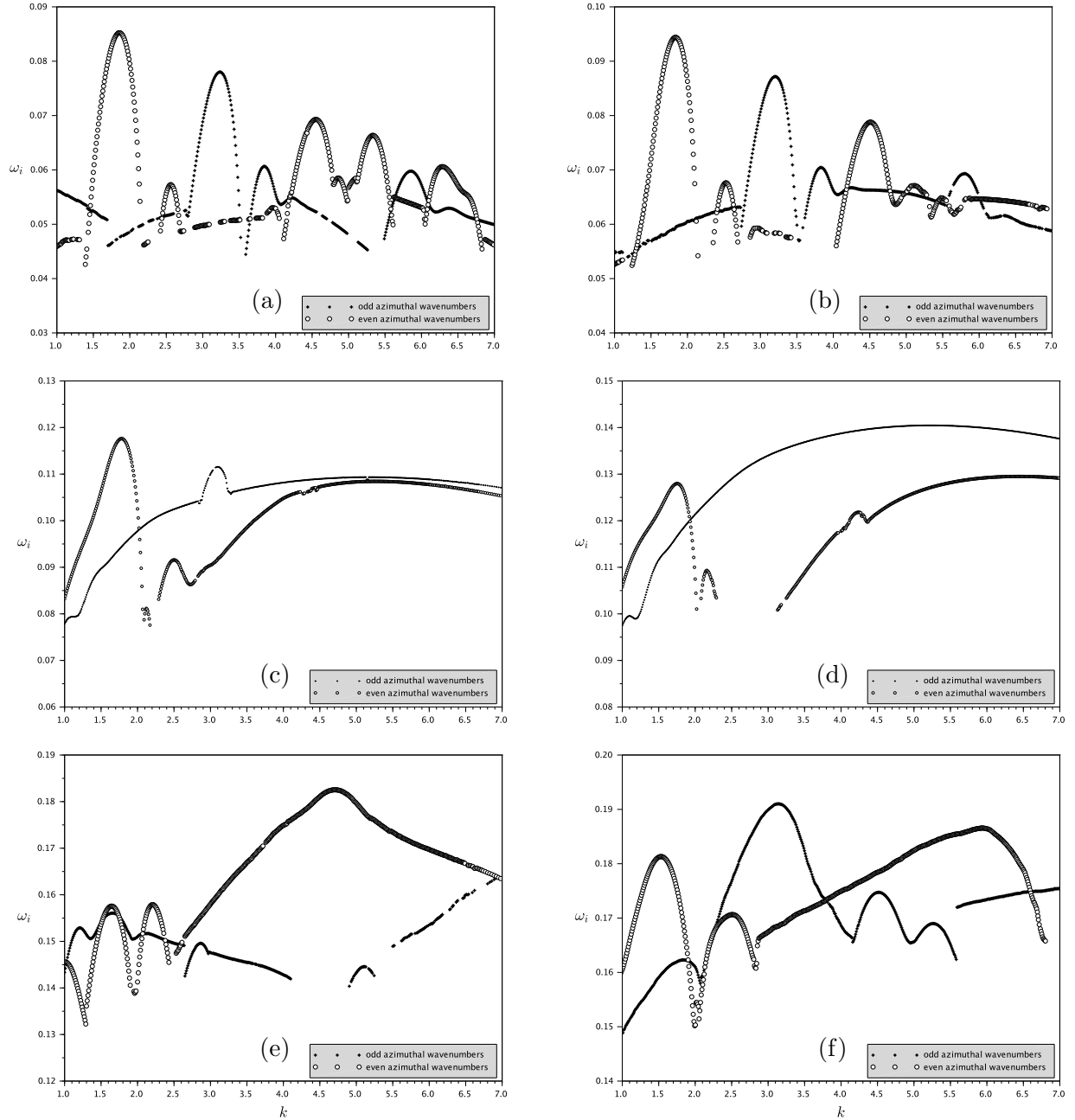


Figure 3.7: The growth rate ω_i as a function of the axial wavenumber k is presented for a number of different mean flow velocity profiles. In (a), results for the Batchelor vortex are shown. In the other plots, Moore-Saffman profiles are used with the wing loading parameter n fixed at (b) $n = 0.95$, (c) $n = 0.80$, (d) $n = 0.70$, (e) $n = 0.50$ and (f) $n = 0.30$. The flow parameters are maintained at $\varepsilon = 0.0625$, $W_0 = 0.482$ and $Re = 3180$ throughout. Resonances of odd and even azimuthal wavenumbers are plotted on different curves. Note the different bounds on each vertical axis.

particularly the locations of the maxima of the growth rate. There is a slight departure in the values of the growth rates themselves. The deviation increases when k is increased. It is worthwhile to briefly point out three dissimilarities between the current study and two interconnected prior investigations, namely [50] and Roy *et al.* [76], although the latter deals mostly with co-rotating vortex pairs. A first difference resides in the fact that we model the effect of the strain field as a first order correction to a single vortex, and use this velocity field to linearize the governing equations. Secondly, since the simulation is performed in cylindrical coordinates, it is able to identify, independently for even and odd azimuthal wavenumbers, two potentially unstable elliptical modes per axial wavenumber k . A third difference, again related to the numerical method taking advantage of the cylindrical geometry, is that we are not obliged to look at the perturbation vorticity field to identify the azimuthal structure of the unstable mode. The first point mentioned here implies that, as is common in stability studies, the strained mean velocity field satisfies the Euler equations at first order of the strain field, but not the Navier-Stokes equations. The impact of this fact on the results is expected to become more significant as k increases.

The other graphs in Figure 3.7 present numerical results for the elliptical instability of the strained Moore-Saffman vortex for various values of n . Figure 3.7(b) demonstrates how the growth rates of the instability vary with k for $n = 0.95$. Although the mean velocity profiles for this value of n closely approximate those of the Batchelor vortex in the near field, the asymptotic behavior for large r is not the same. For instance, the axial mean velocity $W(r)$ decays algebraically and not exponentially for $r \rightarrow \infty$. The growth rates obtained are about 10 percent larger than those for the Batchelor vortex, while the location of the growth maxima is mostly unchanged. Reducing the wing loading parameter to $n = 0.80$, results for which are shown in Figure 3.7(c), produces considerably different results. The growth rates of the elliptical modes are larger than those for $n = 0.95$. Moreover, the narrow bands of unstable axial wavenumbers are exchanged for a continuum of unstable wavenumbers. This phenomenon, which we attribute to the presence of a continuum of unstable modes with short wavelength, is discussed in some detail in the section on the ultra short-wave

cooperative instability (Section 12.4) of the book by Saffman [78]. The existence of a large growth envelope has also been reported by [76], specifically in Figure 9 of their paper, where it is illustrated for the case of a pair of co-rotating vortices with no axial flow, and in their Figure 6, where axial flow is present. The most amplified modes for low values of k are resonances between Kelvin modes with even azimuthal wavenumber m . For larger values of k , above $k \simeq 2.02$, elliptical modes composed of odd values of m are most amplified.

Several observations specifically concern the curve of even resonating wavenumbers in Figure 3.7(c), where $n = 0.80$. These unstable modes are located on parabolic branches only for $k \lesssim 2.73$. The resonances in that region are partitioned in three adjacent bands of instability, centered at $k \simeq 1.78$, $k \simeq 2.12$ and $k \simeq 2.50$. The unstable modes consisting of even azimuthal wavenumbers are situated on a continuous branch in the shape of a wide arc. A single parabolic band with an amplification peak near $k \simeq 3.10$ is visible. Figure 3.7(d), displaying results for $n = 0.70$, exhibits similar features. No instability associated with even values of m is detected between $k \simeq 2.28$ and $k \simeq 3.13$. Resonances between even azimuthal wavenumbers are the most amplified elliptical disturbance for $k \lesssim 1.93$. With an average growth rate of $\omega_i \approx 0.125$ across the spectrum of axial wavenumbers, the flow is more unstable than that for higher values of n . The situation for $n = 0.50$, displayed in Figure 3.7(e), reveals a more complex structure. Aside from a further increase in the growth rate, resonances of even wavenumbers are the most unstable practically throughout the domain k . Finally, computations for $n = 0.30$, in Figure 3.7(f), show that this case has growth rates comparable to $n = 0.50$. Both curves in this figure include several parabolic segments. Figs. 3.7(b)-3.7(f) illustrate the significant influence of the wing loading parameter n on the elliptical instability. In light of previous investigations, viz. [49, 50, 76], which have included the effect of axial flow, the complicated dynamics we have observed to be associated with a change in n may be understood to stem from the fact that variations of this parameter profoundly change the shape of the axial mean velocity $W(r)$ (see Figure 3.1(b)).

The plots displayed in Figure 3.8 confirm the aforementioned conclusion. They demonstrate the dependence of ω_i on n for fixed values of the axial wavenumber k . The magnitude

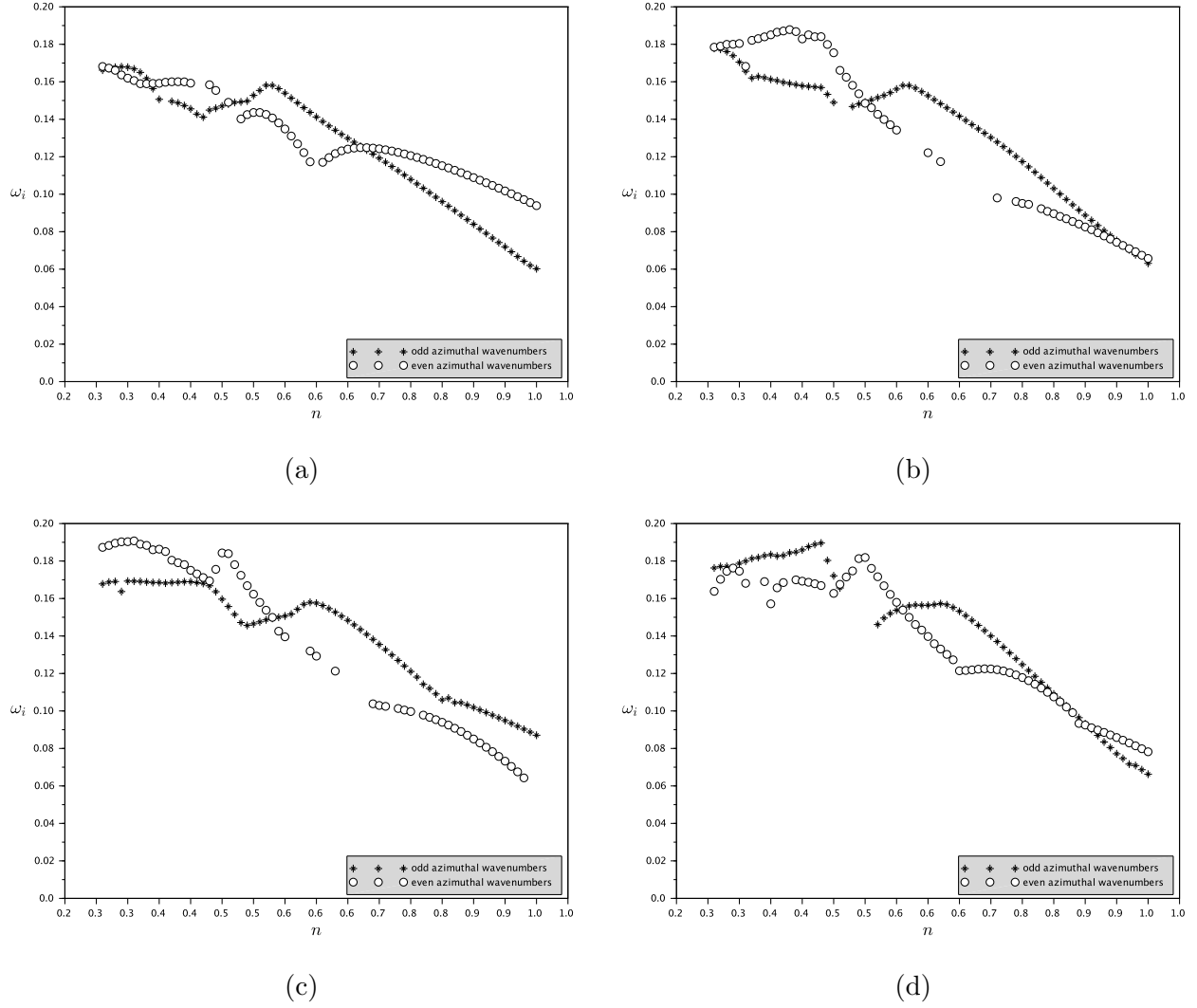


Figure 3.8: The growth rate ω_i as a function of the wing loading parameter n for fixed flow parameters $\varepsilon = 0.0625$, $W_0 = 0.482$ and $Re = 3180$. The value of the axial wavenumber is held steady at (a) $k = 1.88$, (c) $k = 2.60$, (c) $k = 3.23$ and (d) $k = 4.57$. Resonances of odd and even azimuthal wavenumbers are represented by star and circle symbols, respectively.

of the other flow parameters ε , W_0 and Re was kept unchanged from Figure 3.7. The values of k were chosen to be the four most amplified axial wavenumbers for the Batchelor vortex. For $k = 1.88$, shown in Figure 3.8(a), the resonant principal pair $(m_1, m_2) = (-2, 0)$ is the most unstable for $n \gtrsim 0.67$. When n is decreased below that value, a resonance between odd wavenumbers becomes the most amplified disturbance. This continues until $n \simeq 0.46$, below which value of n several interchanges between odd and even resonant pairs as the most dominant instability take place. The maximum growth rate increases from $\omega_i \simeq 0.0939$ for $n = 0.95$ to $\omega_i \simeq 0.153$ for $n = 0.50$, the value of the wing loading parameter that corresponds to elliptical wing loading. Lowering n further, we find $\omega_i \simeq 0.168$ for $n = 0.30$. This means the instability intensifies somewhat below $n = 0.44$. The plot for $k = 2.60$, displayed in Figure 3.8(b), encompasses a similar exchange of dominant resonant pairs. The coupling $(m_1, m_2) = (-2, 0)$ is only slightly more unstable than an odd resonant pair for $n = 0.95$. For lower values of n , this odd resonance grows more rapidly, until $n \simeq 0.50$, when another switch takes place. In all, the growth rate increases from $\omega_i \simeq 0.0657$ for $n = 0.95$ to $\omega_i \simeq 0.188$ for $n = 0.38$, a near threefold increase. Figure 3.8(c), for which $k = 3.23$, exhibits a similar destabilization with a decrease in n . Here $(m_1, m_2) = (-3, -1)$ is most unstable until $n \simeq 0.53$. Below this value of n , resonances between even azimuthal wavenumbers are most amplified, although the exact resonant configuration (m_1, m_2) is changing. The value of ω_i can be seen to almost double between $n = 0.95$ and $n = 0.30$. Figure 3.8(d) presents similar results for $k = 4.57$. In the four cases that were presented in Figs. 3.8(a)-3.8(d), the growth rates reach a peak magnitude in the vicinity of $n = 0.40$. They remain elevated for values of n below that. This contrasts with the inviscid modes of instability of a single Moore-Saffman vortex, discussed in Section 3.2.2, which are most unstable for $n = 0.44$.

Figure 3.9 presents the growth rate of the most amplified cooperative disturbance for every point in the (k, n) -plane. Figure 3.9(a) gives an overview of the findings we have discussed so far in this section for $W_0 = 0.482$, given that the flow parameters have been kept at the same value as in Figs. 3.7 and 3.8. For every value of k and n , the most unstable mode is given irrespective of whether the resonance is between even or odd azimuthal

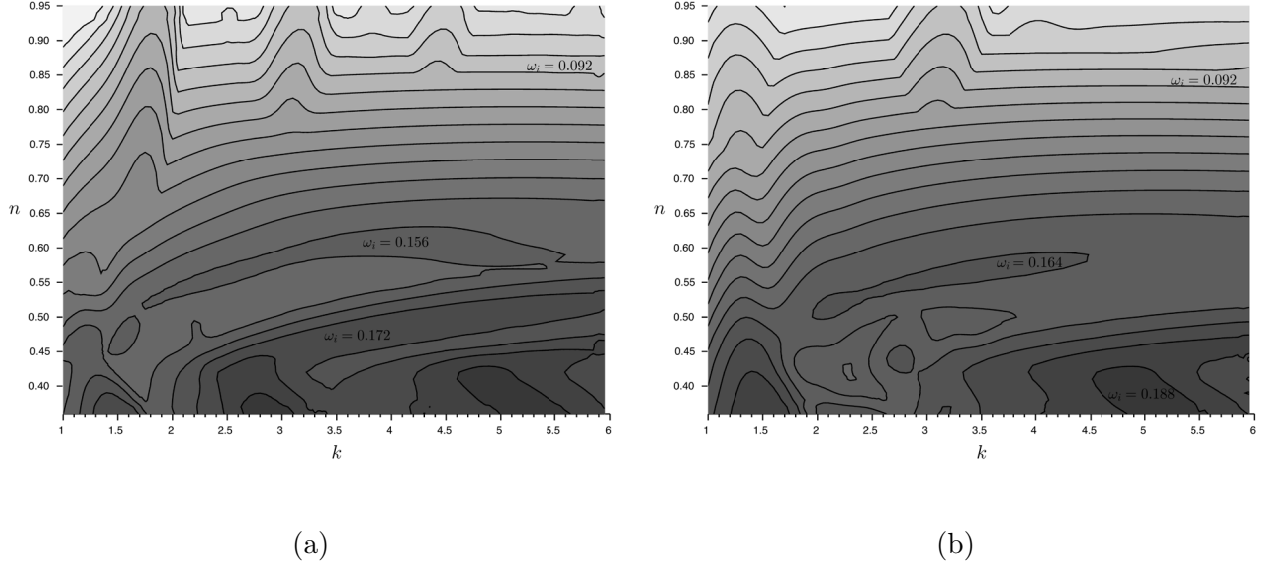


Figure 3.9: Contour plots of the maximum growth rate ω_i for every value of the axial wavenumber k and wing loading parameter n are presented for (a) $W_0 = 0.482$ and (b) $W_0 = 0.2494$. The other flow parameters remain fixed at $\varepsilon = 0.0625$ and $Re = 3180$. Every point shows the most unstable resonance for a given value of (k, n) . The contours are curves of constant growth rate. The spacing between the contours is 0.008. In each plot, several contours have been labeled for clarity.

wavenumbers. One prominent feature is the increase in growth rate of the instability that is associated with a decrease in n . Further, the appearance of a continuum of unstable modes rather than narrow bands can be observed, in particular for $0.60 \lesssim n \lesssim 0.80$. The peaks in growth rate at $k \simeq 4.57$, $k \simeq 3.23$ and $k \simeq 1.88$ remain nearly stationary, although they get absorbed by the continuum when n is decreased. In order, they disappear as k decreases at approximately $n \simeq 0.85$, $n \simeq 0.75$ and $n \simeq 0.65$. For large values of k , there is a continuum of unstable modes for all values of n . These are modes of instability with very short axial wavelength. Below $n \approx 0.50$, the resonances for low axial wavenumbers once again group in parabolic arcs.

In Figure 3.9(b), the same data is shown for a reduced axial flow parameter of $W_0 = 0.2494$, well within the linearly stable regime described in Section 3.2.2. Even though there

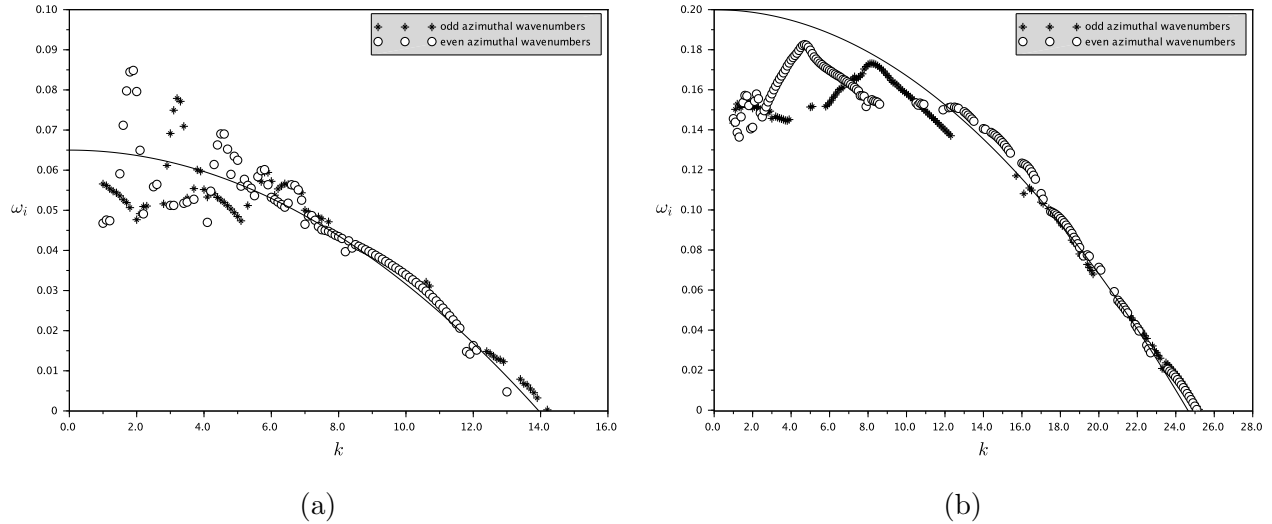


Figure 3.10: The growth rate ω_i as a function of the axial wavenumber k for fixed flow parameters $\varepsilon = 0.0625$, $W_0 = 0.482$ and $Re = 3180$, shown for (a) the Batchelor vortex and (b) the Moore-Saffman vortex with $n = 0.50$. The solid line displays the damping due to viscosity. The viscous decay rate is estimated using the expression $-(k^2/Re)(1 + \varepsilon/(\gamma - \varepsilon))$. Resonances of odd and even azimuthal wavenumbers are represented by star and circle symbols, respectively.

is a reduced axial mean flow, the growth rates are of a magnitude comparable to those for $W_0 = 0.482$. This figure has many of the same properties we noted in Figure 3.9(a). The resonance that can be observed near the left edge of the figure, with a peak growth rate at $k \simeq 1.27$, corresponds to the principal mode $(m_1, m_2) = (-2, 0)$. It persists when n is decreased. Another elliptical instability for the Batchelor vortex, located at $k \simeq 3.22$, vanishes when n is decreased. It becomes swamped by the continuum of modes that exists for large values of k .

Figure 3.10 displays detailed results for the large axial wavenumber behavior of the instability growth rates for the Batchelor vortex and the Moore-Saffman vortex with $n = 0.50$. The instabilities for large values of k are to an increasing extent damped by viscosity as Re increases. Landman and Saffman [51] found an estimate for the time-averaged viscous decay rate, which they denote by σ_V . For a small strain rate $0 < \varepsilon \ll 1$, their expression is

bounded from above by

$$-\frac{k^2}{Re} \left(1 + \frac{\varepsilon}{\gamma - \varepsilon} \right), \quad (3.19)$$

where γ is a positive constant equal to two times the constant axial vorticity at the vortex center. The intuitive formula $-k^2/Re$ for the viscous damping is recovered for the unstrained case ($\varepsilon = 0$). The approximation given in (3.19) is represented by a solid line in Figure 3.10. The line correlates well with the data in both plots of this figure. Note that the predicted viscous decay rate is not the same for Figs. 3.10(a) and 3.10(b) since the core axial vorticity of the base mean flow depends on n . While the value for the Batchelor vortex is $\gamma = 1$, the corresponding quantity for the Moore-Saffman profiles is more elevated, as can be anticipated from Figure 3.1. The larger core axial vorticity for the Moore-Saffman vortex with $n = 0.50$ leads to an elevated value of $\gamma = 1.2818$ in Figure 3.10(b). As a consequence, a reduced amount of viscous damping can be expected for any value of n for the Moore-Saffman mean flow profiles. This reasoning does not take into account the presence of an axial flow. No instability persists past a critical value k_c of the axial wavenumber. We have determined the precise point of viscous cutoff for a limited number of parameter sets. In Figure 3.10(a), which displays results for a Batchelor mean flow, the viscous cutoff point is situated at $k_c \simeq 14.20$. Figure 3.10(b) presents similar findings for the elliptical modes of the Moore-Saffman vortex with $n = 0.50$, but the axial wavenumber at which cutoff occurs is $k_c \simeq 25.19$, significantly larger than the aforementioned value for the Batchelor vortex.

In order to address another important question, namely, the effect of the axial flow parameter W_0 on the instability growth rates, we have employed our numerical routine for a wide range of points in the (k, W_0) -plane. We have done this for several values of n . The results are plotted in Figure 3.11. The topography of the contours for $n = 0.95$, in Figure 3.11(a), demonstrates the major impact of W_0 on both the resonant pairs and their growth rates. Increasing W_0 causes a shift in the horizontal position of the resonant pairs, which are seen as islands on this figure. The three resonant pairs that are apparent for $W_0 = 0$, all of which correspond to resonances $(m_1, m_2) = (-1, 1)$ and have undergone close examination in the literature on the Lamb-Oseen vortex, already become damped for a small amount of axial

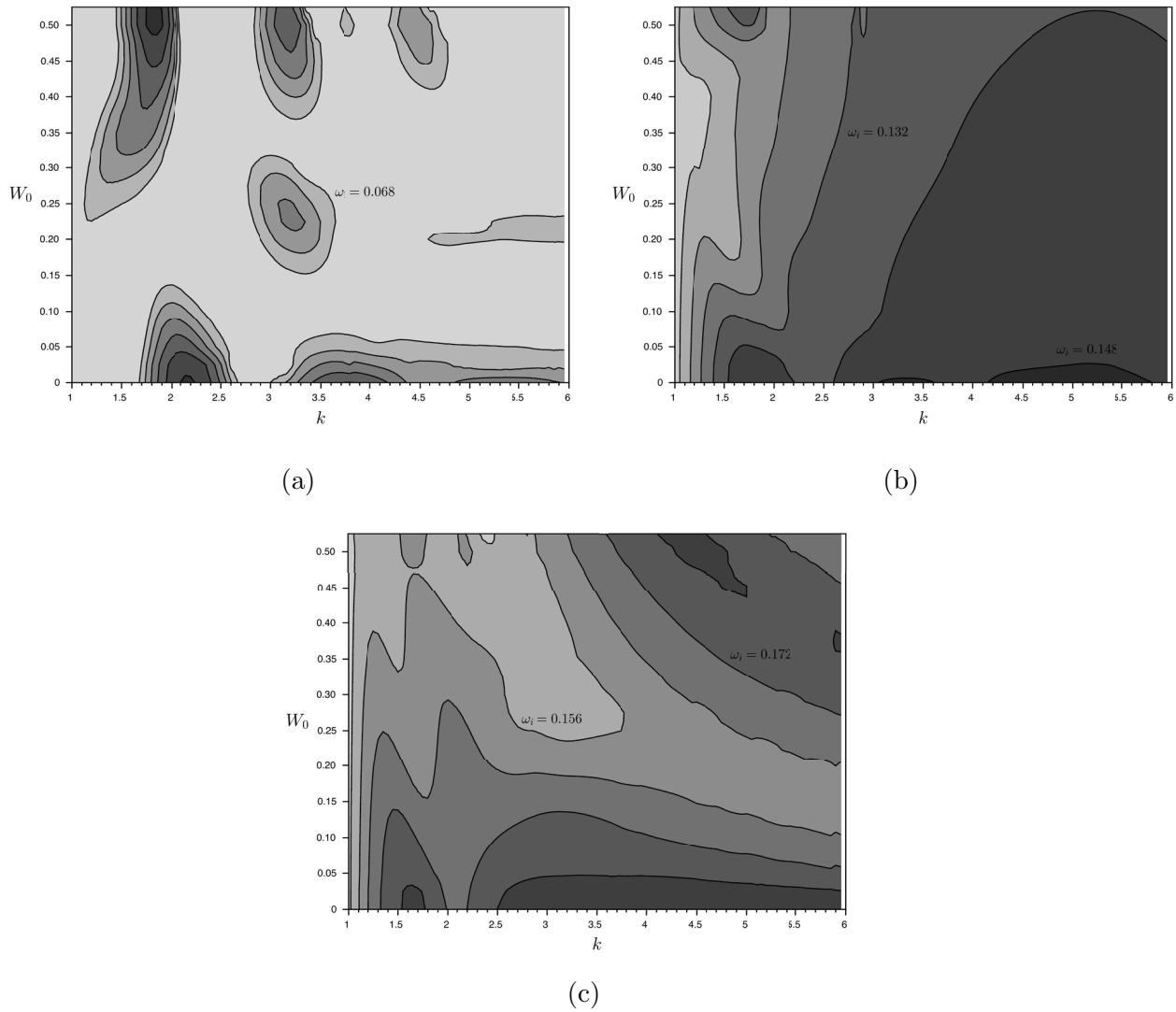


Figure 3.11: Contour plots of the maximum growth rate ω_i for a wide range of values of the axial wavenumber k and axial flow parameter W_0 . The wing loading parameter equals (a) $n = 0.95$, (b) $n = 0.70$ and (c) $n = 0.50$. The other parameters remain fixed at $\varepsilon = 0.0625$ and $Re = 3180$. For each value of (k, W_0) , the growth rate of the most unstable resonance is shown. The contours are curves of constant growth rate and they are spaced 0.008 apart in each plot. Several contours have been labelled for clarity.

mean flow. Other resonances arise and disappear as W_0 is increased to $W_0 = 0.525$. In Figure 3.11(b), which presents data for $n = 0.70$, a very different picture emerges. The continuum of modes is observable on the right, while a fine structure in the contours is conspicuous for $k \lesssim 2$. The growth rates decrease when the axial flow parameter is increased from $W_0 = 0$, with a minimum being attained at $W_0 \simeq 0.36$. When more axial velocity is included in the mean flow model, up to $W_0 = 0.525$ at which point the computation was halted, the growth rates can be seen to once again increase. Overall, however, the amplification rates are significantly higher than those for the Batchelor vortex. We find the most amplified mode to occur for a value of $k \simeq 5.21$, independent of W_0 . A glance at Figure 3.11(c), for $n = 0.50$, shows more fine structure visible for $k \lesssim 3$. The growth rates are larger than for the previous cases discussed in this figure. In contrast to $n = 0.70$, the vortex seems to stabilize for increasing values of k which can be seen from the descending trend in the contours.

Besides distinguishing between odd and even resonant azimuthal wavenumbers, as was done in Figs. 3.7, 3.8 and 3.10 with regards to growth rate, we have looked into the exact resonant configuration that exists for specific parameter sets by calculating the energy of each azimuthal Fourier mode of the perturbation velocity fields. As an example, Figure 3.12 displays the partition diagram of the case $n = 0.50$ shown earlier, in Figure 3.11(c). In the absence of axial flow ($W_0 = 0$), the resonance between $m_1 = -1$ and $m_2 = 1$ is the most unstable elliptical mode of instability for all k . When W_0 is increased, the coupling $(m_1, m_2) = (0, 2)$ becomes unstable, first for large axial wavenumbers. Smaller islands, which correspond to the resonance $(m_1, m_2) = (-2, 0)$, can be seen in this figure. The first of these islands appears at $W_0 \simeq 0.22$ and three more are visible for $W_0 \gtrsim 0.38$. As such, an increase in axial flow causes a progression of the dominant mode of elliptical instability, from $(m_1, m_2) = (-1, 1)$ for W_0 to multiple resonant pairs for $W_0 = 0.525$. We do not, however, obtain more negative resonant pairs (such as $(-3, -1)$ or $(-4, -2)$) for the Moore-Saffman vortex with $n = 0.50$, which differs from the results of [50] for the Batchelor vortex. In fact, the findings in Figure 3.12 are reminiscent of the ones presented by Lacaze, Birbaud

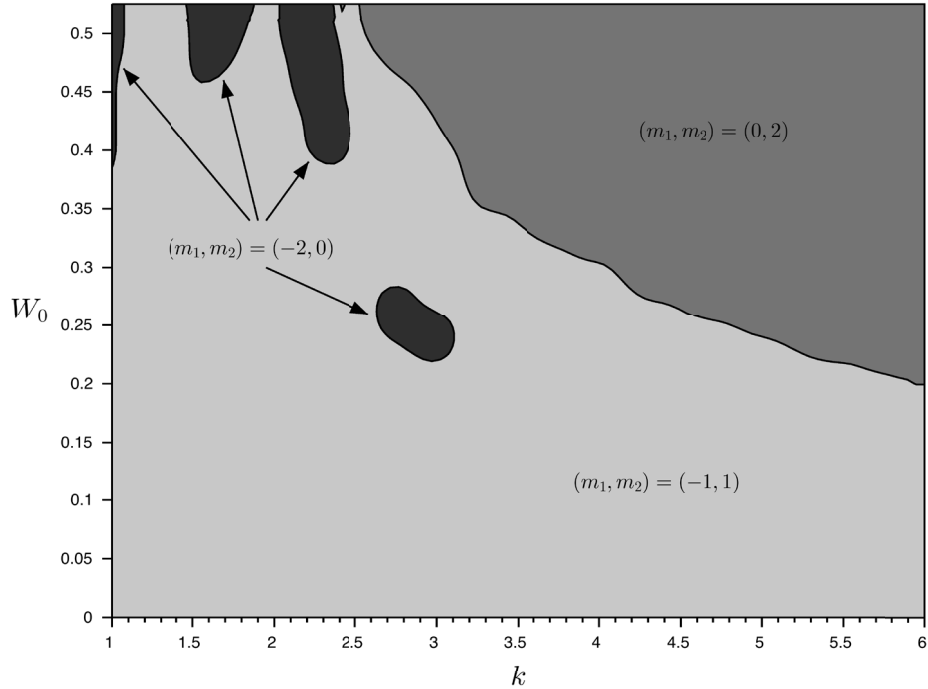


Figure 3.12: Partition diagram showing the most unstable resonant pair for every point in the (k, W_0) -plane for $n = 0.50$, $\varepsilon = 0.0625$ and $Re = 3180$. The corresponding growth rates are shown in Figure 3.11(c).

and Le Dizès [49] for a Rankine vortex with constant axial flow. The results in their Figure 6, which displays a partition of the $(W_0, \varepsilon Re)$ -plane according to which dominant resonant pair occurs, show some similarity to ours, provided that we set $\varepsilon = 0.0625$ and $Re = 3180$. Note that only a resonance of $m = 0$ and $|m| = 2$ was observed by Roy *et al.* [75] in an experimental setup of a pair of counter-rotating vortices with axial core flow.

In order to better visualize the three dimensional shape of the perturbations discussed in this section, we have computed the entire spatial structure of the perturbation vorticity field for a selection of elliptical modes of instability. Images for $n = 0.95$ are shown in Figure 3.13. Four setups with decreasing axial wavelength are presented, namely, $k = 1.88$, $k = 3.23$, $k = 3.85$ and $k = 4.57$. The wavelength is marked on a longitudinal axis running parallel to the vortex axis. The vortex axis itself is situated at the point of symmetry. The corresponding resonant pairs are $(m_1, m_2) = (-2, 0)$, $(-3, -1)$, $(-3, -1)$ (but a non-principal

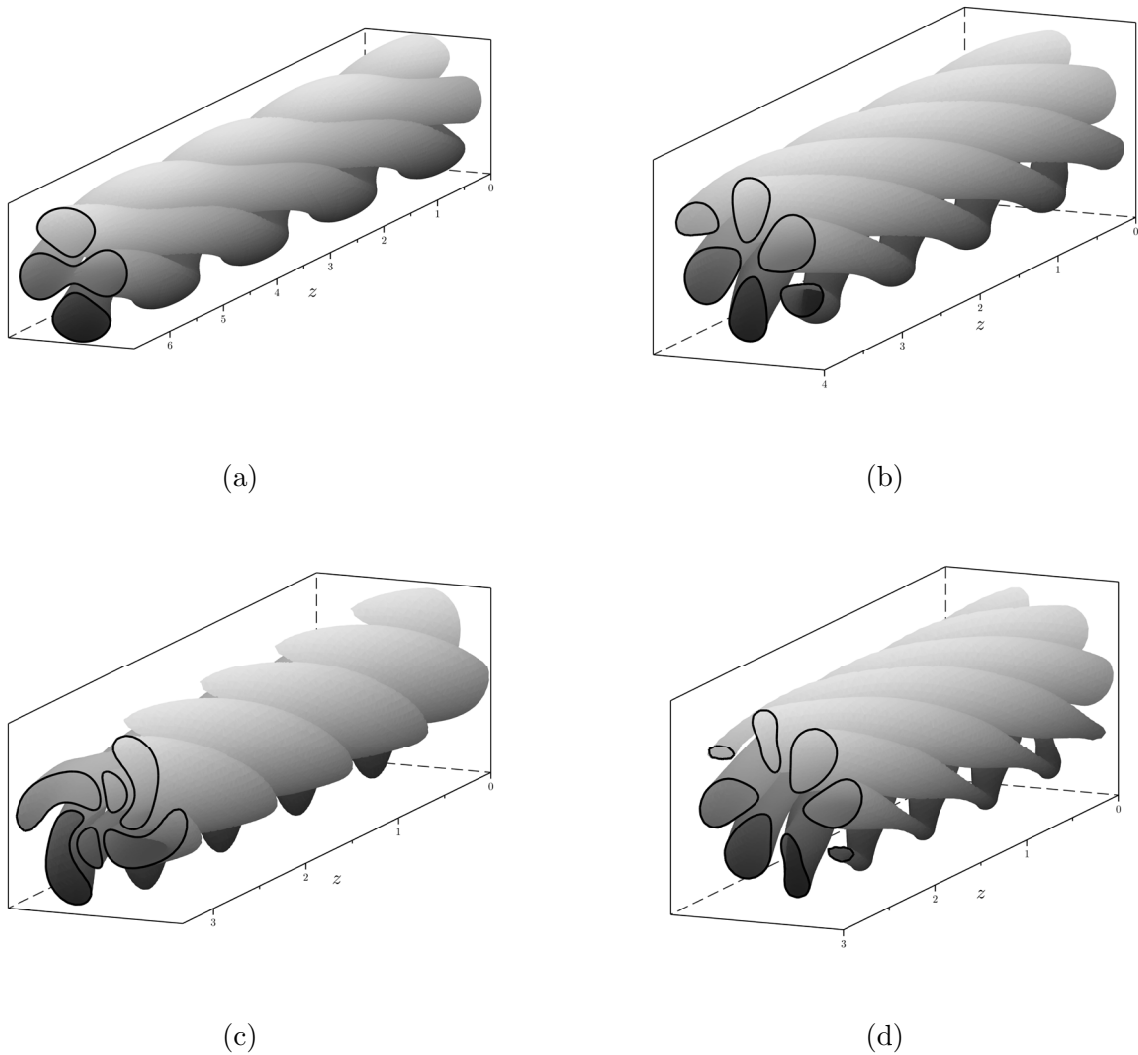


Figure 3.13: Perturbation isovorticity surfaces for a number of highly amplified modes for $n = 0.95$. The axial wavenumber equals (a) $k = 1.88$, (b) $k = 3.23$, (c) $k = 3.85$ and (d) $k = 4.57$, while the other parameters remain fixed at $\varepsilon = 0.0625$, $W_0 = 0.482$ and $Re = 3180$. Two isosurfaces, representing 25% and -25% of the maximum magnitude of the axial component of perturbation vorticity, are displayed in each plot. The shape of the surfaces is emphasized by thick isovorticity contours in the front plane.

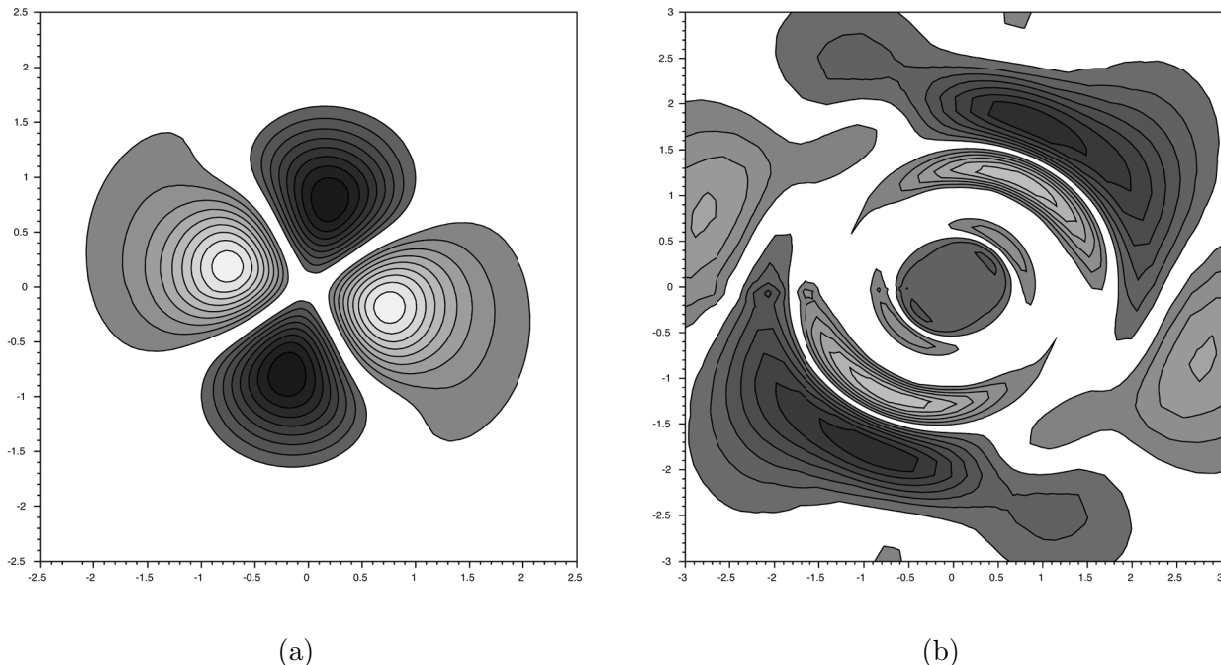


Figure 3.14: Perturbation isovorticity contours for (a) $n = 0.70$ with $k = 1.75$ and (b) $n = 0.50$ with $k = 4.60$. The other parameter values are $\varepsilon = 0.0625$, $W_0 = 0.482$ and $Re = 3180$.

mode) and $(-4, -2)$, respectively. They are akin to the most unstable modes identified for the Batchelor vortex.

Finally, in Figure 3.14, we display isocontours of the axial component of the perturbation vorticity field for two selected modes of instability for $n < 0.95$. Both images illustrate resonances of the type $(m_1, m_2) = (0, 2)$, but their structure is very distinct. The eigenmode in Figure 3.14(a) is located on the leftmost parabolic branch in Figure 3.7(d) and its modal structure shows a clear fourfold symmetry across the origin. Figure 3.14(b) is situated on the wide arc in Figure 3.7(e) and its vorticity field is concentrated around a circle with radius close to 1.75. We find that other modes on the continuous branch have a similar structure, which resembles the images in Figure 10 of [76]. It is suggested there that the spiral structure is associated with a critical layer in one of the resonant modes. The precise nature of these modes and their particular structure invites further investigation.

3.5 Concluding remarks

In Part 3 of the thesis, we examined the elliptical instability of the Moore-Saffman model for a trailing vortex. As shown in Figure 3.1(b), its axial mean velocity component is quite sensitive to changes of the wing loading parameter n . We have found the presence of this axial flow, the magnitude of which is controlled by the parameter W_0 , to strongly impact the properties of the elliptical modes of instability. In comparison to the Batchelor vortex, which is approximated accurately by the choice $n = 0.95$, the instability growth rates are larger for $n < 0.95$.

The wing loading parameter n has been found to impact the stability characteristics in three important ways. First, reducing the value of n significantly increases the growth rates of the unstable modes. This was also the case for the inviscid linear stability characteristics of the Moore-Saffman model obtained by Feys and Maslowe [34]. However, in contrast to the linear modes of instability in that study, we did not find that a decrease in n below $n = 0.44$ resulted in a rapid damping of the elliptical modes of instability. Rather, the growth rates for $n \lesssim 0.50$ remain at elevated levels, between double and triple that for $n = 0.95$. Secondly, the numerical results presented for the growth rates demonstrate the complex interchange of resonant pairs that is associated with varying n . The results presented in Figure 3.8, for example, are composed of curve sections involving different couplings of azimuthal wavenumbers which become dominant in a successive fashion. The computations performed over the course of this investigation revealed numerous interchanges of this kind. However, we have only performed an initial examination of the partition of the parameter space according to the dominant resonant interaction. Finally, we have found a continuum of modes to be present, even for relatively small values of the axial wavenumber k . The continuum can be seen as a wide band of unstable modes, rather than narrow regions of instability centered about a particular value of k . Somewhat similar results, albeit for a pair of co-rotating Batchelor vortices, were obtained by Roy *et al.* [76]. Understanding the mechanism responsible for these modes of instability, together with the reason why the instability band widens with decreasing values of n , requires more investigation.

The parameter space for the problem examined in this part of the thesis, comprised of the quintuplet $(\varepsilon, Re, W_0, n, k)$, is extensive and has not been explored fully. In particular, the effect of the Reynolds number and the strain rate (through the quantity εRe) should be looked into further. Finally, the growth rates yielded by the numerical simulation could be compared to theoretical predictions, as was done for co-rotating Batchelor vortices by Lacaze, Ryan and Le Dizès [50].

Summary

In this thesis, we examined three problems in fluid mechanics. The first involved long nonlinear waves on a shear flow. The evolution in time of the amplitude of these waves is governed by the Korteweg-deVries equation. Our focus was the eigenvalue problem that determines the speed of propagation of long nonlinear surface waves and, in particular, modes with nonlinear critical layers. To this end, we solved the Rayleigh equation searching for singular neutral modes for a variety of continuous shear flows with a free surface. This is significant given that many studies have disregarded the presence of these currents altogether, or have assumed them to be uniform or irrotational. First, we numerically obtained singular modes for a family of hyperbolic tangent shear flows. Certain sets of parameters returned modes with a critical layer that was in close proximity to the wall; this led us to review the theory of nonlinear critical wall layers. Next, we looked at the family of Falkner-Skan boundary layer profiles, which includes the Blasius boundary layer for a flat plate. We computed dispersion curves for a wide range of pressure gradients and inverse Froude numbers and, again, found some eigenmodes within the wall layer régime. Finally, we searched for long wave solutions for the asymptotic suction profile but found none.

In the second part, we studied the inviscid stability of a trailing vortex with mean flow profiles described by the similarity solution of Moore and Saffman. The axial and tangential velocity profiles obtained from this solution agree well with experiments involving wings at slight angles of attack; in particular, they are able to describe the jet-like and wake-like axial flows near the center of a trailing vortex. Two distinct computational routines were employed to solve the Howard-Gupta stability equation in order to retrieve the complex frequency and associated eigenmode: a Chebyshev spectral collocation method for unstable modes and a high accuracy shooting method with contour deformation for singular neutral (and near-neutral) modes. We looked at a wide range of values for the two physical parameters that control the nature of the mean flow, namely, the swirl flow parameter and the Moore-Saffman wing loading parameter n . For every such parameter pair, we searched for axial and azimuthal wavenumbers that support instability. The effect of a decrease in the wing loading parameter was determined to be destabilizing until $n = 0.44$, the point at which axial flow

changes from wake-like to jet-like. When comparing the Batchelor vortex (corresponding to $n \rightarrow 1$) to the case of the trailing vortex shed from an elliptically loaded wing ($n = 0.5$), for example, we found the latter to possess unstable modes with a significantly larger growth rate. Additionally, we established that unstable disturbances persist for a larger range of values of the swirl flow parameter. A rapid stabilization was observed for values of the wing loading parameter below $n = 0.44$.

The elliptical instability of a pair of counter-rotating Moore-Saffman vortices was considered in the last part of the thesis. In spite of the fact that the presence of an axial velocity component significantly affects elliptical instability characteristics, *e.g.* by modifying the dominant resonant pair, there have been few previous investigations that account for the diversity of axial flow that can be present in trailing vortices. This motivated us to employ the aforementioned family of mean flow profiles by Moore and Saffman since it is able to capture both deficits and excesses in the core axial velocity. A direct numerical simulation in cylindrical coordinates was performed to assess the stability of a vortex when subjected to a stationary dipolar strain field. We implemented a spectral method, proposed by Matsushima and Marcus, that uses algebraically mapped associated Legendre polynomials in the radial direction. These polynomials satisfy the pole condition exactly at the origin. We highlight two findings of our investigation. The first is that the growth rates of the elliptical modes of instability for the Moore-Saffman vortex are larger than those for the Batchelor vortex, by up to a factor of two. This is consistent with the conclusions of the linear inviscid stability analysis of Part 2 of this thesis. Next, our calculations yielded interesting results concerning the dominant resonant pair in the presence of an axial flow. Specifically, altering the axial flow strength or the Moore-Saffman wing loading parameter was found to cause a number of exchanges in the pair of azimuthal wavenumbers (m_1, m_2) that is most amplified. Although we identified many such exchanges between pairs of odd and even wavenumbers, closer inspection revealed these to correspond primarily to the resonances $(0, 2)$, $(-1, 1)$ and $(-2, 0)$. The dependency of the elliptical instability of the Moore-Saffman vortex on the Reynolds number and the strain rate offers interesting possibilities for future research.

REFERENCES

- [1] M. Abramowitz and I. A. Stegun. *Handbook of Mathematical Functions*. Dover Publications, New York, 1972.
- [2] E. A. Anderson and T. A. Lawton. Correlation between vortex strength and axial velocity in a trailing vortex. *J. Aircr.*, 40:699–704, 2003.
- [3] R. L. Ash and M. R. Khorrami. Vortex stability. In S. I. Green, editor, *Fluid Vortices*, pages 317–372. Kluwer, Dordrecht, 1995.
- [4] G. R. Baker, S. J. Barker, K. K. Bofah, and P. G. Saffman. Laser anemometer measurements of trailing vortices in water. *J. Fluid Mech.*, 65:325–336, 1974.
- [5] P. M. Balagondar, S. A. Maslowe, and S. Melkonian. The propagation of finite-amplitude waves in a model boundary layer. *Stud. Appl. Math.*, 76:169–185, 1987.
- [6] G. K. Batchelor. Axial flow in trailing line vortices. *J. Fluid Mech.*, 20:645–658, 1964.
- [7] G. K. Batchelor and A. E. Gill. Analysis of the stability of axisymmetric jets. *J. Fluid Mech.*, 14:529–551, 1962.
- [8] B. J. Bayly. Three-dimensional instability of elliptical flow. *Phys. Rev. Lett.*, 57:2160–2163, 1986.
- [9] T. B. Benjamin. The solitary wave on a stream with an arbitrary distribution of vorticity. *J. Fluid Mech.*, 12:97–116, 1962.
- [10] D. J. Benney. Long nonlinear waves in fluid flows. *J. Math. Phys.*, 45:52–63, 1966.
- [11] D. J. Benney and R. F. Bergeron Jr. A new class of nonlinear waves in parallel flows. *Stud. Appl. Math.*, 48:181–204, 1969.
- [12] P. Billant and F. Gallaire. Generalized Rayleigh criterion for non-axisymmetric centrifugal instabilities. *J. Fluid Mech.*, 542:365–379, 2005.
- [13] J. P. Boyd. *Chebyshev and Fourier Spectral Methods*. Dover Publications, New York, 2000.
- [14] R. L. Bristol, J. M. Ortega, P. S. Marcus, and Ö. Savaş. On cooperative instabilities of parallel vortex pairs. *J. Fluid Mech.*, 517:331–358, 2004.
- [15] A. P. Brown. Wake vortex core profiles and stability from enroute flight data. *AIAA Pap.*, pages 2011–3032, 2011.
- [16] J. C. Burns. Long waves in running water (with appendix by M. J. Lighthill). *Proc. Camb. Phil. Soc.*, 49:695–706, 1953.

- [17] B. Caiger and D. G. Gould. An analysis of flight measurements in the wake of a jet transport aircraft. In J. H. Olsen, A. Goldberg, and M. Rogers, editors, *Aircraft Wake Turbulence and its Detection*, pages 125–136. Plenum, New York, 1971.
- [18] A. B. Cain, J. H. Ferziger, and W. C. Reynolds. Discrete orthogonal function expansions for non-uniform grids using the fast Fourier transform. *J. Comput. Phys.*, 56:272–286, 1984.
- [19] J. S. Chow, G. G. Zilliac, and P. Bradshaw. Mean and turbulence measurements in the near field of a wing-tip vortex. *AIAA J.*, 35:1561–1567, 1997.
- [20] S. C. Crow. Stability theory for a pair of trailing vortices. *AIAA J.*, 8(12):2172–2179, 1970.
- [21] R. E. Davis. On the high Reynolds number flow over a wave boundary. *J. Fluid Mech.*, 36:337–346, 1969.
- [22] C. del Pino, L. Parras, M. Felli, and R. Fernandez-Feria. Structure of trailing vortices: comparison between particle image velocimetry measurements and theoretical models. *Phys. Fluids*, 23:013602, 2011.
- [23] W. J. Devenport, M. C. Rife, S. I. Liapis, and G. J. Follin. The structure and development of a wingtip vortex. *J. Fluid Mech.*, 312:67–106, 1996.
- [24] P. G. Drazin and W. H. Reid. *Hydrodynamic Stability*. Cambridge University Press, Cambridge, 1981.
- [25] P. W. Duck and M. R. Foster. The inviscid instability of a trailing line vortex. *Z. Angew. Math. Phys.*, 31:524–532, 1980.
- [26] C. Eloy. *Instabilité multipolaire de tourbillons*. PhD thesis, Université Aix-Marseille II, 2000.
- [27] C. Eloy and S. Le Dizès. Three-dimensional instability of Burgers and Lamb-Oseen vortices in a strain field. *J. Fluid Mech.*, 378:145–166, 1999.
- [28] C. Eloy and S. Le Dizès. Stability of the Rankine vortex in a multipolar strain field. *Phys. Fluids*, 13:660–676, 2001.
- [29] D. Fabre and L. Jacquin. Short-wave cooperative instabilities in representative aircraft vortices. *Phys. Fluids*, 16:1366–1378, 2004.
- [30] D. Fabre and L. Jacquin. Viscous instabilities in trailing vortices at large swirl numbers. *J. Fluid Mech.*, 500:239–262, 2004.
- [31] D. Fabre, D. Sipp, and L. Jacquin. Kelvin waves and the singular modes of the Lamb-Oseen vortex. *J. Fluid Mech.*, 551:235–274, 2006.

- [32] J. M. Faddy and D. I. Pullin. Flow structure in a model of aircraft trailing vortices. *Phys. Fluids*, 17:085106, 2005.
- [33] J. Feys and S. A. Maslowe. Long nonlinear surface waves in the presence of a variable current. *Stud. Appl. Math.*, 126:303–318, 2011.
- [34] J. Feys and S. A. Maslowe. Linear stability of the Moore-Saffman model for a trailing wingtip vortex. *Phys. Fluids*, 26:024108, 2014.
- [35] W. H. Finlay, C. Liu, and S. A. Maslowe. The nonlinear critical-wall layer in a parallel shear flow. *Stud. Appl. Math.*, 94:41–55, 1995.
- [36] Y. Fukumoto. The three-dimensional instability of a strained vortex tube revisited. *J. Fluid Mech.*, 493:287–318, 2003.
- [37] L. J. Garodz. Measurements of Boeing 747, Lockheed C5A and other aircraft wake characteristics by tower fly-by technique. In J. H. Olsen, A. Goldberg, and M. Rogers, editors, *Aircraft Wake Turbulence and its Detection*, pages 265–286. Plenum, New York, 1971.
- [38] D. Gottlieb and S. A. Orszag. *Numerical Analysis of Spectral Methods: Theory and Applications*. SIAM, Philadelphia, 1977.
- [39] S. I. Green. Wing tip vortices. In S. I. Green, editor, *Fluid Vortices*, pages 427–469. Kluwer, Dordrecht, 1995.
- [40] J. Hadamard. *Lectures on Cauchy’s Problem in Linear Partial Differential Equations*. Dover Publications, New York, 1952.
- [41] C. J. Heaton. Centre modes in inviscid swirling flows and their application to the stability of the Batchelor vortex. *J. Fluid Mech.*, 576:325–348, 2007.
- [42] C. J. Heaton. Optimal growth of the Batchelor vortex viscous modes. *J. Fluid Mech.*, 592:495–505, 2007.
- [43] L. N. Howard and A. S. Gupta. On the hydrodynamic and hydromagnetic stability of swirling flows. *J. Fluid Mech.*, 14:463–476, 1962.
- [44] J. Jiménez, H. K. Moffatt, and C. Vasco. The structure of the vortices in freely decaying two-dimensional turbulence. *J. Fluid Mech.*, 313:209–222, 1996.
- [45] R. S. Johnson. On the nonlinear critical layer below a nonlinear unsteady surface wave. *J. Fluid Mech.*, 167:327–351, 1986.
- [46] G. E. Karniadakis, M. Israeli, and S. A. Orszag. High-order splitting methods for the incompressible Navier-Stokes equations. *J. Comput. Phys.*, 97:414–443, 1991.
- [47] R. R. Kerswell. Elliptical instability. *Ann. Rev. Fluid Mech.*, 34:83–113, 2002.

- [48] M. R. Khorrami. On the viscous modes of instability of a trailing line vortex. *J. Fluid Mech.*, 225:197–212, 1991.
- [49] L. Lacaze, A.-L. Birbaud, and S. Le Dizès. Elliptical instability in a Rankine vortex with axial flow. *Phys. Fluids*, 17:017101, 2005.
- [50] L. Lacaze, K. Ryan, and S. Le Dizès. Elliptical instability in a strained Batchelor vortex. *J. Fluid Mech.*, 577:341–361, 2007.
- [51] M. J. Landman and P. G. Saffman. The three-dimensional instability of strained vortices in a viscous fluid. *Phys. Fluids*, 30:2339–2342, 1987.
- [52] F. Laporte and A. Corjon. Direct numerical simulations of the elliptical instability of a vortex pair. *Phys. Fluids*, 12(5):1016–1013, 2000.
- [53] F. Laporte and T. Leweke. Elliptical instability of counter-rotating vortices: experiment and direct numerical simulation. *AIAA J.*, 40(12):2483–2494, 2002.
- [54] S. Le Dizès. Viscous critical-layer analysis of vortex normal modes. *Stud. Appl. Math.*, 112:315–332, 2004.
- [55] S. Le Dizès and F. Laporte. Theoretical predictions for the elliptical instability in a two-vortex flow. *J. Fluid Mech.*, 471:169–201, 2002.
- [56] T. Lee and J. Pereira. Nature of wakelike and jetlike axial tip vortex flows. *J. Aircr.*, 47:1946–1954, 2010.
- [57] S. Leibovich and K. Stewartson. A sufficient condition for the instability of columnar vortices. *J. Fluid Mech.*, 126:335–356, 1983.
- [58] M. Lessen, P. J. Singh, and F. Paillet. The stability of a trailing line vortex. Part 1. Inviscid theory. *J. Fluid Mech.*, 63:753–763, 1974.
- [59] T. Leweke and C. H. K. Williamson. Cooperative elliptic instability of a vortex pair. *J. Fluid Mech.*, 360:85–119, 1998.
- [60] T. Loiseleux, J. M. Chomaz, and P. Huerre. The effect of swirl on jets and wakes: Linear instability of the Rankine vortex with axial flow. *Phys. Fluids*, 10(5):1120–1134, 1998.
- [61] X. Mao. *Vortex instability and transient growth*. PhD thesis, Imperial College London, 2010.
- [62] S. A. Maslowe. Instability of rigidly rotating flows to non-axisymmetric disturbances. *J. Fluid Mech.*, 64:302–317, 1974.
- [63] S. A. Maslowe. Critical layers in shear flows. *Ann. Rev. Fluid Mech.*, 18:405–432, 1986.

- [64] T. Matsushima and P. S. Marcus. A spectral method for unbounded domains. *J. Comput. Phys.*, 53:321–345, 1997.
- [65] T. Maxworthy, E. J. Hopfinger, and L. G. Redekopp. Wave motion on vortex cores. *J. Fluid Mech.*, 151:141–165, 1985.
- [66] E. W. Mayer and K. G. Powell. Viscous and inviscid instabilities of a trailing vortex. *J. Fluid Mech.*, 245:91–114, 1992.
- [67] D. W. Moore and P. G. Saffman. Axial flow in laminar trailing vortices. *Proc. R. Soc. London Ser. A*, 333:491–508, 1973.
- [68] D. W. Moore and P. G. Saffman. The instability of a straight vortex filament in a strain field. *Proc. R. Soc. London Ser. A*, 346:413–425, 1975.
- [69] L. C. Morland, P. G. Saffman, and H. C. Yuen. Waves generated by shear layer instabilities. *Proc. R. Soc. London Ser. A*, 433:441–450, 1991.
- [70] D. H. Peregrine. Interaction of water waves and currents. *Adv. Appl. Mech.*, 16:9–117, 1976.
- [71] W. R. C. Phillips. The turbulent trailing vortex during roll-up. *J. Fluid Mech.*, 105:451–467, 1981.
- [72] R. T. Pierrehumbert. Universal short-wave instability of two-dimensional eddies in an inviscid fluid. *Phys. Rev. Lett.*, 57:2157–2160, 1986.
- [73] D. I. Pullin and W. R. C. Phillips. On a generalization of Kaden’s problem. *J. Fluid Mech.*, 104:45–53, 1981.
- [74] L. G. Redekopp. On the theory of solitary Rossby waves. *J. Fluid Mech.*, 82:725–745, 1977.
- [75] C. Roy, T. Leweke, M. C. Thompson, and K. Hourigan. Experiments on the elliptic instability in vortex pairs with axial core flow. *J. Fluid Mech.*, 677:383–416, 2011.
- [76] C. Roy, N. Schaeffer, S. Le Dizès, and M. Thompson. Stability of a pair of co-rotating vortices with axial flow. *Phys. Fluids*, 20:094101, 2008.
- [77] P. G. Saffman. The structure and decay of trailing vortices. *Arch. Mech.*, 26:423–439, 1974.
- [78] P. G. Saffman. *Vortex Dynamics*. Cambridge University Press, Cambridge, 1992.
- [79] T. Sakai and L. G. Redekopp. An application of one-sided jacobi polynomials for spectral modeling of vector fields in polar coordinates. *J. Comput. Phys.*, 228:7069–7085, 2009.

- [80] D. Sipp and L. Jacquin. Widnall instabilities in vortex pairs. *Phys. Fluids*, 15(7):1861–1874, 2003.
- [81] P. R. Spalart. Airplane trailing vortices. *Ann. Rev. Fluid Mech.*, 30:107–138, 1998.
- [82] K. Stewartson. *The Theory of Laminar Boundary Layers in Compressible Fluids*. Oxford University Press, Oxford, 1964.
- [83] J. L. Synge. The stability of heterogeneous liquids. *Trans. Roy. Soc. Canada*, 27:1–18, 1933.
- [84] C.-Y. Tsai and S. E. Widnall. The stability of short waves on a straight vortex filament in a weak externally imposed strain field. *J. Fluid Mech.*, 73:721–733, 1976.
- [85] F. Waleffe. On the three-dimensional instability of strained vortices. *Phys. Fluids A*, 2:76–80, 1990.
- [86] S. E. Widnall. The structure and dynamics of vortex filaments. *Ann. Rev. Fluid Mech.*, 7:141–165, 1975.
- [87] S. E. Widnall, D. B. Bliss, and C.-Y. Tsai. The instability of short waves on a vortex ring. *J. Fluid Mech.*, 66:35–47, 1974.
- [88] C. S. Yih. Surface waves in flowing water. *J. Fluid Mech.*, 51:209–220, 1972.